Restitution des propriétés des aérosols et validation

Lyana Curier

Numéro d'ordre : 1848

UNIVERSITE BLAISE PASCAL

(U.F.R. de Recherche Scientifique et Technique)

ECOLE DOCTORALE DES SCIENCES FONDAMENTALES

N° 573

THESE

présentée pour obtenir le grade de

DOCTEUR D'UNIVERSITE

(Spécialité : Physique de l'atmosphère)

PAR

Lyana CURIER

Diplômé d'Etudes Approfondies

Restitution des propriétés des aérosols et validation

Soutenue publiquement le 2 Septembre 2008, devant la commission d'examen.

Président	Pr. P. Veefkind
Rapporteur	Pr. P. Builtjes
Rapporteur	Dr. A. Kokhanovsky
Examinateur	Pr. H. Kelder
Examinateur	Pr. G. de Leeuw
Directeur de thèse	Nadine Chaumerliac
Co-directeur de thèse	Maud Leriche

AEROSOL RETRIEVAL AND VALIDATION

Proefschrift

ter verkrijging van de graad van doctor

aan de Technische Universiteit Eindhoven

op gezag van de Rector Magnificus, prof.dr.ir. C.J. van Duijn,

voor een commissie aangewezen door het College voor Promoties

in het openbaar te verdedigen op dinsdag 2 september 2008 om 16.00 uur

door

Raymonde Lyana Curier

geboren te Basse-Terre, Frankrijk

Dit proefschrift is goedgekeurd door de promotoren:

prof.dr. H. Kelder

en

prof. N. Chaumerliac

Copromotoren:

prof.dr. G. de Leeuw

en

M. Leriche PhD

The work described in this thesis was performed at TNO Defence, Security and Safety, The Hague, The Netherlands.

The pictures appearing as footnotes, throughout the manuscript, are properties of "Piled Higher and Deeper" by Jorge Cham and were taken on the www.phdcomics.com website

Et venant je me dirais à moi-même:

" Et surtout mon corps aussi bien que mon âme,

gardez-vous de vous croiser les bras en l'attitude stérile du spectateur,

car la vie n'est pas un spectacle,

car une mer de douleurs n'est pas un proscenium,

car un homme qui crie n'est pas un ours qui danse..."

Cahier d'un retour au pays natal, Aimé Césaire

"You see, in this world there's two kinds of people, my friend those with loaded guns, and those who dig. You dig."

Sergio Leone, 1966

Remerciements

En matière de remerciements, il existe un ordre préétabli au cours duquel j'égrènerais mon inventaire de remerciements tel Prévert en partant du directeur de thèse, en passant par les collègues et enfin la famille.

Je resterai fidèle à moi-même et, sans grande surprises, je dérogerai à cette règle... Au cours de la rédaction de ce manuscrit j'ai dû m'armer de patience et me forcer à suivre un cheminement logique, ces remerciements, puisqu'ils m'appartiennent, n'en auront pas...

Mes remerciements les plus profonds et les plus sincères s'adressent à Gaby Curier. Son mode de vie et sa ténacité m'ont appris que tous les rêves sont accessibles. Sa générosité et son altruisme m'auront permis de réaliser mes rêves sans encombres ni soucis.

Sans aucun préambule ni aucune explication je dirai : " Merci Maman..."

Je profite de cette occasion pour exprimer ma gratitude et ma reconnaissance à tous mes proches qui m'ont encouragée pendant ces quatre ans de thèse mais aussi en bien d'autres occasions. Je remercie donc et sans ordre particulier : Yanis, Yanik, Yanaël, Yanaïs, Nana, Mam Mine.

The promotors, prof.dr. H. Kelder and prof. N. Chaumerliac, the copromotor M. Leriche PhD are gratefully acknowledged. Even though they did not

supervise my daily work, they were available and willing to help.

I would like to thank prof.dr. G. de Leeuw, my supervisor. He was a continuous support during theses years. I thank him for his reliability, direct feedbacks and also for introducing me to experts in the aerosol research field.

I am grateful to my entire committee for accepting to judge this last four years of work. I would like to acknowledge Peter Builtjes and Alexander Kokhanovsky my two "rapporteurs" for reviewing this manuscript and providing me with perspicacious feedbacks.

Un grand merci à Marianne D. qui était là, il y a maintenant quatre ans pour m'accueillir à la descente du train à Holland Spoor et m'initier aux joies de l'administration néerlandaise.

J'ai cherché une boutade, une contrepétrie, un bon mot pour te remercier de ton accueil, ton amitié au cours de ces quatre longues dernières années... Mais je n'ai rien trouvé qui reflète vraiment ce que je voulais dire... alors je dirai simplement, Merci Benoît...

Un clin d'oeil à mon acolyte de galère: Yas. Avec qui vais-je faire mes pauses de 10h...? Qui vais-je impressionner avec mes proverbes et mes citations et mon langage très imagé mais châtié...Allez Miss, la fin n'est pas loin ce n'est pas un mythe... Et puis Merci pour ces quatre dernières années.

Mon départ de La Haye s'associe à la fin de discussions les plus frivoles qui puissent exister, i.e. l'association fraise asperge ou encore l'utilité d'un siphon (de cuisine Yas!!!). Elles vont me manquer ces conversations Miss ou devrais-je dire Mme... Merci, Myriam.

Last but not the least...

Als laatste wil ik Menno bedanken. Jij was en bent mijn steun en toeverlaat geweest tijdens het schrijven van dit proefschrift. Jij hebt mij op veel meer

manieren geholpen dan jezelf beseft.

I am well-known for being absentminded, I would not be surprised, while reading the acknowledgement, I realize that I have forgotten one person or even more. Therefore, I would like to apologize... I am truly sorry, if your name should appear here and does not...

Abstract

Aerosols affect the radiation budget and cloud processes [IPCC, 2001, 2007] . It is hard to make an estimation of the impact due to the aerosols - because of a large variety of sources and precursors and a high variability on both time and space - but necessary for a better understanding and modeling of the Earth's global climate system.

Aerosol properties can be measured at ground level with good accuracy, however these data are often only representative for local situation and cannot be used on a regional to global scale. Therefore, one of the most efficient methods to study aerosol properties, at a large scale is, nowadays, to use satellite remote sensing data [IPCC, 2001, 2007]. Satellites allow for monitoring the highly variable aerosol fields at a reasonable spatial and temporal resolution. In this thesis two instruments and their associated aerosol retrieval algorithms are used. These algorithms allow for the retrieval of aerosol optical depth, i.e. the column integrated aerosol extinction coefficient along a vertical path through the atmosphere, over both ocean and land surfaces. A key parameter in aerosol retrieval is to distinguish between the atmospheric and surface contributions. The first algorithm was applied to the Advanced Along Track Scanning

Radiometer (AATSR) data to retrieve aerosol optical depth in the visible domain (see Veefkind and de Leeuw [1998] and Veefkind et al. [1998]). Results show the successful retrieval of information on the aerosol concentration. The second algorithm was designed to retrieve aerosol optical properties from the Ozone Monitoring Instrument (OMI) in the UV visible range (see Torres et al. [2002b]).

These algorithms have been further developed and tested over North Western Europe and the Amazon Basin. The case studies presented a collocation between high aerosol optical depth values and heavily industrialized areas, and downwind from the local sources large spatial gradients of the aerosol concentration. The results for both algorithms compare favorably with both ground based measurements and other spaceborne instruments.

Résumé

Les particules d'aérosols influencent le bilan radiatif terrestre en diffusant et absorbant le rayonnement solaire incident (*effet direct*), et en modifiant le cycle de vie ainsi que les propriétés radiatives des nuages (*effet indirect*). De par la grande hétérogénéité spatio-temporelle de leurs sources et de leurs précurseurs, l'estimation de cet impact reste un exercice difficile mais nécessaire afin de mieux appréhender le bilan radiatif du système Terre-atmosphère. Les propriétés optiques et physico-chimiques des aérosols sont suivies par des mesures au sol avec une grande précision. Cependant ces données sont représentatives de situations locales et restent très difficilement utilisables à grande ou moyenne échelle. Ainsi, au cours des trois dernières décennies plusieurs algorithmes, fondés sur l'inversion de données satellitaires, ont été développés permettant ainsi le suivi des particules d'aérosols à plus ou moins grande échelle pour des résolutions spatio-temporelles raisonnables. Dans cette thèse, deux instruments et leurs algorithmes associés sont utilisés. Ces algorithmes permettent la restitution des épaisseurs optiques des aérosols, correspondant à l'intégrale du coefficient d'extinction sur une tranche d'atmosphère, à la fois au-dessus des océans et des terres émergées. Au cours de chacune des études présentées ici les résultats inversés sont validés par comparaison avec d'autres jeux de données

issues de mesures au sol et avec d'autres algorithmes d'inversion. L'algorithme *TNO DV-AATSR* a été utilisé en premier et résulte du couplage de deux algorithmes le *Single View algorithme* [Veefkind and de Leeuw, 1998], et le *Dual View algorithme* [Veefkind et al., 1998]. Il s'applique aux radiances mesurées par le radiomètre AATSR (Advanced Along Track Scanning Radiometer), dans le visible et le proche infrarouge. Le second, l'algorithme *" multi-wavelength "*, a été développé afin d'inverser les propriétés optiques des particules d'aérosols, telles que les épaisseurs optiques et les albédos de diffusion simple à partir des radiances mesurées par le spectromètre OMI (Ozone Monitoring Instrument) dans le proche UV et le visible (cf.Torres et al. [2002b]).

La distinction entre la contribution de la surface et la contribution atmosphérique au signal mesuré est primordiale. La restitution des propriétés optiques des particules d'aérosols à partir de radiances mesurées au sommet de l'atmosphère est un problème inverse mal posé. Ainsi, plusieurs informations à priori sur l'albédo de la surface, la granulométrie et la composition chimiques des particules d'aérosols sont nécessaires afin de contraindre le problème.

C'est dans cette optique que les deux algorithmes ont été développés et testés sur le Nord-Ouest de l'Europe et sur le bassin amazonien. Les cas étudiés se situaient dans des zones, fortement industrialisées et comportant des couches d'aérosols de forte épaisseur optique sous le vent de sources locales avec de forts gradients de concentration en aérosols. Les résultats obtenus avec ces algorithmes permettent une bonne restitution des concentrations en aérosols.

Contents

List of Tables

List of Figures

Chapter 1

Background and Theory

Over the last decades, various climatics events (heat waves, hurricanes) were observed. Their increasing frequency makes us wonder on climate change and effects due to human activities. Almost every week, media draws our attention on *global warming*, *reduction of the ice pack*. Therefore, the study of climate change is a hot topic. Nowadays, the effects of aerosol[1] remain one of the largest uncertainties in our understanding of climate. These uncertainties are inherent to the complex relation between aerosol properties and the multiphase system which is the atmosphere. Aerosols directly affect climate by increasing the scattering and/or absorption of solar radiation and indireclty by changing cloud microphysics and thus cloud albedo and precipitation cycle. Moreover, heterogeneous chemical processes occur at their surfaces.

Over the last three decades monitoring of aerosol particles from space has become feasible. A general consensus has been reached that satellite remote sensing provides viable means for measurement-based characterisation of aerosol optical properties on regional to global scale. The improvement in aerosol satellite remote sensing has contributed to the increase of the level of scientific understanding since the third assessment report of the IPCC in 2001 [IPCC, 2001,

[1] a definition of aerosol particles is given Section 1.2

2007]. The problem with aerosol particles is their short lifetime (e.g. days), complex chemical composition and interactions in the atmosphere which in turn result in large spatial and temporal hetereogeneities.

The work described in this thesis contributes to a better understanding of the effect of aerosol particles on climate and air quality. Measurements from satellite based instruments are used to retrieve the optical properties of aerosol particles. More precisely, we use the radiance measured at the top of the atmosphere (TOA) by either AATSR[2] or OMI[2] to obtain this information, and the results are compared with other measurement-based data.

A large part of this work is presented as articles which have been puslished or submitted for publication. As a consequence there is some redundancy concerning the state of the art on aerosol remote sensing and/or algorithm descriptions in the various chapters.

In this chapter, some background is given on the climate system, what are aerosols, how do they affect the climate system and what is the theory behind aerosol remote sensing?

1.1 The climate system

The Earth's surface intercepts, everyday at day time, about 1367 W $\cdot$ m $^{-2}$ of the incoming solar radiation which represents 342 W $\cdot$ m $^{-2}$ over the entire planet. Clouds, molecules, aerosol particles and the surface reflect about 30% of this incoming radiation back to space. The remaining 70% are absorbed by the atmosphere and the Earth's surface. The absorbed radiation heats the earth system which in turn emits this heat as radiation in the thermal infrared following

[2]this intrument is presented Section 1.6

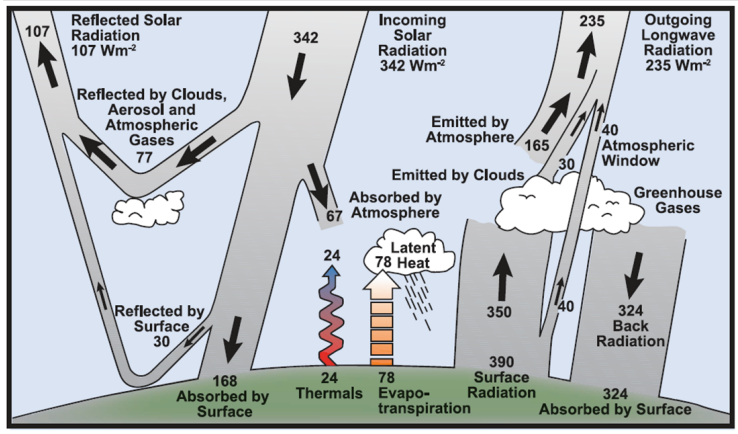

Figure 1.1: Estimate of the Earth's annual and global mean energy balance. Source: IPCC [2007].

the Stefan-Boltzmann law[3]. A large amount of the emitted radiation is absorbed by the atmosphere and is radiated back to the Earth surface. This phenomenon is called the *greenhouse effect* and is mainly due to the presence of trace gases such as water vapor, carbon dioxide, methane and ozone in the atmosphere. The *greenhouse effect* warms the Earth's surface of the planet and maintains the average temperature around 14°C instead of the -19°C prescribed by the Stefan-Boltzmann law. The long term energy balance of the Earth-atmosphere system is described schematically in Figure 1.1. The amount of incoming solar radiation absorbed by the Earth-atmosphere system is balanced by the release of the same amount of longwave radiation by the Earth-atmosphere system.

The climate system is an open system where the atmosphere, the surfaces and the biosphere interact and the incoming solar radiation supplies energy.

[3] $j^* = \sigma \cdot t^4$

The climate system evolves in time under the influence of its own internal dynamics. Changes in the climate system are also due to externals forces such as variation in the incoming solar radiation, the cloud cover, the atmospheric particles, the vegetation or the greenhouse gas concentrations. Changes in the climate system due to external influences in the Earth's radiative balance are defined as 'radiative forcing'.

The changes in the incoming solar radiation are purely natural, whereas recently the changes in the other external influences are considerably disturbed by human activities. Since the beginning of the industrial era, significant increases in the emissions of carbon dioxide, methane, nitrous oxide and halocarbons, also kown as the long lived greenhouse gases, have been observed. Forster et al. [2007] attribute all of these increases to human activities. The long lived greenhouse gases are relatively well mixed in the atmosphere and therefore few observations are sufficient to determine their global warming potential. Ozone, which is formed by photochemical processes, also contributes significantly to the change in radiative forcing. Forster et al. [2007] estimate the anthropogenic contribution to the radiative forcing, due to the combined actions of long lived greenhouse gases and ozone, to be 2.9 ± 0.3 W $\cdot$ m $^{-2}$.

Aerosols partly balance the warming effect of the long-lived greenhouse gases. They absorb and/or reflect the incoming solar flux and on the other hand they influence the radiative properties and the time life of clouds. The combined anthropogenic aerosol direct effect and cloud albedo effect[4] is assumed to exert a radiative forcing of 1.3 ± 0.3 W $\cdot$ m $^{-2}$ with a 90% confidence range between -2.2 and -0.5 W $\cdot$ m $^{-2}$. Seinfeld and Pandis [1998] assess that, nowadays, 10% of the atmospheric aerosol particles are due to human activities.

[4] detailled explanation on aerosol direct effect and the cloud albedo effect is given Section 1.4

The Fourth assessment report of the IPCC [IPCC, 2007] estimates that the combined effect of human activities on climate, is $+1.6\ \mathrm{W} \cdot \mathrm{m}^{-2}$ with a 90% confidence range between -0.6 and $2.4\ \mathrm{W} \cdot \mathrm{m}^{-2}$.

1.2 Atmospheric aerosol particles

In the following paragraphs a brief introduction to atmospheric aerosol particles is given, which is largely inspired by the one presented by Seinfeld and Pandis [1998].

An aerosol is technically defined as a suspension of fine solid and/or liquid particles in a gas [Seinfeld and Pandis, 1998]. The origin of aerosol particles is very divers. They are either directly emitted, *primary aerosols*, to the atmosphere or formed via various physico-chemical processes,*secondary aerosols*, in the atmosphere. The main sources are natural (sea spray, biogenic, etc.) but, since the Industrial Revolution, a sizeable contribution (10%) is due to human activities. The aerosol number/mass concentrations and chemical composition highly depends on their sources. The geographical distribution of aerosol particle sources is non-uniform and therefore a large variation in aerosol particle concentration and chemical properties is observed across the planet. Table 1.1 gives an overview of the source strengths and atmospheric burden of the most dominant types of atmospheric aerosols.

Aerosol particle sizes range from a few nanometers to several hundreds of micrometers. Particles with a diameter smaller than 2.5 μm are often referred to as *fine particles* and the larger ones as *coarse particles*. The coarse particles are mainly emitted via mechanical processes and are strongly subject to sedimentation. Within the fine particle class, a distinction between *Aitken* mode

and *accumulation* mode is often made. Typically, the *Aitken* diameters range from 5 to 100 nm, they are predominantly formed via gas-to-particle conversion and determine the number concentration of the fine particle class. Due to their important Brownian motion they have a short lifetime. Coagulation due to collisions with other particles induces their transfer to the *accumulation* mode. The diameter of the particles of the *accumulation* mode is between 100 nm and 2500nm. The *accumulation* mode is so named because particle removal mechanisms are least efficient in this regime, causing particles to accumulate there.

Aerosol particle removal processes occur by means of two mechanisms, Dry deposition occurs when the particles are directly transported to the Earth's surface. On the other hand, wet deposition encompasses all processes by which aerosol particles are transferred to the Earth's surface in aqueous form: (i) removal when they serve as cloud condensation nuclei, (ii) removal when they collide with a droplet within or below clouds. As the aerosol particles are subject to wet and dry deposition, their residence times in the atmosphere vary from a few days to a few weeks. Figure 1.2 is a schematic description of the aerosol sources and sinks.

Aerosols can be classified in several ways. Earlier we made a size distinction, a production classification, the third assessment report of the IPCC [IPCC, 2001] classified five major aerosol types according to their chemical composition: soil dusts, sea salt, carbonaceous, sulfate and nitrate. The study presented in this thesis focuses on aerosol optical properties. It is therefore appropriate to classifiy the aerosol in accordance with their ability to scatter and/or absorb solar radiation. We define three generic types: nonabsorbing, mineral dust and carbonaceous which are briefly described in Section 1.2.1 to 1.2.3.

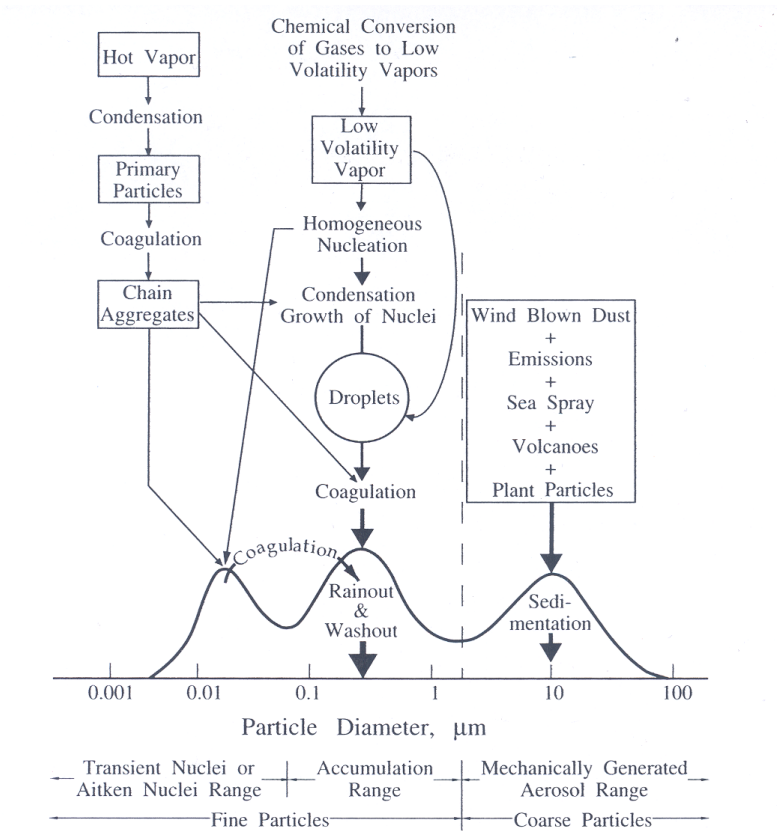

Figure 1.2: Idealized schematic of the distribution of the particle surface area of an atmospheric aerosol *(Whitby and Cantrell 1976)*. Principal modes, sources, and particle formation and removal mechanism are indicated. Source: Seinfeld and Pandis [1998]

Table 1.1: Source strength and atmospheric burden for various types of aerosols. Adapted from Andreae and Crutzen [1997]; Seinfeld and Pandis [1998]

Natural 90%			
particles	source	flux ($Tg.yr^{-1}$)	range
primary	soil dust	1500	1000-3000
	sea salt	1300	1000-10000
	volcanic ashes	33	4-10000
	biological debris	50	26-80
secondary	Sulfates	102	85-210
	organic matter	55	40-200
	Nitrates	22	15-50
Antropogenic 10%			
particles	source	flux ($Tg.yr^{-1}$)	range
primary	Industrial dust	100	40-130
	Soot	20	5-20
secondary	Sulfates from SO_2	140	120-250
	Biomass burning	80	50-150
	Nitrates	36	25-65
	Organics matter	10	5-25

1.2.1 Nonabsorbing aerosols (sea spray, sulfate, nitrate)

Sea spray, sulfate and nitrate aerosol do not absorb light in the visible wavelengths. Sea spray is entirely from natural origin and is generated by breaking waves. They constitute a major aerosol component (see Table 1.1) and their concentration strongly depends on the local wind speed. Sea spray particles contribute mainly to the coarse mode, although recent findings indicate significant emission of submicron sea spray down to ca. 10 nm. [Clarke et al., 2006; O'Dowd and de Leeuw, 2007].

Sulfate and nitrate are mainly formed via gas-to-particle conversion and are from natural (DMS, volcanoes) and anthropogenic (fossil fuels) origins. They contribute predominantly to the accumulation mode [Seinfeld and Pandis, 1998]. In the atmosphere, the sulfate, SO_4^{2-}, is mainly found in the form of ammonium sulfate, $(NH_4)_2SO_4$. Sulfate is formed via the oxidation of sulfur dioxide, SO_2 either in gas or liquid phase, which reacts with ammonia, NH_3. The nitrate aerosol particles are formed by oxidation of nitrogen dioxide, NO_2. The concentration of nitrate aerosol particles is closely connected to the concentration of sulfur dioxide and ammonia. In fact, the formation of ammonium sulfate is dominant, once the sulfure dioxide is neutralized, excess ammonia reacts with nitrogen dioxide.

Nonabsorbing aerosols are highly hygroscopic and therefore easily act as cloud condensation nuclei.

1.2.2 Mineral dust aerosol

Mineral dust particles are mechanically generated over the deserts and other arid regions. They are mainly produced by wind erosion and the sources are mainly

located at low latitudes such as the Sahara desert, the Middle East, the Gobi desert (collectivly known as the the global dust belt) [Prospero et al., 2002]. In the Southern hemisphere, arid regions in Australia, South Africa, South America also contribute to the total mineral dust load. A small proporportion of these aerosol particles, about 5 to 7%, originates from agricultural and industrial activities [Tegen et al., 2004], i.e. has an anthropogenic origin.

Mineral dust particles are typically nonspherical and their chemical composition is highly variable. In fact, the chemical composition which determines the complex refractive index, and thus the optical properties, depends on the composition of bed surfaces, spatial and temporal variability of the production mechanisms [Sokolik and Toon, 1999]. The presence of iron oxides (e.g. hematites) in mineral dust is responsible for the absorption of UV- radiation.

1.2.3 Carbonaceous aerosols

Black carbon and organic carbon aerosol particles significantly contribute to the total aerosol mass [Novakov et al., 1997; Heintzenberg, 1989]. Black carbon is a primary aerosol emitted directly at the source from incomplete combustion processes such as fossil fuel and biomass burning [IPCC, 2007]. Black carbon aerosol strongly absorbs solar radiation. Organic carbon can be of both primary and secondary origin. Natural sources for primary organic carbon are mainly pollen, bacteria, plant debris, spores and algae [Bauer et al., 2002]. The production of secondary organic carbon is driven by the oxidation or the condensation of volatil organic compounds. The hygroscopic, chemical and optical properties of organic carbon are continuously changing because of chemical processing by gas-phase oxidants such as ozone, OH and NO_x.

An overview on organic carbon aerosol can be found in Kanakidou [2005]

1.3 Aerosol Extinction: definitions

A particle in the path of an electromagnetic wave continuously extracts energy from it. This energy can be elastically scattered, i.e. radiates this energy in all directions without energy loss, and/or absorbed, i.e. converted into heat by the particle. In our everyday life we experience and rave about such phenomena, e.g. sunsets, rainbows, glories, halos etc., which result from refraction and reflection of the incomming solar radiation by particles or cloud droplets or even ice crystals.

The attenuation of the incoming solar radiation as it travels through the atmosphere is described by the well-known Beer-Lambert-Bouguer law.

$$\frac{I(L)}{I_0} = \int_0^L e^{\sigma_e h} dh \tag{1.1}$$

where I_0 is the intensity of the incident light, I is the intensity after passing through the atmosphere along a path with length L, σ_e is the extinction coefficient.

The atmospheric extinction is due to absorption and scattering by both gases and aerosol particles. As these processes are additive the extinction coefficient can be broken down as:

$$\sigma_e(\lambda, h) = \sigma_{a,p}(\lambda, h) + \sigma_{s,p}(\lambda, h) + \sigma_{a,r}(\lambda, h) + \sigma_{s,r}(\lambda, h) \tag{1.2}$$

where subscripts a, s, p and r denote absorption, scattering, aerosol particles and gas molecules, respectively.

Although for simplicity the particles are often assumed to be spherical it is pointed out that the shape of a particle also influences the probability of light

reflection in a given direction. Two reasons explain why the spherical assumption is realistic. First, secondary aerosol, such as sulfate and nitrate, are mainly formed via gas-to-particle conversion either on existing particles or forming new particles, which leads to spherical particles. Second, the hygroscopicity of the particles implies that they are usually almost spherical particles. In fact, as the ambient relative humidity increases, the particles remain solid until the relative humidity reaches a threshold value, the delisquescence point, which is characteristic for particle composition, and they sponteanously absorb water. On the other hand, evaporation of water is observed as the relative humidity decreases. The aerosol particles will however remain in their activated state (i.e. aqueous solution) as the relative humidity below which crystallisation occurs is much lower than the delisquescence point.

The spherical assumption is difficult to justify when observing aerosol particles such soil dust, as these particles are non-hygroscopic and mechanically generated. Therefore, it is important to account for the nonspherical features of these aerosol particles when using optical instruments. For more information on the effect of the non-sphericity of aerosol optical properties the reader is referred to Mishchenko et al. [1995]; Li-Jones et al. [1998]; Volten et al. [2001]

In the present study, no case involving soil dust particles is considered, therefore aerosol paticles are assumed spherical and the aerosol extinction is calculated using Mie theory [Mie, 1908].

$$\sigma_{ep}(\lambda, h) = \int_0^R Q_e\left(\frac{2\pi r}{\lambda}, m\right) \cdot \pi r^2 . n(r) dr \tag{1.3}$$

where Q_e is the mass extinction effeciency of aerosol particles with the size parameter $\frac{2\pi r}{\lambda}$ and complex refractive index m, such as $m = n - ik$ where

n and k describe respectively the scattering and absorbing properties of the aerosols. r represents the radius of the aerosol particles and R the maximum radius considered, $n(r)$ is the number size distribution. Equation 1.3 shows that the light scattering of the solar radiation depends on several factors such as particle size, chemical composition (i.e. , refractive index) and density.

The *aerosol optical depth* is defined as the aerosol extinction coefficient integrated over a vertical path from the ground to the TOA, and is dimensionless.

$$\tau(\lambda) = \int_0^{TOA} \left(\sigma_{a,p}(\lambda, h) + \sigma_{s,p}(\lambda, h)\right) dh \tag{1.4}$$

The spectral behavior of the aerosol optical depth can be represented by a power law function

$$\tau(\lambda) = \beta\lambda^{-\alpha} \tag{1.5}$$

The ratio of scattering (σ_{sc}) to extinction is called the *single scattering albedo*, $\omega_0(\lambda, m)$. The fraction, 1-$\omega_0(\lambda, m)$, is a measure for the amount of absorption relative to the total extinction. The value of the single scattering albedo is 1 when the extinction is solely due to scattering.

$$\omega_0(\lambda, m) = \frac{\sigma_{sc}(\lambda, m)}{\sigma_{ex}(\lambda, m)} \tag{1.6}$$

The aerosol single scattering albedo is a key parameter when determining the influence of aerosols on climate. If $\omega_0(\lambda, m) > 0.95$, for example, the aerosol particles induce cooling under almost all conditions. If $\omega_0(\lambda, m) < 0.9$, the aerosol particles locally heat the troposphere significantly.

The angular distribution of the scattered light is described by the *phase function* $p_{11}(\Omega)$, i.e. , the amount of incident light $(\theta_0\phi_0)$ scattered into the direction $\theta\phi$. The phase function is a probability distribution and is normalized according to Equation 1.7.

$$\int_{4\pi} p_{11}(\Omega)\, d\Omega = 4\pi \tag{1.7}$$

where $d\Omega = sin\theta d\theta d\phi$ is a solid angle around the scattering direction (θ, ϕ). Assuming that the particles are either spherical or randomly orientated the phase function can be simplified as follows:

$$\int_0^{2\pi} \int_0^{\pi} p_{11}(\theta, \phi)\, sin\theta d\theta d\phi = \int_0^{\pi} p_{11}(\theta)\, sin\theta d\theta = 2 \tag{1.8}$$

The aerosol phase function is anisotropic, thus a parameter called the *average cosine of the phase function* or *asymmetry parameter* is used to describe the degree of anisotropy of the phase function.

$$g = \frac{1}{2} \int_0^{\pi} p_{11}(\theta)\, cos\theta sin\theta d\theta \tag{1.9}$$

1.4 Aerosol radiative forcing

The aerosol effect on the Earth radiative budget is twofold, they absorb and/or reflect the incoming solar flux and on the other hand they influence the radiative properties and the lifetime of clouds. The aerosol radiative effect depends on the aerosol shape, size distribution and chemical composition. The ability of aerosol particles to activate and become cloud condensation nuclei and/or ice nuclei is a key factor for assessement of the aerosol indirect effect. The aerosol

activation to form cloud droplets via heterogenous nucleation is nowadays well understood, cf. Pruppacher and Klett [1997]; Seinfeld and Pandis [1998].

The quantification of the aerosol effect on a global scale is quite difficult and large uncertainty remains. Excellent overviews have been presented by Haywood and Boucher [2000] and Lohmann and Feichter [2005.]. The Fourth assessment report of the IPCC [IPCC, 2007] estimates that the combined aerosol direct and cloud albedo effects exert a radiative forcing that is certain to be negative, with a median of $-1.3 \pm W \cdot m^{-2}$ with a 90% interval confidence between -2.2 and -0.5 W$\cdot$ m^{-2}

1.4.1 Aerosol direct radiative effect

The aerosol direct radiative effect is the most easily understood interaction between aerosols and climate, i.e. scattering and/or absorption of the short- and longwave radiation. The current best measurement-based estimates of the clear-sky direct radiative effect at TOA are about -5.5 $\pm 0.2 W \cdot m^{-2}$ over the global ocean [Yu et al., 2006]. Over land the integration of satellite retrievals and model simulations results in an estimate of -4.9$\pm$0.7$W \cdot m^{-2}$ [Yu et al., 2006]. Table 1.2 summarizes estimates of the antropogenic aerosol direct radiative forcing. Kaufman et al. [2005], Bellouin et al. [2005] and Yu et al. [2006] provide measurement-based assessements of the aerosol direct radiative forcing whereas Schulz et al. [2006] and Forster et al. [2007] use models for this purpose. The measurement-based estimate provided by Bellouin et al. [2005] for the global all-sky condition is stronger by a factor 2 to 4 than the model-based estimate.

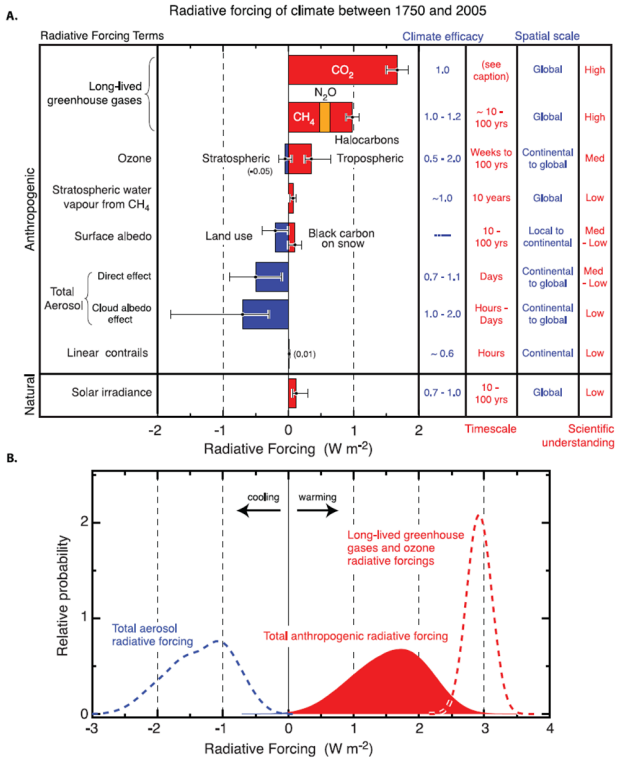

Figure 1.3: A./Global mean radiative forcing ($W \cdot m^{-2}$) due to increase in the emissions from pre-industrial (1750) to 2005. Anthropogenic and natural direct solar radiative forcing are shown. Time scales represent the length of time that a given RF term would persist in the atmosphere after the associated emissions and changes ceased. No CO_2 time scale is given, as its removal from the atmosphere involves a range of processes that can span long time scales, and thus cannot be expressed accurately with a narrow range of lifetime values. B./ Probability distribution functions. Three cases are shown: the total of all anthropogenic radiative forcing terms, long-lived greenhouse gases (CO_2, CH_4, N_2O, SF_6) and ozone radiative forcings only, finally the aerosol direct and cloud albedo radiative forcings only. Obtained from the IPPC report [IPCC, 2007]

Table 1.2: Anthropogenic aerosol direct radiative forcing $W \cdot m^{-2}$

Reference	clear sky ocean	clear sky global	all-sky global
Kaufman et al. [2005]	-1.4 ± 0.4	-	
Bellouin et al. [2005]		-1.9 ± 0.3	-0.8 ± 0.1
Yu et al. [2006]	-	-1.3 ±	-
Schulz et al. [2006]	-	-0.7 ± 0.2	-0.2 ± 0.2
Forster et al. [2007]	-	-0.7 ± 0.3	-0.4 ± 0.4

1.4.2 Aerosols and Clouds

Clouds are important regulators of the Earth's radiation budget. About 60% of the Earth's surface is covered with clouds. Aerosol particles and clouds are closely related because aerosol particles act as cloud condensation nuclei. If the Earth's atmosphere were totally devoid of aerosol paticles, the Kelvin equation[5] prescribes that there would be no cloud formation as homogeneous nucleation is unlikely to happen. Aerosol activation is the process in which the aerosol particles grow to form cloud droplets. The number concentration of the activated aerosols does not affect the cloud liquid water content, however, it drives the cloud droplet number concentration. When there are more cloud condensation nuclei, the available amount of water is distributed over more cloud droplets, which therefore have a smaller radius i.e. the aerosol particles affect the cloud microphysics. This effect on the cloud microphysic is known as Towmey effect [Twomey, 1977] or cloud albedo effect as suggested by the Fourth assessment report of the IPCC [IPCC, 2007]. Note that the relationship between aerosol number concentration and the cloud droplet number concentration is nonlinear

[5] $p_w = p_w^0 exp\left(\frac{2\sigma_w M_w}{RT\rho_w R_d}\right)$

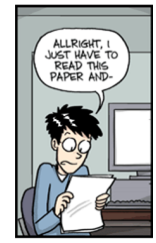

[Feingold, 2003]. Based on the result of modelling, Forster et al. [2007] present the best estimate for the cloud albedo effect of -0.7 $W \cdot m^{-2}$ with the 5 to 95% confidence range of -0.3 to -1.8 $W \cdot m^{-2}$

It is also assumed that the aerosols increase the lifetime of clouds. When droplets are smaller both their gravitational deposition decreases and they evaporate faster and therefore the precipitation rate is reduced. This effect is known as the Albrecht effect [Albrecht, 1989], although in the Fourth assessment report of the IPCC [IPCC, 2007] the term cloud lifetime effect is used.

The cloud albedo and lifetime effect induce a heat loss for the climate system by increasing cloud optical depth and cloud cover, respectively, thus reducing the net solar radiation at TOA.

1.5 Aerosol Remote sensing

In this section a brief description of aerosol remote sensing is given. Section 1.5.1 presents the aerosol passive remote sensing from space. First applications of satellite remote sensing of aerosols were made to detect desert dust aerosol over the ocean, in the mid-1970s using Landsat, GOES and AVHRR data [Fraser, 1976; Griggs, 1975]. Satellite remote sensing of aerosols initially focussed over ocean because surface reflectivity is low. First attempts to characterize aerosols over land surface were made in the beginning of the 1980s, to improve land surface images by introducing an atmospheric correction

1.5.1 Passive remote sensing from space

Passive remote sensing is based on the fact that the incoming solar radiation is alterated by the atmosphere and the surface. The emerging radiation at TOA in

the satellite direction is influenced by a myriad of processes in the atmosphere and at the surface: single scattering of the direct solar beam, multiple scattering from all directions, emission from the atmosphere, attenuation of the incoming reflected radiation by extinction, reflection by the surface. How is the aerosol contribution separated from all these processes affecting the received radiation? As seen earlier (Section 1.4.2), clouds influence aerosol properties and therefore the aerosol contribution to the TOA radiance is derived only in cloud free situations. In such conditions, the TOA reflectance assuming a Lambertian surface can be derived from the measured TOA radiance by:

$$\rho = \frac{\pi \cdot L}{F_0 \cdot cos\theta_0} \tag{1.10}$$

where L is the measured radiance, F_0 is the extraterrestrial solar irradiance and θ_0 is the solar zenith angle.

The spectral behavior of the surface reflectivity is a determing factor in the approach used to retrieve the aerosol properties from their contribution to the TOA reflectance. Assuming a horizontally uniform atmosphere overlying a Lambertian surface, the TOA reflectance, for a given sun-satellite geometry, can be written as [Chandrasekhar, 1960]:

$$\rho(\lambda, \theta, \theta_0, \phi) = \rho_{atm}(\lambda, \theta, \theta_0, \phi) + \frac{\rho_{sfc}(\lambda, \theta, \theta_0, \phi)}{1 - \rho_{sfc}(\lambda, \theta, \theta_0, \phi) \cdot s(\lambda)} T(\lambda, \theta, \theta_0) \tag{1.11}$$

In the near UV domain, the albedo of most surfaces is low (2% to 5%) [Herman and Celarier, 1997]. In such case, the atmospheric contribution and the surface contribution are usually separated by using a precalculated surface reflectance database obtained from application of the minimum reflectivity technique.

In the visible and near infra-red domain, a major dichotomy according to surface types is observed when accounting for the surface contribution. Over dark surfaces, i.e. ocean surfaces, the most common approach is to represent the surface by a Lambertian approximation which is tuned, by means of a Cox and Munk parametrization, to account for wave influences, as follows:

$$\rho = T_{\downarrow}\rho_{s,dir}T_{\uparrow} + t_{\downarrow}\rho_{s,dif_{\downarrow}}T_{\uparrow} + T_{\downarrow}\rho_{s,dif_{\uparrow}}t_{\uparrow} + t_{\downarrow}\rho_{s,dif_{\uparrow\downarrow}}t_{\uparrow} + \rho_{atm} \tag{1.12}$$

Where ρ_{atm} is the path reflectance by aerosols and molecules, T is the direct transmittance along an upward ($\uparrow$) and downward ($\downarrow$) path, and t is the diffuse transmittance due to forward scattering by aerosol particles and molecules. $\rho_{s,dir}$, $\rho_{s,dif_{\downarrow}}$, $\rho_{s,dif_{\uparrow}}$, $\rho_{s,dif_{\uparrow\downarrow}}$, describe the surface bidirectional reflection. The aerosol scattering processes depend on the sun-satellite geometry. The aerosol contribution also depends on the aerosol optical properties, and the aerosol vertical distribution. The molecular processes which attenuate and scatter the outcoming solar radiation toward the space borne instrument are generally simulated using radiative transfer calculations.

Over bright surfaces, the photons reflected by the surface contribute significantly to the TOA reflectance. The TOA reflectance measured by the space-borne instrument is commonly approximated using Equation 1.11. The impact of the aerosols is first to increase the path reflectance, ρ_{atm} and second to reduce the transmittance. When the surface reflectance is small, the first aerosol impact will dominate. For larger values of the surface reflectance the transmittance reduction will become more and more important. Nowadays, several methods are used to account for the surface contribution:

1. using a surface reflectance database

2. introducing a relationship between the surface reflectance in the visible and mid-IR [Kaufman et al., 1997; Levy et al., 2007b].

3. parametrizing the surface reflectance [Grey et al., 2006]

4. assuming that the wavelength dependence of the shape of the surface BRDF is negligible [Veefkind et al., 1998]

Once the surface and the molecular contributions are accounted for, a merit function, ϵ^2, is minimized to retrieve the aerosol model which best represents the measured reflectance.

$$\epsilon_j^2(\lambda_l) = \sum_l \left[\rho_{meas}(\lambda_l) - \rho_{calc,j}(\tau_j(\lambda_{ref}), \lambda_l)\right]^2 \tag{1.13}$$

$\rho_{calc,j}(\tau_j(\lambda_{ref}), \lambda_l)$ is the TOA reflectance computed by means of radiative transfer calculations and stored into look up tables, to simulate the effects of a variety of aerosol models for different aerosol optical depths and sun-satellite geometries which encompass the global aerosol range.

The aerosol model for which the merit function is minimum is chosen as the most appropriate aerosol model. The determination of the most appropriate aerosol model allow for retrieving the aerosol optical depth by using either a non-linear fitting method such as the Levenberg-Marquardt or the linearity assumption Durkee et al. [1986]; Veefkind [1999].

1.5.2 Ground-base remote sensing

The AErosol RObotic Network (AERONET, Holben et al. [1998]) is a network of sunphotometers, established by NASA, continuously measuring atmospheric

aerosol properties. It provides observations of the aerosol optical depth at several wavelengths and inversion products for diverse regions. The measurements of aerosol optical depth data are available for three data quality levels: Level 1.0 (unscreened), Level 1.5 (cloud-screened, Smirnov et al. [2000]), and Level 2.0 (cloud screened and quality-assured). Level 1.0 and level 1.5 are near real-time data whereas quality assured Level 2.0 data are available only after a periodic calibration which is yearly carried out. Direct sun measurements are made at several wavelengths (e.g. 340, 380, 440, 500, 670, 870 and 1020 nm) depending on the type of instrument (all instruments used by the AERONET are CIMEL, but several models are available). The aerosol optical depth is calculated from spectral extinction of direct beam radiation at each wavelength based on the Beer-Lambert-Bouguer law after the attenuation due to Rayleigh scattering has been corrected for. In addition to direct sun measurements the sunphotometers also make an almucantar scan, i.e. , observation of the angular distribution of the sky radiance through a scan at low elevation angles. From theses measurements, the aerosol size distribution as well as the single scattering albedo and the phase function are extracted [Dubovik et al., 2002].

1.6 Instruments Overview

Aerosol retieval studies were intially made using the Advanced Very High Resolution Radiometer (AVHRR) and Total Ozone Mapping Spectrometer (TOMS) data. For these instruments long time series are available of more than 25 years. The primary goal of AVHHR and TOMS was to monitor respectively the meteorological conditions and the ozone layer and they were not designed to monitor aerosol optical properties. However, the AVHHR instrument provided top of the

atmosphere radiances in the visible and the near infrared which were used to retrieve aerosol optical properties over ocean [Husar et al., 1997; Durkee et al., 1991] and TOMS has proved to be succesful in monitoring UV absorbing aerosol particles such as mineral dust and carbonaceous aerosols [Torres et al., 2002a, 1998]. In recent years aerosol satellite remote sensing has become a priority and dedicated instruments have been developed (MODIS, MISR, POLDER). In addition, instruments designed for other purposes proved useful for aerosol remote sensing because of features such as multiple viewing angle, multiple wavelengths and wavelengths in the UV. Below a brief description for three of these instruments of the new generation is provided because they are used in this thesis.

1.6.1 Advanced Along Track Scanning Radiometer

The Advanced Along Track Scanning Radiometer (AATSR) onboard of ENVISAT is the third instrument in the ATSR series, after ATSR-1 on ERS-1 and ATSR-2 on ERS-2. ENVISAT is in a sun-synchronous polar orbit of about 800-km altitude with an overpass time at 11:00 local solar time. AATSR measures at wavelengths of 0.55 μm, 0.67 μm, 0.87 μm, 1.6 μm, 3.7 μm, 11 μm and 12.0 μm and provides a spatial resolution of $1 \times 1 km^2$ at nadir. The major drawback of AATSR is the small swath of 512 km which results in a return time of approximatly 3 days at mid-latitudes. The major feature of these instruments is the conical scan which provides a dual-view of the Earth's surface, a region is first seen at a zenith angle of 55°and then, approximately 150 s later, at nadir. This geometry provides two different atmospheric path lengths allowing to retrieve independent information about the atmospheric contributions to the signal. In

addition, the dual view can also be useful when assessing the bi-directional reflectance distribution function of different surfaces. Currently, three different algorithms are available for retrieving aerosol optical properties from AATSR measurements.

1. The TNO dual view algorithm. This algorithm is based on the assumption that the ratio between the surface reflectances at nadir and in the forward direction is independent of the wavelength. A detailled description of this algorithm is given Chapter 2.

2. The Swansea University Atmospheric Aerosols Retrieval using Dual_View Angle Reflectance algorithm (AARDVARC, Grey et al. [2006]). This algorithm uses the dual view and a parametrisation of the variation of the land surface reflectance with the viewing angle to retrieve aerosol optical properties.

3. The Oxford-RAL retrieval of Aerosol and Cloud algorithm (ORAC, Thomas et al. [2007]) which is an optimal estimation scheme designed to retrieve aerosol and/or cloud properties from near-nadir satellite radiometers.

1.6.2 Ozone Monitoring Instrument

The Ozone Monitoring Instrument (OMI) derives its heritage from the TOMS instrument. OMI provides daily global coverage. OMI is a nadir viewing spectrometer that measures solar reflected and backscattered light in the UV-Visible domain between 270 nm and 500 nm [Levelt et al., 2006a,b]. OMI reaches global coverage in one day with a 13×24 km ^{2} footprint. The reflectance at the top of the atmosphere measured by OMI is used to derive aerosol optical properties.

Two algorithms have been developed to achieve this goal. The Near-UV algorithm (OMI-AEROsol UltraViolet, OMAERUV, [Torres et al., 2002a]), which uses two wavelengths in the near-UV to provide the aerosol optical depth and the single scattering albedo at 388 nm. The Near-UV method was initially developed to retrieve aerosol properties from TOMS (Total Ozone Mapping Spectrometer) observations and has been upgraded for OMI as explained in Torres et al. [2002b]. The Near-UV method is based on the difference in the sensitivity of the TOA radiation in two wavelength bands to absorbing aerosols such as carbonaceous aerosols or mineral dust and can be applied over any surface. The multi-wavelength method (OMI-AEROsol, OMAERO, [Torres et al., 2002b; Curier et al., 2008b]) is a new approach, which exploits the information in the wider wavelength range between 330 nm and 500 nm. In the current implementation of the multi-wavelength algorithm, 14 wavelength bands between 342.5 nm and 483.5 nm are used. This choice has been made in order to exclude spectral features in the surface albedo related to surface vegetation and ozone absorption features in the UV. The aerosol optical depth is retrieved for a number of aerosol models and a best-fit aerosol model is determined. It has been theoretically shown that the information content in the OMI spectral reflectance measurements in the mentioned wavelength bands provides 2 to 4 degrees of freedom and are sensitive to aerosol parameters such as the aerosol optical depth and the single-scattering albedo [Veihelmann et al., 2007].

1.6.3 MODerate resolution Imaging Spectrometer

The MODerate resolution Imaging Spectrometer (MODIS) onboard of Aqua is part of the A-train constellation. The A-train instruments include among others OMI, MISR, PARASOL, CLOUDSAT and CALIPSO. MODIS also flies

on Terra which is orbiting around the Earth in a descending mode passing across the equator in the morning (10:30 local sun time), while Aqua has a ascending orbit and passes south to north over the equator in the afternoon (13:30 local sun time). MODIS views the surface at $\pm$ 55°with a 2330 km swath, and therefore provides a near daily global coverage. MODIS has 36 channels between 0.44 μm and 15 μm with spatial resolution ranging from 250 m to 1 km. The operational aerosol retrieval algorithm uses 7 wavebands, of which 3 are for retrieval over land, between 0.47 μm and 2.13 μm. This algorithm is a coupling between a land and an ocean algorithm (e.g., Remer et al. [2005]) which assumes that a small set of aerosol types, loadings and sun-satellite geometries can span the entire range of aerosol conditions. Detailed description on the MODIS aerosol retrieval algorithm can be found in Levy et al. [2007a,b].

1.7 Aim and Outline of the work

The work presented in this PhD thesis, was undertaken to improve information on aerosol optical properties using satellite data. Satellite remote sensing of aerosol particles is challenging because the problem of the retrieval of the aerosol properties from the top of the atmosphere radiance is ill-posed. Therefore, several a priori assumptions have to be made on the reflectivity of the surface, the aerosol size distribution and the chemical composition of the aerosol particles to retrieve the aerosol properties that best describe the observations.

Chapter 2 presents the improved TNO DV-AATSR algorithm for aerosol optical properties retrieval from AATSR measurements. The aerosol optical depth derived by means of this algorithm is applied and validated against other measurement-based data (ground and spaceborne) over Western Europe. The

case studies presented in this chapter were partly published in two comparison papers. The first paper presentes a case study over the Venise (Italy) area where results from the TNO DV-AATSR algorithm are compared with result from the application of ORAC to AATSR and MSG-SEVIRI data [Thomas et al., 2007]. The second paper focuses on a scene over Germany where the TNO DV-AATSR algorithm is compared with results from MISR, MODIS and the AARDVARC AATSR algorithm [Kokhanovsky et al., 2008]. An extensive description of the TNO DV-AATSR algorithm is presented in [Curier et al., 2008a], together with several examples of its application and recent progress.

Chapter 3 describes the multi-wavelength algorithm developed to retrieve aerosol optical depth in the UV-visible domain from radiances measured by the OMI. In this study the multi-wavelength algorithm is applied to North Western Europe and evaluated versus ground- and space-based data. This chapter was accepted for publication in the *Journal of Geophysical Reasearch* [Curier et al., 2008b].

The study presented in Chapter 4 was focused on the Amazon basin and has a dual-purpose. First, the multi-wavelength algorithm is tested to established its sensitivity to size distribution and single scattering albedo of several aerosol models representing aerosol particles generated by biomass burning. Second, the sensitivity for the aerosol height layer is investigated using Calipso

Conclusions are presented in Chapter 5; some final remarks are given and possibilities for future work are discussed. In summary, 5 publications form the basis of this thesis, three of which are first author publications. Significant contributions, i.e., all TNO DV-AATSR algorithm retrievials and their description, were made to Thomas et al. [2007]; Kokhanovsky et al. [2008]

Chapter 2

Aerosol Remote Sensing using AATSR observations

This chapter is partly reproduced from an extensive description chapter on the TNO DV-AATSR algorithm [Kokhanovsky and de Leeuw, 2009]: Curier, R.L., G. de Leeuw, P. Kolmonen, A-M. Sundström, L. Sochageva, Y. Bennouna (2008). Aerosol retrieval over land using the ATSR dual-view algorithm. In: A. A. Kokhanovsky and G. de Leeuw (Eds.), Satellite Aerosol Remote Sensing Over Land, Springer-Praxis (Berlin)

Abstract

In this chapter the TNO DV-AATSR algorithm is presented. In a second step two case studies are presented and compared to other measurement-based aerosol optical depth. The first study is a validation of the k-approximation theory, main assumption of the TNO DV-AATSR algorithm. To this end, the aerosol optical depth retrieved are compared to results from both the the AARD-VARC AATSR algorithm and MODIS algorithm. In the second study, the aerosol optical depth retrieved by means of the TNO DV-AATSR algorithm are compared to both result from the Oxford-RAL retrieval of Aerosol and Cloud (ORAC) algorithm applied to AATSR and ground-based measurement for an AATSR overpass of the Northern Adriatic and Po Valley region on September 4^{th}, 2004. After this two study cases, the favorable comparison between the

TNO DV-AATSR algorithm results and other measurement-based results provides confidence in the ability of the TNO DV-AATSR algorithm to retrieve aerosol optical depth.

The most efficient way to follow the variations of the aerosol properties on a global to regional scale is to use remote sensing data [Forster et al., 2007]. Passive remote sensing of aerosols analyzes top of the atmosphere (TOA) radiances, measured by satellite radiometers, to extract aerosol optical properties. In the absence of clouds, the emerging radiance at the top of an aerosol-laden atmosphere can be decomposed into three main contributions:

1. reflection by the surface and transmitted through the atmosphere
2. molecular (Rayleigh) scattering,
3. aerosol scattering.

All three components are affected by transmission and absorption between the height of scattering and the top of the atmosphere. Absorption is due to molecular and aerosol effects. For aerosol retrieval, wavelengths are chosen where molecular absorption is minimal. In the visible and near infra-red domains, the Rayleigh contribution to the total emerging radiance is relatively small as compared to wavelengths in the UV, but not negligible. The surface contribution depends on the surface type, this contribution is very small over dark surfaces such as vegetation in the UV-visible or the sea surface in the visible and near infrared. Over most bright surfaces, the contribution is significant and of similar magnitude or larger than the aerosol contribution, thus the extraction of aerosol information is very difficult without either a precise characterization of the surface, or a method to eliminate the surface effect on the TOA reflectance.

The retrieval of aerosol information from satellite data is done in various steps. The first step is a cloud screening. For clear areas the surface contribution is eliminated, to retain atmospheric contributions to the TOA radiance.

Contributions due to gaseous species can be well-estimated by the use of radiative transfer models, which leave the aerosol contribution to be determined. These steps cannot usually be separated because of cross-terms and a radiative model, including all processes, is used in combination with a retrieval code. Because radiative transfer models are computationally heavy, calculations are made for discrete situations (sun-satellite geometry, aerosol models, etc...) and results are stored in look up tables. In the retrieval code an interpolation is made between look up table situations. Commonly the reflectance ρ is used in retrieval algorithms, it can be derived from the satellite measured radiance L assuming that the surface reflectance is Lambertian and the atmosphere is horizontally uniform:

$$\rho(\lambda) = \frac{\pi \cdot L}{F_0 cos\theta_0} \tag{2.1}$$

where F_0 is the extraterrestrial solar irradiance and θ_0 is the solar zenith angle.

In this chapter the current version of the aerosol retrieval algorithm for AATSR measurements is presented. This algorithm was derived from algorithms developed for application over ocean Veefkind and de Leeuw [1998] and over land Veefkind et al. [1998] for ATSR-2. Both algorithms include multiple scattering and the bi-directional reflectance of the surface. These algorithms were coupled and adjusted for application to ATSR-2 and AATSR data. The major feature of these instruments is the dual-view of the Earth's surface. A scene is first observed at a forward angle of 55°and then, approximately 150 s later, at nadir. AATSR has 7 channels at 0.55, 0.67, 0.87, 1.6, 3.7, 11.0, 12.0 μm and provides a 512 km swath with a resolution of 1×1 km^2 at nadir. The major

drawback of AATSR is the small swath of 512 km which results in a revisit time of approximately three days at mid-latitude.

A schematic description of the algorithm is shown Figure 2.1. The algorithm comprises two main parts: an inversion part (section 2.1) where the actual retrieval is done and a forward part (section 2.2) where all necessary *a priori* data are defined and/or computed using a radiative transfer model.

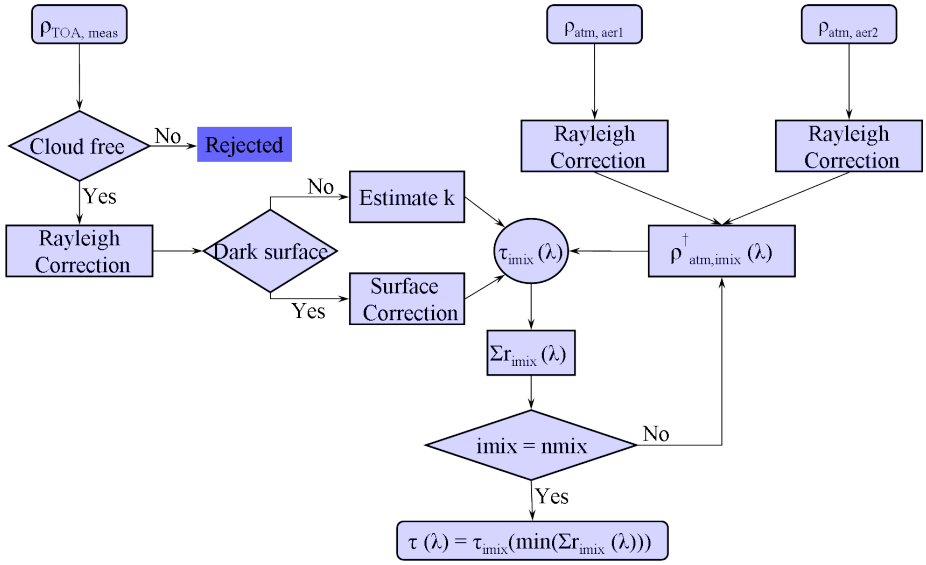

Figure 2.1: Schematic description of the aerosol optical depth retrieval algorithm used at TNO. Coupling of the single view and the dual view algorithms.

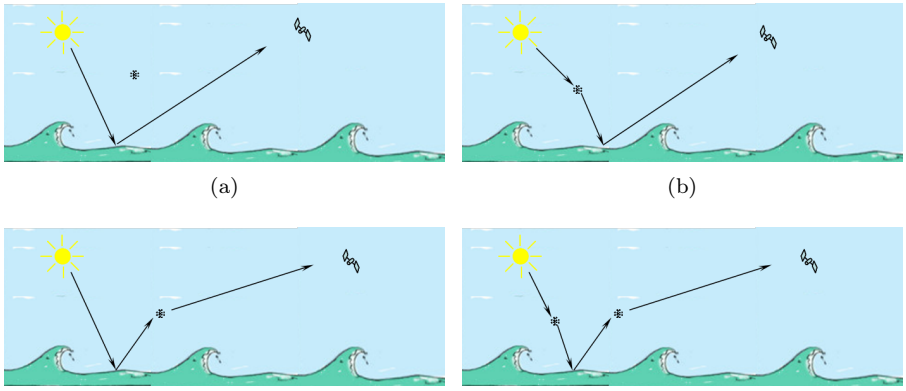

(a) (b) (c) (d)

Figure 2.2: Schematic representation of the different possibilities for the incoming solar radiation to be scattered by both the atmosphere and the surface.

2.1 Inversion Model

2.1.1 Theory

The reflectance measured by AATSR in the visible and NIR domains measured by AATSR at TOA is used to retrieve aerosol optical properties. To retrieve the aerosol contribution, $\rho_{aer,meas}$, the measured TOA reflectance is corrected for the contribution of a Rayleigh atmosphere, ρ_0.

$$\rho_{aer,meas}(\lambda) = \rho_{atm}(\lambda) - \rho_0(\lambda) \tag{2.2}$$

The retrieval procedure is based on two main assumptions:

- The reflectance TOA due to an external mixture of two aerosol types can be approximated as the weighted average of the reflectance TOA of each of the aerosol types [Wang and Gordon, 1994].

$$\begin{aligned}\rho_{aer,imix}(\tau_{ref},\lambda) &= \rho_{aer,meas}(\lambda) + \epsilon_{imix}(\lambda) \\ &= x_{aer_1} \cdot \rho_{aer_1}(\tau_{ref},\lambda) + x_{aer_2} \cdot \rho_{aer_2}(\tau_{ref},\lambda) \end{aligned} \quad (2.3)$$

where ρ_{aer_1} and ρ_{aer_2} are the modeled TOA reflectance due to the presence of each aerosol type. x_{aer_1}, x_{aer_2} are the contribution of each type. ϵ_{imix} accounts for the deviation between the measured, $\rho_{aer,meas}$ and the weighted average, $\rho_{aer,mix}$.

- The reflectance TOA can be expressed as a linear function of the aerosol optical depth with the reflectance of an aerosol free atmosphere as an offset [Durkee et al., 1986].

$$\rho_{atm}(\lambda) = \rho_0(\lambda) + c(\lambda) \cdot \tau(\lambda) \quad (2.4)$$

where ρ_{atm} is the path reflectance due to presence of aerosols and molecules and τ is the aerosol optical depth. Veefkind [1999] demonstrates that Equation 2.4 is a valid assumption for the region of aerosol optical depths characterizing tropospheric aerosols i.e. $\tau \in [0.1\ 0.6]$. For higher aerosol loads the intercept, ρ_0, does not represent solely the Rayleigh scattering and is influenced by the aerosol particles. This assumption leads to biases in retrievals for smaller τ, however, such small values of τ are rare in the observed areas (e.g. industrial, urban, biomass burning, etc...) Moreover, nowadays aerosol optical depth retrieval algorithms are not efficient yet for extremely low aerosol loads over land due to the dominant surface contribution in this case.

The error, in the inversion method used, is introduced by separating the aerosols and molecular scattering and assuming a Lambertian ground reflectance in estimating multiple land/atmosphere scattering, which results in decreasing accuracy at high optical thickness and at steep solar/view angle. The inversion procedure can either use a least square minimization method or a least median square method to fit the modeled reflectance to the satellite measurements. The error function $\sum_l \epsilon^2_{imix}(\lambda_l)$ is minimized to determine the best fit for mixing ratio.

$$\sum_l \epsilon^2_{imix}(\lambda_l) = \sum_{l=1}^{3} \left(\frac{\rho_{aer,meas}(\lambda_l) - \rho_{aer,imix}(\tau_{ref}, \lambda_l)}{\rho_{aer,meas}(\lambda_l)} \right)^2 \tag{2.5}$$

In a cloud free situation, the measured TOA reflectance contains information about both the surface and the atmosphere. For dark surfaces, the surface contribution to the TOA reflectance is computed by reconstructing the bidirectional reflectance of the surface and the aerosol optical depth can be directly determined, Section 2.1.2. Over brighter surfaces, the contribution of the surface reflection and the atmospheric reflection on the TOA reflectance need to be separated. In the dual view algorithm described here, the surface effect is eliminated by taking advantage of the two views of the Along Track Scanning Radiometer, Section 2.1.3

2.1.2 Single view

To derive the aerosol contribution to the TOA reflectance the surface contribution has to be known. The single view algorithm was developed by Veefkind and de Leeuw [1998] to derive aerosol optical depths over dark surfaces, i.e the ocean surface, where the TOA reflectance can be computed using a radiative transfer

model. For a given wavelength and sun satellite geometry, the TOA reflectance measured by the satellite can be expressed as the sum of five contributions.

$$\rho = \underbrace{T_{\downarrow}\rho_{s,dir}T_{\uparrow}}_{1} + \underbrace{t_{\downarrow}\rho_{s,dif_{\downarrow}}T_{\uparrow}}_{2} + \underbrace{T_{\downarrow}\rho_{s,dif_{\uparrow}}t_{\uparrow}}_{3} + \underbrace{t_{\downarrow}\rho_{s,dif_{\uparrow\downarrow}}t_{\uparrow}}_{4} + \underbrace{\rho_{atm}}_{5} \tag{2.6}$$

where ρ_{atm} is the path reflectance by aerosols and molecules, T is the direct transmittance along the upward ($\uparrow$) and downward ($\downarrow$) paths, and t is the diffuse transmittance due to forward scattering by aerosols and molecules. $\rho_{s,dir}$, $\rho_{s,dif_{\downarrow}}$, $\rho_{s,dif_{\uparrow}}$, $\rho_{s,dif_{\uparrow\downarrow}}$, describe the surface bidirectional reflection. In Equation 2.6, the terms 2, 3 and 4 represent the coupled contribution of the surface and the atmosphere. The different possibilities for scattering of the incoming solar radiation by both the atmosphere and the surface are sketched in Figure 2.2.

1. photons are solely reflected by the surface. Figure 2.2(a)
2. photons are scattered by aerosols and/or molecules then reflected by the surface. Figure 2.2(b)
3. photons are reflected by the surface then scattered by aerosols and/or molecules. Figure 2.2(c)
4. photons are scattered by aerosols and/or molecules then reflected by the surface and scattered one more time by aerosols and/or molecules. Figure 2.2(d)
5. photons are scattered and/or absorbed by the atmosphere

The ocean albedo is assumed to be the sum of the subsurface reflection, the reflection on oceanic whitecaps, and specular reflection. $\rho_{s,dir}$, $\rho_{s,dif_{\downarrow}}$, $\rho_{s,dif_{\uparrow}}$,

$\rho_{s,dif_{\uparrow\downarrow}}$, account for each of these processes. For open ocean the subsurface reflection is a function of chlorophyll concentration [Morel, 1988]. The reflection by oceanic whitecaps is taken to be a function of the surface wind speed [Koepke, 1984]. Specular (Fresnel) reflection is computed using the Cox and Munk [1954] sunglint formulas. All components of Equation 2.6 are computed exactly except term 4. As the contribution of term 4 to the TOA reflectance is small, it is assumed that the scattering is isotropic.

Once the measured TOA reflectance is corrected for the surface, the aerosol optical depth can easily be derived from the atmospheric path reflectance, by combining Equations 2.3 and 2.4. The best mixing ratio is used to determine the aerosol optical depth, $\tau(\tau_{ref}, \lambda)$.

$$\tau(\tau_{ref}, \lambda) = \frac{x_{aer_1}\tau_{aer_1}(\tau_{ref}, \lambda) + x_{aer_2}\tau_{aer_2}(\tau_{ref}, \lambda)}{x_{aer_1}\rho_{aer_1}(\tau_{ref}, \lambda) + x_{aer_2}\rho_{aer_2}(\tau_{ref}, \lambda)}\rho_{aer,meas}(\lambda) \tag{2.7}$$

2.1.3 Dual view

The dual view algorithm was developed by Veefkind et al. [1998] for ATSR-2 for aerosol retrieval over land. In the single view algorithm, used over water, the surface reflectance is assumed isotropic, therefore the difference observed in measured TOA radiance can easily be explained by a difference in the atmospheric path length. However, over land, the surface reflectance is usually not isotropic and the surface bidirectional reflectance distribution (BRDF) affects the interactions between the surface and the atmosphere. It is, therefore, necessary to use a more complex model to retrieve the atmospheric contribution to the TOA radiance. Over land the contribution of the surface reflection in the visible to NIR domain is mainly driven by the direct contribution, i.e. photons are reflected at the surface and transmitted through the atmosphere.

On a pixel-by-pixel approach, we assume that the surface can be represented by a Lambertian approximation. The pixel-by-pixel approach allows for introducing the non-Lambertian characteristics of the natural surfaces. The TOA reflectance, ρ, for a Lambertian surface, can be written as [Chandrasekhar, 1960]:

$$\rho(\lambda) = \rho_{atm}(\lambda) + \frac{\rho_{sfc}(\lambda)}{1 - \rho_{sfc}(\lambda) \cdot s(\lambda)} T(\lambda) \tag{2.8}$$

where λ is the wavelength, ρ_{atm} is the atmospheric path reflectance , T is the atmospheric total transmittance, s is the spherical albedo of the atmosphere. The surface reflectance depends both on the wavelength and on the geometry. Flowerdew and Haigh [1995] point out that the angular variation of the surface reflectance is due to the macroscopic structure of the underlying surface, which is of a much larger scale than the wavelength of the incident light. Hence, the surface reflectance is a strong function of the wavelength while its shape is in comparison independent of the wavelength. Therefore, in the dual view algorithm, it is assumed that the ratio between the surface reflectance in the nadir view and the surface reflectance in the forward view, k, is independent of the wavelength. This approach is later referred as the k-approximation

$$k_\lambda = \frac{\rho_{sfc,f}(\lambda)}{\rho_{sfc,n}(\lambda)} \approx k \tag{2.9}$$

The subscripts f and n represent respectively the forward and the nadir view. For $k = 1$, this approximation corresponds to a Lambertian surface approximation.

Using Equation 2.9, the TOA reflectance in the forward view, $\rho_f(\lambda)$, is expressed by:

$$\begin{aligned}\rho_f(\lambda) &= \rho_{atm,f}(\lambda) + \frac{k\cdot\rho_{sfc,n}(\lambda)}{1-k\cdot\rho_{sfc,n}(\lambda)\cdot s(\lambda)}T_f(\lambda) \\ &\approx \rho_{atm,f}(\lambda) + \frac{k\cdot\rho_{sfc,n}(\lambda)}{1-\rho_{sfc,n}(\lambda)\cdot s(\lambda)}T_f(\lambda)\end{aligned} \tag{2.10}$$

In general $k \cdot \rho_{sfc,n}(\lambda) \cdot s(\lambda) << 1$, therefore the TOA reflectance in the forward view, $\rho_f(\lambda)$ can be approximated as:

$$\frac{\rho_{sfc,n}(\lambda)}{1-\rho_{sfc,n}(\lambda)\cdot s(\lambda)} = \frac{\rho_f(\lambda)-\rho_{atm,f}(\lambda)}{k\cdot T_f(\lambda)} = \frac{\rho_n(\lambda)-\rho_{atm,n}(\lambda)}{T_n(\lambda)} \tag{2.11}$$

Assuming that Equation 2.4 applies to the path reflectance, $\rho_{atm,f}$, the aerosol optical depth, $\tau(\tau_{ref},\lambda)$, can be derived using an iterative procedure.

$$\tau^i(\tau_{ref},\lambda) = \frac{\left[\frac{\rho_n(\lambda)-\rho_{0,n}(\tau_{ref},\lambda)}{T_n^{i-1}(\tau_{ref},\lambda)} - \frac{\rho_f(\lambda)-\rho_{0,f}(\tau_{ref},\lambda)}{k^i(\tau_{ref})\cdot T_f^{i-1}(\tau_{ref},\lambda)}\right]}{\left[\frac{c_n(\tau_{ref},\lambda)}{T_n^{i-1}(\tau_{ref},\lambda)} - \frac{c_f(\tau_{ref},\lambda)}{k^i(\tau_{ref})\cdot T_f^{i-1}(\tau_{ref},\lambda)}\right]} \tag{2.12}$$

For most of the continental aerosol types, the aerosol extinction decreases rapidly with the wavelength thus the aerosol optical depth at 1600 nm is small compared to the aerosol optical depth in the visible. The ratio,k, for the $i-th$ iterative step is computed from the 1600 nm channel:

$$k^i = \frac{\rho_f(\lambda=1600nm) - \rho_{atm,f}^{(i-1)}(\lambda=1600nm)}{\rho_n(\lambda=1600nm) - \rho_{atm,n}^{(i-1)}(\lambda=1600nm)} \tag{2.13}$$

The iterative procedure is initiated by ignoring the atmospheric contribution at 1600 nm $\rho_f(\lambda = 1600\ nm) \approx \rho_{sfc,f}(\lambda = 1600\ nm)$. The k-approximation can not be applied to the 865 nm channel because of the strong reflection by

vegetation at this wavelength. The spectral aerosol optical depth, $\tau^i(\tau_{ref}, \lambda)$, is computed using mixtures of two aerosol models. The best aerosol optical depth for the 555, 659, and 1600 nm channels and subsequently the best mixing ratio is determined by applying a least squares minimization as explained in Section 2.1.1.

2.2 Forward Model

The determination of aerosol optical properties from the measured TOA reflectance is an ill posed problem because there is insufficient information to constrain for possible solutions. Therefore, radiative transfer calculations using DAK (Doubling-Adding KNMI, de Haan et al. [1987]) radiative transfer code, are performed to derive the Rayleigh and surface contributions, and a priori assumptions are made on the aerosol. This procedure requires aerosol models describing the aerosol microphysical and optical properties, determined by the chemical composition, to calculate the reflectance at the top of the atmosphere (TOA) using a radiative transfer model.

2.2.1 RTM & LUT

Reflectances and transmissions for Rayleigh atmospheres and atmospheres containing both gases and aerosols were calculated for a set of wavelengths, aerosol concentrations and geometries (solar zenith angle, viewing zenith angle, relative azimuth angles). Table 2.1 presents the amounts of tiepoints used for each dimension. The results are stored in look-up tables (LUT), these tables contain nine calculated variables, an overview of the variables stored in the LUT as

well as their dimensions is given in Table 2.2. By using look-up tables, bidirectional reflectance and multiple scattering are accounted for, while the algorithm computational speed is not affected.

The radiative transfer model used at TNO is the DAK model (Doubling-Adding KNMI, de Haan et al. [1987], Stammes [2000]) developed at KNMI. DAK makes use of the doubling adding method, a two step process. Calculations start with a very thin atmospheric layer which has only single-scattering properties. An identical layer is then introduced, the optical properties of the combined layer are calculated and internal scattering is included. This step is the "doubling" one. The doubling step will be repeated until the layer has reached the required thickness. Multiple scattering is thus taken into account. The "adding" step is a similar mechanism designed to handle layers with different optical properties. These layers are combined in a single one which will be added to a third layer and so on. The "adding" is assumed completed when the boundary fluxes of the modeled layers converge. In this study, each input parameter was set to achieve a 4 or 5 decimal accuracy.

Table 2.1: Overview of the layout of the different LUTs. Each variable represents the axis of the multi-dimensional grid. The different parameter contains in each LUT can be found in Table 2.2

Variable name	symbol	units	amount	entries
wavelength	λ	nm	4	555, 659, 865, 1600
solar zenith angle	μ_0	degree	15	0.15, 0.2, 0.25, ..., 0.65, 0.7, 0.8, 0.9, 1.
view zenith angle	μ	degree	15	0.15, 0.2, 0.25, ..., 0.65, 0.7, 0.8, 0.9, 1.
relative azimuth angle	$\Delta\phi$	degree	19	0., 10., 20., ..., 180.
aerosol optical depth at 500 nm	τ_{500}	-	10	0.05, 0.1, 0.25, 0.5, 1., 1.5, 2., 2.5, 3., 4.

Table 2.2: Variables and dimensions for the data stored in the different LUTs.

Variable name	Symbol	Dimension
Path reflectance	ρ_{atm}	$\mathrm{p}_s, \lambda, \mu_0, \mu, \Delta\phi, \tau_{500}$
Surface downward reflectance	ρ_d	$\mathrm{p}_s, \lambda, \mu_0, \mu, \Delta\phi, \tau_{500}$
Total transmittance	T	$\mathrm{p}_s, \lambda, \mu_0, \mu, \tau_{500}$
Total diffuse transmittance	t	$\mathrm{p}_s, \lambda, \mu_0, \mu, \tau_{500}$
Diffuse transmittance down	$\mathrm{t}_\downarrow$	$\mathrm{p}_s, \lambda, \mu_0, \mu, \tau_{500}$
Total transmittance down	$\mathrm{T}_{tot\downarrow}$	$\mathrm{p}_s, \lambda, \mu_0, \mu, \tau_{500}$
Spherical albedo	s	$\mathrm{p}_s, \lambda, \tau_{500}$
Aerosol optical thickness	τ	λ, τ_{500}

2.2.2 Aerosol Description

In this section, the microphysical and chemical properties of the aerosols used for the look up tables are described. The aerosol particles are assumed spherical, which allows for the application of the Mie theory [Mie, 1908] to compute the optical properties. This assumption is justified because most atmospheric particles are hygroscopic and thus contain water when the relative humidity is above a certain threshold value (desliquescence point). Due to hysteresis, once the particles have absorbed water vapor, they remain wet unless the relative humidity drops below a certain value where crystallization occurs. For common atmospheric aerosol particles the crystallisation point occurs at very low relative humidity (for discussion cf. Seinfeld and Pandis [1998] and references therein). Hence, it is assumed that most atmospheric aerosol particles are a solution. Dust particles are an exception and should be treated as non-spherical particles. The aerosol size distribution is described by an n-mode lognormal distribution.

$$\frac{dN}{dln\ r} = \sum_{i=1}^{n} \frac{N_i}{(2\pi)^{\frac{1}{2}}\ ln\ \sigma_i} \exp\left(-\frac{(ln\ r_i - ln\ \overline{r}_{gi})^2}{2\ ln^2\ \sigma_i}\right) \tag{2.14}$$

where N_i is the number concentration, $\overline{r}_{gi}$ is the mean geometric radius and σ_i, the standard deviation of the i-th lognormal mode.

Look up tables were computed for four aerosol models, using field campaign measurements and/or literature data:

1. *Continental Background.* This model represents the aerosol background in industrial or urban areas. It has a tri-modal distribution. The chemical composition is defined according to the work of Heintzenberg [1989] distinguishing between water soluble inorganic, non water soluble inorganic

and organic fractions. The complex refractive index is derived from the chemical composition using Maxwell-Garnet mixing rules (Chylek, 1993) and the complex refractive index of each main fraction is given by Hess et al. [1998].

2. *Anthropogenic particles.* Monomodal lognormal distribution representing the aerosol particles from anthropogenic origin. Veefkind [1999]

3. *Sea spray.* Bimodal lognormal distribution. de Leeuw et al. [1989]

4. *Biomass burning.* The size distribution of aerosol particles originating from biomass burning is described as a tri-modal lognormal distribution [Quinn et al., 2002; Anderson et al., 1996]. The complex refractive index is defined following Haywood et al. [2003].

Detailed information on the aerosol models, such as geometric mean radii r_g, geometric standard deviation σ_g, complex refractive index and the mode's fraction are presented in Table 2.3.

Table 2.3: Physical and optical properties of the aerosol models used to build the LUT. The complex refractive index, n, is given for $\lambda = 555\ nm$. x represents the mass fraction for each mode.

Name	mode	R	$ln\ \sigma$	x	n_r	n_i
Continental background	m_1	0.010	0.161	0.4	1.44	0.0039
	m_2	0.058	0.217	72	1.44	0.0039
	m_3	0.900	0.380	28	1.44	0.0039
Biomass Bruning	m_1	0.085	0.161	85	1.54	0.0180
	m_2	0.395	0.217	3	1.54	0.0180
	m_3	1.200	0.380	12	1.53	0.0080
Sea spray	m_1	0.070	0.460	25	1.38	5.38×10^{-9}
	m_2	0.389	0.370	75	1.38	5.38×10^{-9}
Anthropogenic	m_1	0.030	0.139	100	1.41	0.00241

2.3 Automatic Cloud Screening

In the presence of clouds, the aerosol contribution to the TOA reflectance is completely masked by the cloud contribution. Therefore, aerosol properties can be retrieved only over cloud free areas. To discriminate between cloudy and clear pixels from ATSR-2 data a semi-automatic algorithm for cloud screening over land has been adapted that follows from Koelemeijer et al. [2001] and is based on the work of Saunders and Kriebel [1988]. The procedure applies four standard cloud detection tests, as described below. This algorithm is time consuming, as it requires manual interference, and therefore has been automated by Robles Gonzalez [2003] for application over large areas and for longer periods. This cloud screening is a pixel by pixel process, a pixel is classified as clear if and only if all tests indicate the absence of clouds. These tests are based on histogram evaluation of either brightness temperature or reflectance. To determine whether a pixel is cloud contaminated, thresholds are set. The threshold depends on the surface properties, the day to day variation of the meteorological condition, as well as sun-satellite geometry. Clearly, threshold values must be carefully chosen. Therefore, this threshold is determined for each 512×512 frame. The threshold value for each histogram is determined in two steps. First, a Fast Fourier Transform low-pass filter is applied to smooth the data. Then the extrema (maximum, minimum and inflexion points) of the smooth histogram are computed by applying a modified Lagrange interpolation, and from this set of extrema each test's threshold is determined.

The first test, T1, is the gross cloud test. It uses the 12 μm channel and makes use of the fact that the temperature of the atmosphere decreases with altitude, so the temperature of an an optically thick cloud at high altitude will

be significantly less than the surface temperature. If the measured brightness temperature is below the set threshold, the pixel is marked as cloudy.

The second test, T3, exploits the fact that clouds are brighter than the underlying surfaces and checks the reflectance at 659 nm for each pixel. Cloudy pixels will present a higher reflectance than non-cloudy pixels. For each frame reflectances are histogrammed and a threshold is selected to discriminate between cloudy and clear pixels.

The third test, T4, is a reflectance ratio at 865 nm and 659 nm test. It is based on the difference between the spectral behavior of the surface and the cloud at these wavelengths. Indeed, cloud reflectances are similar in these channels whereas surface reflectances are generally different. Over land the surface reflectance at 865 nm tends to be higher than the one at 659 nm while over water the reflectance at 659 nm tends to be higher than the one at 865 nm. Therefore, three cases can be observed: a reflectance ratio of 1 which denotes the presence of clouds, a reflectance ratio lower than 1 characterizes water surfaces whereas land surfaces feature a ratio higher than one.

The fourth test, T5, is made to detect semi-transparent clouds such as cirrus for which the difference between the brightness temperature at 12μm and the brightness temperature at 11μm is large. The temperature difference is computed for each pixel and compared to a tabulated threshold value. When the difference exceeds the threshold, the pixel is flagged as cloudy. This last test must be used carefully and is not used for the analysis of large amounts of data.

2.3.1 Cloud Screening: Example

Figure 2.3(a) shows the cloud mask derived for August 10^{th}2004. The pixels flagged as clear by all tests are colored in blue, whereas all other pixels have

been detected as cloudy by one or more tests. Table 2.4 presents a description of the different values of the cloud quality flag. Figure 2.3(b) is an RGB picture of the same day from MODIS where clouds are visible. The similar pattern in the derived cloud mask and the RGB picture derived from MODIS provides confidence in the cloud screening. For a more quantitative study the cloudmask derived from AATSR data is compared to the cloudmask provided for MODIS, [Ackerman et al., 2002]. Figure 2.4(a) is a composite map which presents a comparison of the cloudmask derived from MODIS [Ackerman et al., 2002] and the cloudmask derived from AATSR data. In order to derive this composite map, the AATSR derived cloudmask has been meshed into the MODIS cloudmask grid. In the case of the TNO DV-AATSR algorithm, the cloud screening protocol designates pixels either as cloudy or as clear, whereas the MODIS cloud screening protocol flags pixels in four different ways, cloudy, probably cloudy, probably clear or clear. Thus, each pixel information from AATSR and MODIS have been combined into an unsigned integer, e.g. the two first bits code for MODIS cloudmask and the third one for the AATSR cloudmask. The flag description is summarized in Table 2.5 which also includes the interpretation for each observed value in the combined cloudmask, Figure 2.4(a). Figure 2.4(b) is a histogram of the available pixels for this comparison. It can be seen that 83. % of the pixels has been flagged the same way by each cloud screening protocol. The cloudmasks were in complete disagreement for 12 % of the pixels. For 5 % of the pixels the comparison is not conclusive as the pixels were flagged as probably clear or probably cloudy by MODIS.

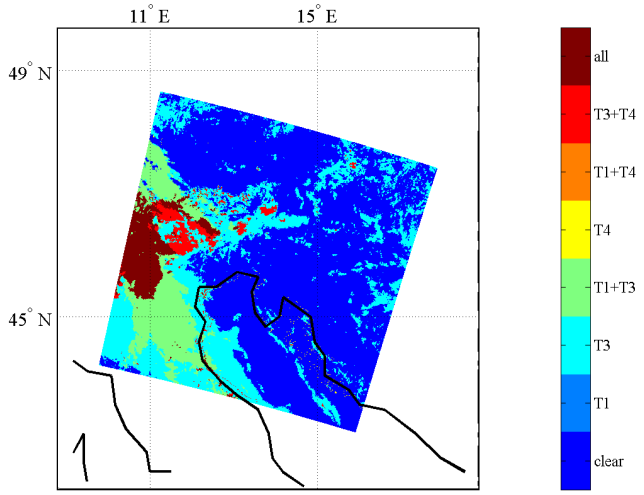

(a) AATSR at 1x1km

(b) modis RGB picture

Figure 2.3: The upper panel is the a composite map of the cloud mask derived by the cloud screening protocol described in Section 2.3 for August 10^{th}, 2004. The lower panel is a RGB picture derived from channels 1, 3 and 4 of MODIS for August 10^{th}, 2004. Pixels determined cloudy by all tests are red. Clear pixels are blue. See Table 2.4 for detailed information on colorbar

Table 2.4: Flag description of the cloudmask derived from AATSR data in Figure 2.3(a)

Flag number	Interpretation
Clear	clear
T1	flag by test 1
T3	flag by test 2
T1+T3	flag by test 1 and 2
T4	flag by test 3
T1+T4	flag by test 1 and 3
T3+T4	flag by test 2 and 3
All	flag by all test

Table 2.5: Flag description of the combined cloudmask in Figure 2.4

MODIS	AATSR	COMBINED	Interpretation
0	0	0	clear for AATSR and MODIS
1	0	1	probably clear for MODIS, clear for AATSR
2	0	2	probably cloudy for MODIS, clear for AATSR
3	0	3	cloudy for MODIS, clear for AATSR
0	1	4	clear for MODIS, cloudy for AATSR
1	1	5	probably clear for MODIS, cloudy for AATSR
2	1	6	probably cloudy for MODIS, cloudy for AATSR
3	1	7	cloudy for AATSR and MODIS

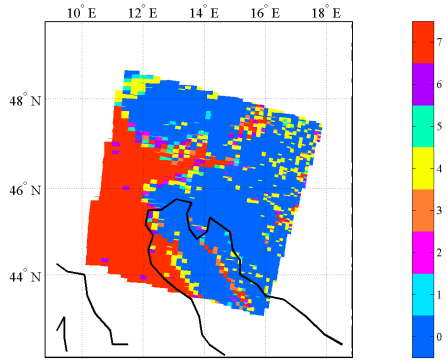

(a)

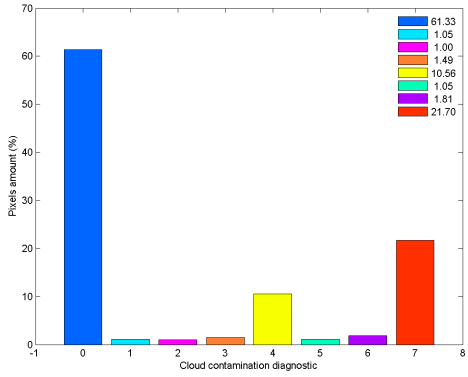

(b)

Figure 2.4: Comparison of the AATSR and MODIS cloud screening for August 10^{th} 2004. Dark blue and red represent pixels when AATSR and MODIS diagnostics agree. Orange and yellow are representative for pixels when AATSR and MODIS disagree. The left panel is a composite map of the combined cloudmask. The right panel is an histogram of the number of pixels versus the cloudmask flag. In Table 2.5, a description of the combined cloudmask is given

2.4 Validation of the k-approximation theory

Figure 2.5(a) is a composite map of the aerosol optical depth derived at 555 nm, over Germany for October 13^{th} 2005. The spatial resolution is a 1×1 km^2 at nadir. The aerosol optical depth derived is low and ranges from 0.07 to 0.23, with a mean aerosol optical depth of 0.15. The observed aerosol optical depth pattern is a mixture of continental background aerosol (blue color) and aerosol originating from human activities but also natural causes such as wind-blown-dust, sea spray (green color). Some higher values are observed in or near cloud areas, likely due to residual cloud contamination, illumination of aerosol from a cloud side (3-D effects), or due to enhanced relative humidity in these areas causing swelling and thus elevated extinction. Statistical methods are tested to remove such pixels or flag them as suspect of cloud influences.

Figure 2.5(b) presents a comparison between the mean aerosol optical depth retrieved (filled circles) and their measured counterparts (open circles) for Hamburg, Leipzig and Mainz. The results compare favorably with the AERONET measured aerosol optical depth and are within the aerosol optical depth uncertainty of 0.05 , for ATSR-2 [Robles-Gonzalez et al., 2006].

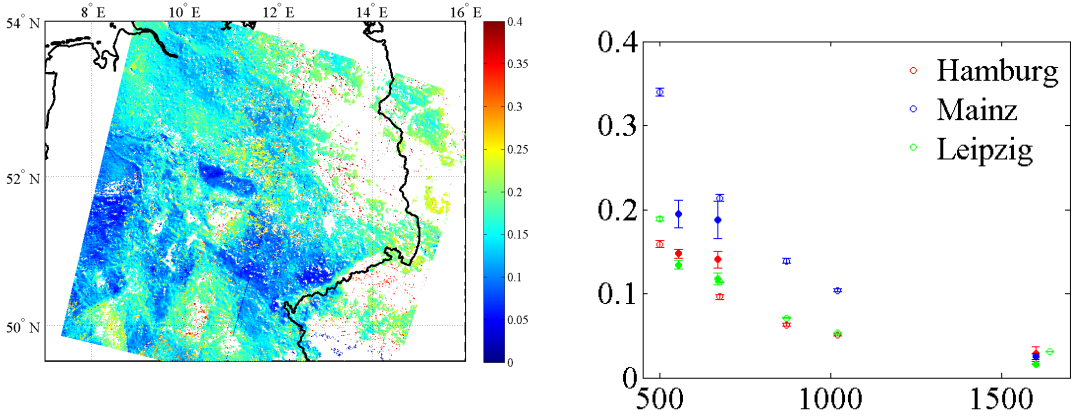

Figure 2.5: Left: composite map of the aerosol optical depth, derived from AATSR measurement at 555 nm, over Germany for October 13^{th} 2005, with a 1×1 km^2 resolution. Right: Comparison of the mean aerosol optical depth retrieved using the dual-view algorithm (filled circles) and from sun-photometer data (open circles) for selected AERONET stations. Error bars indicate the spatial standard deviation for the mean aerosol optical depth retrieved within a radius of 2km around the AERONET site and the temporal standard deviation of the mean aerosol optical depth measured by ground based sun-photometers.

A comparison study by North et al. [1999] indicates that the use of the k-approximation constraint resulted in a mean absolute error of 0.029 for an aerosol optical depth of 0.1. A model constraint based on the decomposition of the angular effects, an isotropic term which is wavelength dependent and an anisotropic term which is independent of wavelength, resulted in a mean absolute error of 0.007 for an aerosol optical depth of 0.1. However, when the reflectance is a mixture of atmospheric and surface scattering, this constraint does not correctly represent the surface as the anisotropic term is not wavelength-independent. The data in Figure 2.6 were used in a intercomparison study over Germany for 13 October 2005, between the dual-view algorithm earlier described (See 2.1.3) and the Swansea University AARDVARC (Atmospheric Aerosols Retrieval using Dual_View Angle Reflectance Channels) algorithm which applies the models constraint [Grey et al., 2006; Kokhanovsky et al., 2008]. Each algorithm uses the same AATSR datasets to produce the aerosol optical depth, therefore the existing differences in the aerosol optical depth are solely induced by differences in the processing schemes.

First, the algorithms have independent cloud screening and sampling protocol. Thus, different radiances are ingested by the algorithms depending on masking and pixel aggregation. Second, the parameterizations of aerosol chemical and optical properties used to constrain the inverse problem contains different assumptions. Third, the atmospheric radiative transfer models used are different, the Swansea University AARDVARC algorithm uses the Second Simulation of the Satellite Signature in the Solar Spectrum (6S) of Vermote [1997] whereas the TNO DV-AATSR algorithm uses DAK. Fourth, the sampling of the look up tables of atmospheric parameters influences the aerosol retrievals. Finally, the a-priori constraint used to account for the surface reflectance is not the

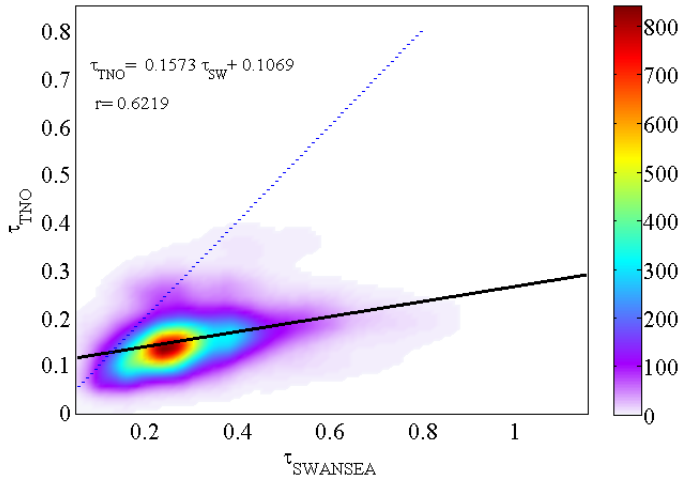

Figure 2.6: Scatter density plot of the mean aerosol optical depth derived from TNO dual view algorithm and the mean aerosol optical depth derived from Swansea University AARDVARC algorithm at 555 nm, over Germany for October 13^{th} 2005.

same. Thus, the variation between the algorithms themselves and the assumptions upon which they are based will result in different estimates of the surface and atmospheric reflectance. Figure 2.6(a) present a comparison between the aerosol optical depth derived by these two different dual view algorithms. The aerosol optical depth derived using the Swansea University AARDVARC algorithm, provided on a 10×10 km^2 grid, were meshed into the 1×1 km^2 grid used by the TNO dual-view algorithm, using a linear interpolation. Similar to the TNO AATSR algorithm, the Swansea University AARDVARC algorithm derived a mean aerosol optical depth of 0.15 for the region of interest.

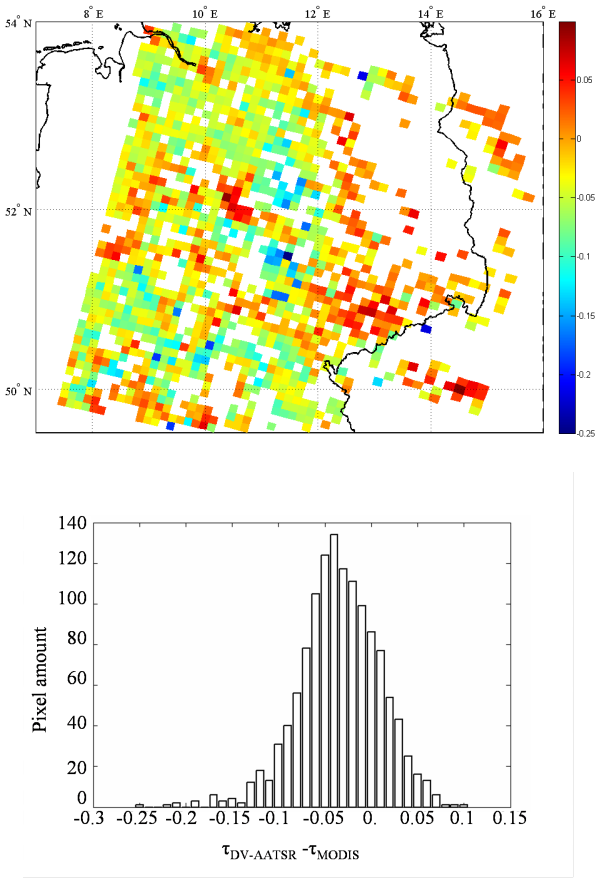

Figure 2.7: Left:Composite map of the difference between the aerosol optical depth derived by MODIS and the aerosol optical depth derived by means of the TNO DV-AATSR algorithm, over Germany for October 13^{th} 2005. Right : Histogram of this difference, where the number of pixels is plotted as a function of the difference in aerosol optical depth.

Table 2.6: Direct comparison of aerosol optical depth derived for Hamburg, Leipzig and Mainz at 555nm for 13 October 2005.

location	aod_{AER}	aod_{MODIS}	aod_{TNO}	aod_{SW}
Hamburg	0.16	0.15± 0.01	0.13± 0.02	0.25± 0.05
Mainz	0.34	0.19± 0.03	0.21± 0.02	0.42± 0.09
Leipzig	0.19	0.13± 0.01	0.15± 0.03	0.26± 0.03

AATSR on board of ENVISAT and MODIS on board of TERRA overpass the same area within 30 minutes. Thus an exact temporal match is not possible. However, the time span is small enough to assume that it is unlikely to observe large changes in the aerosol optical depth. Figure 2.7(a) presents a comparison with the aerosol optical depth derived using MODIS (TERRA, collection 5). In order to compare the aerosol optical depth, the TNO AATSR algorithm results were meshed within the MODIS grid (10×10 km^2). The overlapping area contains information for 1283 pixels. The datasets compare favorably, with a homogeneous distribution of the difference. The TNO AATSR algorithm appears to overestimate the aerosol optical depth in about 75% of the pixels with respect to MODIS. Figure 2.7(b) presents the distribution of this difference, showing that for 69 % of the pixels, the absolute value of difference is lower than the 0.05 uncertainty derived by Robles-Gonzalez et al. [2006].

Table 2.6 summarizes the aerosol optical depth derived by each measurement-based algorithm for 3 AERONET sites over Germany for October 13^{th} 2005.

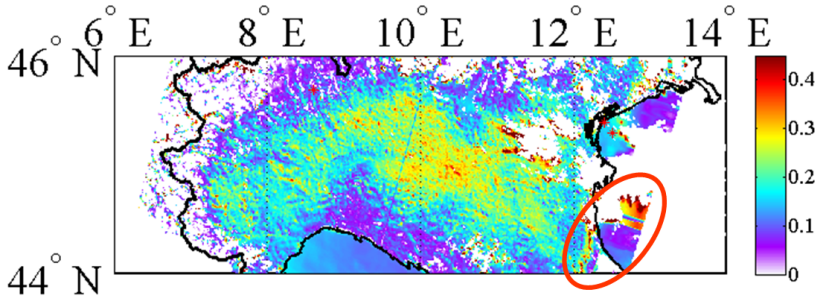

Figure 2.8: Composite map of the aerosol optical depth derived by means of the TNO AATSR algorithm, over the Po Valley, Northern Italy, for September 4^{th} 2004. White areas indicates that no data were computed due to cloud occurrences. Red crosses mark Ispra (45.7°N 8.6°S), Nicelli (45.4°N 12.4°S) and Venice (45.3°N 12.5°S).

2.5 Application and comparison

Figure 2.8 is a composite map of the aerosol optical depth derived by means of the TNO AATSR algorithm, over the Po Valley for September 4^{th} 2004. Strong aerosol optical depth gradients are observed with values varying form about 0.1 near the Alps to about 0.5 in the Central Po Valley. This variability is caused by the presence of the Alps barrier, the aerosols produced in industrialized areas as Milan and Turin, can only be evacuated trough the Po valley to the Adriatic Sea. As observed in the validation study over Germany for October 13^{th} 2005, an unreasonable increase of the aerosol optical depths occurs at the edges of area flagged as cloudy. The eastern edge (marked by the red circle) of the composite map presents some unrealistic pattern. The source of these artifacts, once flagged as sunglint contamination, has not been found. These artifacts seem to be a peculiar feature of this specific scene, as similar artifacts have not been encountered in other processed scenes. The land-sea transition over

Table 2.7: Direct comparison of aerosol optical depths derived at 555nm for September 4^{th}. The aerosol optical depths retrieved by means of the TNO DV-AATSR algorithm were averaged over 5 km around the ground measurement sites. The AERONET values are averaged over ± 30 minutes of the AATSR overpass. The closest MODIS values available within a maximum of 10 km was used.

station	aod_{TNO}	aod_{AER}	aod_{MODIS}
Ispra	0.10 ±0.04	0.26 ±0.01	0.12
Venice	0.18 ±0.02	0.15 ±0.01	—
Nicelli	0.16 ±0.02	0.17 ±0.01	0.26

the coastline of the Adriatic sea is smooth and shows little evidence of a sudden change in the aerosol burden and probably represents the aerosol advection from land. On the other hand, the land-sea transition observed over the coastline of the Ligurian sea shows a discontinuity with a severe increase of the aerosol optical depth.

Table 2.7 is a direct comparison with the measured aerosol optical depth for three AERONET ground measurement sites, Ispra (45.7°N 8.6°S), Nicelli (45.4°N 12.4°S) and Venice (45.3°N 12.5°S). The AERONET averaged aerosol optical depths within ± 30 minutes of an AATSR overpass are have been compared to derived aerosol optical depths averaged over 5 km.

The averaged aerosol optical depth derived for Ispra is overestimated by a factor of 2.6. It appears from Figure 2.8 that the aerosol optical depth derived in the area around the measurement site was quite heterogeneous. By reducing the averaging area, and considering only values within 1 km of the ground site measurement, the averaged aerosol optical depths retrieved over the Ispra site is 0.144 ± 0.006, i.e. within experimental error. The averaged aerosol optical

depth derived for Nicelli and Venice compare well with the AERONET averaged aerosol optical depth. The averaged aerosol optical depth derived by means of the TNO AATSR algorithm are, for the Venice and Nicelli sites, within the standard deviation of the AERONET measurements. Once more it is worthwhile to point out that the aerosol optical depths are retrieved within the 0.05 uncertainty prescribed by Robles-Gonzalez et al. [2006] for the ATSR-2 instruments.

The aerosol optical depths derived in this study were used in a comparison study by Thomas et al. [2007] between the Oxford-RAL retrieval of Aerosol and Cloud (ORAC) and TNO AATSR algorithms. It has been denoted a general overestimation and an unrealistic degree of scatter in the aerosol optical depth resulting from the ORAC algorithm over land. The amount of ocean pixels in the observed area were not sufficient to draw a definitive conclusion, but the two algorithms seem to compare better than over land.

2.6 Conclusion

In this chapter the TNO AATSR algorithm was presented. This algorithm resulted from an upgrade and coupling of the single view and dual view algorithm developed by Veefkind and de Leeuw [1998] and Veefkind et al. [1998] for ATSR-2.

The cloud screening protocol, developed for the algorithm, is found to be satisfactory with the AATSR algorithm and MODIS cloud masks agreeing in 83. % of the conclusive cases. The sensitivity of the cloud screening protocol for various conditions (i.e. desert, forest fire) remains to be explored. The aerosol optical depth estimated using the TNO AATSR algorithm has been

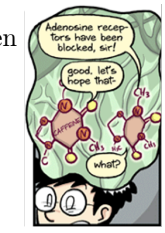

compared with results from the Swansea University AARDVARC algorithm, MODIS and AERONET for an area over Germany. The favorable comparison provides confidence in the ability of the TNO AATSR algorithm to retrieve aerosol optical depth. An application case study was presented for September 4^{th}, 2004 over the Po Valley, Northern Italy. The results compare favorably with ground based measurements. Land-sea transition areas remain an issue in the current implementation of the TNO AATSR algorithm.

The ATSR-2 single and dual view algorithms have already been tested over areas such as North America [Veefkind and de Leeuw, 1998; Veefkind et al., 1998], Central and South Africa [Robles-Gonzalez and G. de Leeuw, 2007], India and the Indian Ocean [Robles-Gonzalez et al., 2006] and also over bright desert surfaces [de Leeuw et al., 2005]. These tests should be repeated to further validate the new TNO AATSR algorithm.

Chapter 3

Aerosol optical depth over Western Europe using OMI

This chapter was accepted for publication in the Journal of Geophysical Reasearch: Curier, R. L.; Veefkind, J.; Braak, R.; Veihelmann, B.; Torres, O. and de Leeuw, G. Retrieval of aerosol optical properties from OMI radiances using a multi-wavelength algorithm:Application to Western Europe. Accepted for publication in J. Geophys. Res., 2008

Abstract

The OMI multi-wavelength algorithm has been developed to retrieve aerosol optical depth using OMI measured reflectance at the top of the atmosphere. This algorithm was further developed by using surface reflectance data from a field campaign in Cabauw (The Netherlands), a new cloud screening method and a global aerosol database derived from the aerosol transport model TM5. The first results from an application of this algorithm over Western Europe are presented. The OMI retrieved aerosol optical depth is evaluated by comparison with both ground based measurements from AERONET and MODIS satellite data. The various aerosol optical depth values compare favorably, except in situations where large changes occur in the surface properties, which is illustrated over the Iberian peninsula. OMI and MODIS aerosol optical depth are well-correlated

(with a correlation coefficient of 0.66 over land and 0.79 over sea), although the multi-wavelength algorithm appears to overestimate the aerosol optical depth values with respect to MODIS. The multi-wavelength algorithm performs better over sea than over land. Qualitatively, the multi-wavelength algorithm well reproduces the expected spatial aerosol optical depth gradient over Western Europe.

3.1 Introduction

THE influence of aerosols on the Earth's radiative balance is one of the largest unknowns in the climate system. Aerosols have a direct effect by scattering and/or absorbing the incoming solar radiation The aerosols' net effect on the Earth's radiative balance depends on the aerosol chemical and physical properties, the surface albedo and the aerosol layer's altitude [Torres et al., 1998]. The uncertainty in the effect of aerosols on climate stems from the large variability of aerosol sources, i.e. their concentrations and physical, chemical and optical properties, in combination with their short atmospheric residence time of a few days. Experimental data on aerosol properties are available from ground based observations. However, they often are only representative for local situations and cannot be used for estimates of effects on regional to global scales. Furthermore, they are part of several networks which often are disconnected and the data are available in different formats, on different time scales and measured using different procedures and correction factors. Although efforts have been made to harmonize some of these datasets (e.g. GAW[1] and EMEP[2]), the data availability on a global or regional scale is still a concern. Furthermore, the area coverage is very sparse for most continents. An alternative to provide aerosol properties on a regional to global scale with a spatial resolution varying from 1×1 km^2 to $1^\circ\times 1^\circ$ and a temporal resolution of once per day is provided by sun synchronous satellites. Satellite data insure the creation of worldwide aerosol database properties derived from the same protocol. The use of satellites is

[1] Global Atmosphere Watch program of the World Meteorological Organisation (WMO), www.wmo.ch/web/arep/gaw/gaw_home.html

[2] co-operative program for monitoring and evaluation of the long-range transmission of air pollutants in Europe through the european project CREATE, http://www.gse-promote.org/services/create/createdb.html

complementary to the ground based networks for extension to larger spatial scales, even though the satellite retrieved aerosol properties do not provide the same detail and accuracy as ground based in situ measurements and lack vertical resolution (except for space borne lidars such as the Cloud-Aerosol Lidar with Orthogonal Polarization (CALIOP)).

OMI is a Dutch-Finnish contribution to the Aura mission, [Schoeberl et al., 2006]. It is a nadir viewing spectrometer that measures solar reflected and backscattered light in the UV-Visible domain between 270 nm and 500 nm [Levelt et al. 2006a and 2006b]. The reflectance at the top of the atmosphere (TOA) measured by OMI is used to derive aerosol optical properties, two algorithms have been developed to achieve this goal. The Near-UV algorithm (OMI-AEROsol UltraViolet, OMAERUV, [Torres et al., 2002a]), which uses two wavelengths in the near-UV to provide the aerosol optical depth and the single scattering albedo at 388 nm. The Near-UV method was initially developed to retrieve aerosol properties from TOMS (Total Ozone Mapping Spectrometer) observations and has been upgraded for OMI as explained in Torres et al. [2002b]. The Near-UV method is based on the difference in the sensitivity of the TOA radiation at two wavelength bands to absorbing aerosols such as carbonaceous aerosols or mineral dust and can be applied over any surface. The multi-wavelength method (OMI-AEROsol, OMAERO) is a new approach, which exploits the information in the wider wavelength range between 330 nm and 500 nm. In the current implementation of the multi-wavelength algorithm, 14 wavelength bands between 342.5 nm and 483.5 nm are used. This choice has been made in order to exclude spectral features in the surface albedo related to surface vegetation and ozone absorption features in the UV. The aerosol optical depth is retrieved for a number of aerosols models and a best fitting aerosol

model is determined. It has been theoretically shown that OMI spectral reflectance measurements in the mentioned wavelength bands contain between 2 and 4 degrees of freedom and are sensitive to aerosol parameters such as the aerosol optical depth and the single-scattering albedo [Veihelmann et al., 2007].

The main goal of this study is to validate the aerosol optical depth output of the multi-wavelength algorithm, therefore, in agreement with the study made by Veihelmann et al. [2007], which pointed out the redundancy of the information content in the nominal wavelengths, the retrievals in this study were made over Western Europe for May to July 2005 for eight wavelengths of 342.5, 367.0, 388.0, 406.0, 425.5, 442.0, 463.0, and 471.0 nm. The aerosol optical depth provides information on the total concentration of particles for a given size range and its spectral variation provides an indication of the particle size distribution.

In the near ultraviolet and visible domains the net aerosol effect on the TOA radiation results from complex interactions between several competing radiative processes: the scattering and absorption of incoming solar radiation by molecules and aerosols, the absorption of the scattered radiation, scattering and absorption of radiation reflected by the underlying surface. For OMI wavelengths in the near UV and the visible almost all surfaces, (except ice, snow, desert and salt lakes), have low surface albedo. Therefore, for cloud-free skies, the TOA radiance is dominated by atmospheric effects, i.e. molecular and aerosol scattering and absorption.

In this paper, we present the first results from the retrieval of aerosol optical depth from application of the multi-wavelength algorithm [Torres et al., 2002b] to OMI (Ozone Monitoring Instrument) data over Western Europe for May to July 2005. An extended version of the multi-wavelength algorithm is presented and validated. Section 3.2 gives an overview of the different aerosol

properties present in the OMAERO product derived from the multi-wavelength algorithm. The extended version of the multi-wavelength algorithm required an improvement of the cloud screening, an evaluation of the surface albedo effects on the TOA reflectance and the introduction of an improved aerosol climatology. The surface albedo was evaluated based on experimental data. The cloud screening has been enhanced by the synergistic use of MODIS (Moderate Resolution Imaging Spectrometer) and OMI cloud masks. And finally, the aerosol geographical distribution has been improved using an aerosol transport model. The multi-wavelength method as well as the different adjustments are explained in Section 3.3. Results are presented in Section 3.4. The aerosol optical depth time series for ten European sites are presented and evaluated versus AErosol RObotic NETwork (AERONET) data [Holben et al., 1998] in Section 3.4.1. In Sections 3.4.2 and 3.4.3, the OMI retrieved aerosol optical depth is compared to MODIS retrieved aerosol optical depth and the spatial variation of the aerosol optical depth over Europe is evaluated based on monthly composite maps.

3.2 The OMI Aerosol Product OMAERO

OMI measurements are unique, they are sensitive to aerosol absorption in the UV and, at the same time, combine a small footprint (13 km $\times$ 24 km at nadir) with global coverage. The small footprint is essential for the observation of tropospheric aerosols. The UV-absorption facilitates the distinction of aerosols types such as desert dust and biomass burning from other aerosol types.

The OMI multi-wavelength algorithm, OMAERO, provides aerosol optical depth, τ, and the most probable aerosol model for a given spectral reflectance measurement. The product comprises also the single-scattering albedo ω_0, layer

height and the size distribution associated with the best fitting aerosol model. In addition, the aerosol indices in the UV and in the visible range for the main aerosol type are given for both clear and cloudy pixels.

The extinction coefficient, σ_{ex}, describes the extinction of the incoming radiation at wavelength, λ, per unit length due to scattering and absorption by particles. σ_{ex} is expressed in km^{-1}

$$\sigma_{ex}(\lambda, m) = \int_0^\infty \pi r^2 Q_{ex}(\lambda, m, r) n(r) dr \tag{3.1}$$

Q_{ex} is the extinction efficiency, for a single particle characterized by its radius r and complex refractive index m, at wavelength λ. $n(r)$ describes the number size distribution, i.e. the number concentration of particles for each radius r.

The aerosol optical depth is defined as the column integrated aerosol extinction coefficient, i.e. integrated over the whole atmospheric column with height h, and is dimensionless.

$$\tau(\lambda, m) = \int_0^h \sigma_{ex}(\lambda, m, z) dz \tag{3.2}$$

The ratio of scattering to extinction is called the single scattering albedo, $\omega_0(\lambda, m)$, and is a measure for the amount of absorption relative to the total extinction. The value of the single scattering albedo is 1 when the extinction is solely due to scattering and 0 if the extinction is due to absorption only.

$$\omega_0(\lambda, m) = \frac{\sigma_{sc}(\lambda, m)}{\sigma_{ex}(\lambda, m)} \tag{3.3}$$

σ_{sc} is the scattering coefficient.

The aerosol index, *ai*, is a concept based on TOMS observations in the near UV, [Torres et al., 1998]. The aerosol index, as defined in Eq. 3.4 below, is the

residue between the measured radiance and the calculated one using the Lambert Equivalent Reflectivity (LER) assumption. Assuming a Rayleigh scattering atmosphere above a Lambertian surface, the Lambert Equivalent Reflectivity [Herman and Celarier, 1997] is defined as the value of the Lambertian spectral surface albedo for which the modelled and measured TOA reflectance are equal. The LER in the multi-wavelength algorithm was determined using the radiative transfer code DAK (Doubling-Adding KNMI, de Haan et al. [1987], Stammes [2000]) .

$$ai = -100 \log \left\{ \left[\frac{I_{\lambda_1}}{I_{\lambda_2}} \right]_{meas} \right\} + 100 log \left\{ \left[\frac{I_{\lambda_1}\left(A_{LER_{\lambda_1}}\right)}{I_{\lambda_2}\left(A_{LER_{\lambda_2}}\right)} \right]_{calc} \right\} \tag{3.4}$$

A_{LER} is the wavelength dependent surface Lambert Equivalent albedo. The UV aerosol index at 388 nm is calculated using the following wavelengths λ_1= 342.5 nm and λ_2= 388 nm. The visible aerosol index at 483.5 nm is calculated using the following wavelengths λ_1= 388 nm and λ_2= 483.5 nm. The aerosol indices represent the change in the spectral contrast with respect to a molecular atmosphere due to the presence of cloud and/or aerosol particles [Torres et al., 2002b]. The aerosol index is sensitive to elevated absorbing aerosol layers such as Saharan dust and biomass burning aerosols, de Graaf et al. [2005].

3.3 The multi-wavelength algorithm

In the wavelength range observed by OMI and for cloud-free skies, the TOA radiance is dominated by atmospheric effects, i.e. molecular and aerosol scattering and absorption. Molecular scattering is referred to as Rayleigh scattering which varies with the wavelength λ as λ^{-4}. For the OMI wavelengths Rayleigh scattering contributes significantly to the total TOA radiance. To account for

this effect the radiative transfer model DAK (de Haan et al. [1987] Stammes [2000]) that includes aerosols and multiple scattering, is applied.

The multi-wavelength algorithm comprises two models: an inversion model (Section 3.3.1) where the actual retrieval is done and a forward model (Section 3.3.2) where all *a priori* data needed to retrieve the optical properties are defined and/or computed using DAK. A variety of aerosol models, characterized by their chemical and physical properties, are introduced into DAK. The aerosol particles are assumed to be spherical so the aerosol extinction is calculated using Mie theory [Mie, 1908]. The retrieval of aerosol information from satellite data is done in various steps. The first step is to determine whether a pixel is cloud free. Next the contribution of the surface to the TOA reflectance needs to be determined. Then the atmospheric contributions to the TOA reflectance need to be separated for gases and aerosols. The aerosol optical depth is retrieved using an optimal estimation retrieval scheme for a number of aerosol models. Then the best fitting aerosol model is selected and used to determine the aerosol optical depth. For a more detailed explanation of the basic components of the algorithm the reader is referred to the OMI ATBD [Torres et al., 2002b]. The extensions to better account for surface effects, different types of aerosols and clouds are explained below in Sections 3.3.2 and 3.3.3.

3.3.1 Inversion Model

The core of the OMI aerosol algorithm is the derivation of aerosol optical properties for cloud free pixels, which is accomplished by comparing the measured TOA reflectance to results from a radiative transfer model stored in look up tables (LUT). This is done for selected aerosol models for which the difference

between the measured and computed TOA reflectances at a number of wavelengths is minimized using least squares minimization. The model with the smallest residue is selected as representative for the pixel. Subsequently this information is used to determine the aerosol optical depth of that ground pixel. The selection of the aerosol models used in this procedure is based on maps providing the monthly averaged geographical distribution of the occurrence of certain aerosol types (cf. Section 3.3.2).

3.3.2 Forward Model

In the absence of clouds, the TOA reflectance measured by satellite sensors arises from atmospheric scattering (molecules and aerosol particles) and surface reflectance. The determination of aerosol optical properties from the measured TOA reflectance is an ill posed problem because there is insufficient information to constrain for possible solutions. Therefore, radiative transfer calculations using DAK are performed to derive the Rayleigh and surface contribution, and *a priori* assumptions are made on the aerosol. Radiative transfer calculations are time consuming, it is therefore convenient and common practice to use precalculated sets of radiative parameters in the algorithm (e.g. Veefkind et al. [1998], von Hoyningen-Huene et al. [2003], Levy et al. [2007b]).

Geographical aerosol distribution

To account for the aerosol spatial and temporal variability, a climatology has been prepared in which the aerosols are classified into different types according to their optical properties. Three generic classes are distinguished: weakly-absorbing, carbonaceous and mineral aerosols. Sea salt, sulfate and nitrate

are three major components of the weakly-absorbing class. Sea salt is entirely natural whereas nitrate and sulfate can be of both natural and anthropogenic origin. Carbonaceous aerosols are generated by biomass burning and fossil fuel combustion. Their chemical composition is a mixture of both absorbing and non-absorbing compounds. The UV-absorbing feature of carbonaceous aerosols is mainly driven by the fraction of black carbon. Mineral aerosols are mechanically generated over the deserts. The presence of iron oxides in mineral dust is responsible for the absorption of UV- radiation. The aerosol temporal and geographical distribution database used in the multi-wavelength algorithm has been developed with a 3D chemical transport zoom model (TM5). The prescribed data-set for the emissions of the primary aerosols in TM5 is presented in Dentener et al. [2006] and the model results used in this study were retrieved within the framework of the AeroCom (Aerosol Comparison between Observation and Models) project [Kinne et al., 2006].

This database has been developed on a grid of $1^\circ \times 1^\circ$. The weakly-absorbing aerosols are assumed to be always present; the two other classes are indicated to be present when the ratio of their mass to the total mass is higher than a threshold, here set at 0.4. Figure 3.1 shows the resulting geographical distribution of the three aerosol types, used in the OMI multi-wavelength algorithm, for the months of May, June and July. Carbonaceous aerosols mainly occur around heavily industrialized areas and over the tropical rain forests, where they are mainly known as biomass burning. Mineral aerosols are mainly located over the northern hemisphere, the Sahara desert, the Middle East and the Gobi desert, and are often referred to as desert dust. Saharan dust is also transported to the Tropical North Atlantic Ocean and the Mediterranean Sea.

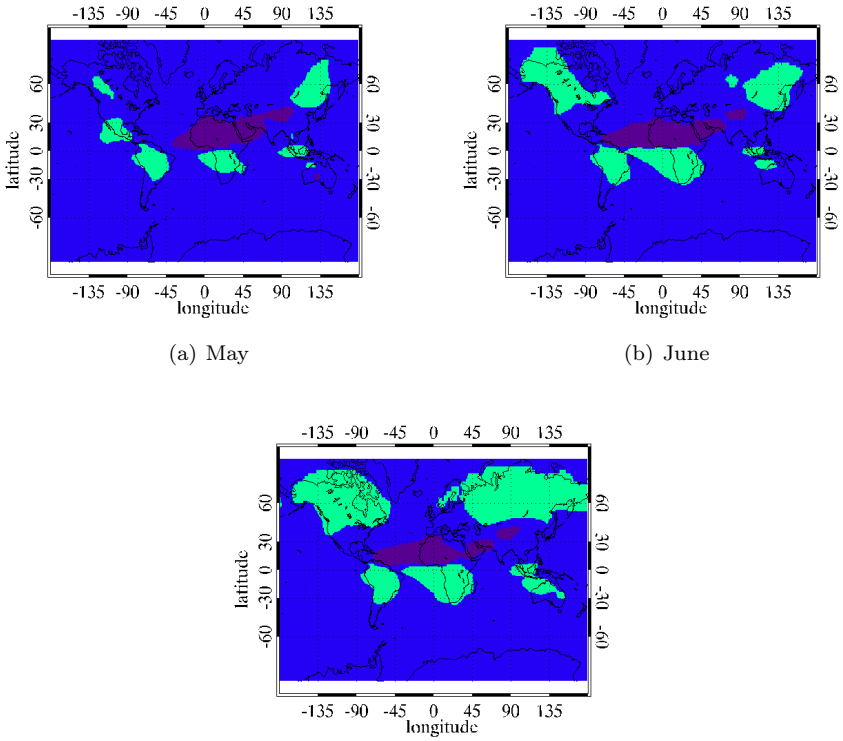

(a) May

(b) June

(c) July

Figure 3.1: Aerosol geographical distribution for May, June and July, determined using the chemical transport model (TM5) as described in the text, providing the climatology used as input in the OMI multi-wavelength algorithm. Blue represents weakly absorbing aerosol, green indicates the occurrence of carbonaceous aerosol and purple shows the occurrence of mineral aerosol.

Aerosol Model

In the part of the solar spectrum observed by OMI, the effects of aerosols on radiative transfer are determined by the size distribution and the complex refractive index of the aerosols (i.e. the chemical composition) and the altitude of

the aerosol layers. The aerosol size distributions and chemistry used to build the aerosol model are derived from AERONET ground-based sun photometer measurements, Dubovik et al. [2002]. AERONET data are used because they are available for a wide range of conditions all over the globe, and were all derived from the same type of instrument: they apply to column integrated properties which are also measured by space borne instruments. In order to build the aerosol models, radiative transfer calculations were performed for some tie points. A tie point represents a node in the database. These tie points are defined by the scene geometry, the surface and the aerosol optical properties. The aerosol size distribution is assumed to be the sum of two lognormal distributions following equation 3.5.

$$n(ln\ r) = \sum_{i=1}^{2} \frac{N_i}{(2\pi)^{\frac{1}{2}}\ ln\ \sigma_i} \exp\left(-\frac{(ln\ r_i - ln\ \overline{r}_{gi})^2}{2\ ln^2\ \sigma_i}\right) \tag{3.5}$$

where N_i is the number concentration, $\overline{r}_{gi}$ is the mean geometric radius and σ_i is the standard deviation of the i^{th} lognormal mode. The different aerosol models were built according to three generic aerosol types defined earlier in Section 3.3.2, weakly absorbing, carbonaceous and mineral. Within an aerosol type the aerosol models differ by either their chemical composition (i.e. refractive index) or their size distribution. Detailed information on the aerosol models, such as geometric mean radii r_g, geometric standard deviation σ_g, complex refractive index and the mode's fraction are presented in Table 3.1.

Table 3.1: Size distributions and refractive indices of OMI aerosol models. The aerosol types (weakly absorbing, WA; carbonaceaous, BB; minerals, DD) provide different aerosol models according to size distribution, refractive index, and vertical distribution. An extra aerosol type is added to account for volcanic ashes (VO). Geometric mean radii, r_g, and geometric standard deviation, σ_g, of modes 1 and 2 of the bimodal size distribution are listed together with the particle number fraction x_2 of the second mode. The imaginary part of the refractive index of desert dust is wavelength-dependent and takes values up to 6.53e-3 (*) or 0.013 (#) in the UV.

Model	$r_{g,1}$	$r_{g,2}$	$\sigma_{g,1}$	$\sigma_{g,2}$	x_2	real	imag
WA_{1101}	0.078	0.497	1.499	2.160	4.36e-4	1.4	5.0e-8
WA_{1102}	0.088	0.509	1.499	2.160	4.04e-4	1.4	5.0e-8
WA_{1103}	0.137	0.567	1.499	2.160	8.10e-4	1.4	5.0e-8
WA_{1104}	0.030	0.240	2.030	2.030	1.53e-2	1.4	5.0e-8
WA_{1201}	0.078	0.497	1.499	2.160	4.36e-4	1.4	0.004
WA_{1202}	0.088	0.509	1.499	2.160	4.04e-4	1.4	0.004
WA_{1203}	0.137	0.567	1.499	2.160	8.10e-4	1.4	0.004
WA_{1301}	0.078	0.497	1.499	2.160	4.36e-4	1.4	0.012
WA_{1302}	0.088	0.509	1.499	2.160	4.04e-4	1.4	0.012
WA_{1303}	0.137	0.567	1.499	2.160	8.10e-4	1.4	0.012
BB_{2101}	0.074	0.511	1.537	2.203	1.70e-4	1.5	0.010
BB_{2102}	0.087	0.567	1.537	2.203	2.06e-4	1.5	0.010

Continued on Next Page...

Model	$r_{g,1}$	$r_{g,2}$	$\sigma_{g,1}$	$\sigma_{g,2}$	x_2	real	imag
BB_{2103}	0.124	0.719	1.537	2.203	2.94e-4	1.5	0.010
BB_{2201}	0.074	0.511	1.537	2.203	1.70e-4	1.5	0.020
BB_{2202}	0.087	0.567	1.537	2.203	2.06e-4	1.5	0.020
BB_{2203}	0.124	0.719	1.537	2.203	2.94e-4	1.5	0.020
BB_{2301}	0.074	0.511	1.537	2.203	1.70e-4	1.5	0.030
BB_{2302}	0.087	0.567	1.537	2.203	2.06e-4	1.5	0.030
BB_{2303}	0.124	0.719	1.537	2.203	2.94e-4	1.5	0.030
DD_{3101}	0.042	0.670	1.697	1.806	4.35e-3	1.53	$\lambda - dep.*$
DD_{3102}	0.052	0.670	1.697	1.806	4.35e-3	1.53	$\lambda - dep.*$
DD_{3201}	0.042	0.670	1.697	1.806	4.35e-3	1.53	$\lambda - dep.\#$
DD_{3202}	0.052	0.670	1.697	1.806	4.35e-3	1.53	$\lambda - dep.\#$
VO_{4101}	0.230	0.230	0.800	0.800	0.5	1.45	7.5e-7

Surface albedo

The retrieval of aerosol optical depth requires precise information on the surface albedo. Uncertainties in the surface albedo lead to errors on the aerosol optical depth retrieval. Veefkind et al. [2000] estimated that in the UV range, an error of 0.01 in the surface albedo would induce an error of 0.1 in the aerosol optical depth retrieved. Torres et al. [1998] explained the impact of the surface albedo on the aerosol optical depth which is different for low and high values. For high surface reflectivities the importance of aerosol absorption increases whereas the effect of scattering decreases significantly with the increase of the aerosol optical thickness. This is due to the enhancement of the ground reflection component

that is backscattered by the aerosol layer toward the surface. For low surface albedo the impact depends on the absorption properties of the aerosol layer. If the aerosol layer is weakly absorbing, scattering dominates resulting in a net increase in the amount of backscattered radiation. If the aerosol layer is highly absorbing, a net decrease of the amount of backscattered radiation is observed. For more information the reader is referred to the OMI ATBD [Torres et al., 2002b]

The multi-wavelength algorithm discriminates between land and sea pixels. The surface contribution to the reflectance at the top of the atmosphere is determined either by an ocean color model or by a surface albedo database for pixels over land.

Currently available surface albedo databases are derived using TOMS [Herman and Celarier, 1997], GOME (Global Ozone Monitoring Experiment, Koelemeijer et al. [2003]), MISR (Multiangle Imaging SpectroRadiometer, [Wanner et al., 1997]) and MODIS data. GOME and TOMS surface albedo databases were derived using measured TOA albedo to derive the Minimum Lambert Equivalent Reflectivity (MLER) of the Earth's surface in the near UV and visible range. An atmospheric correction is applied to account for aerosols and molecules. However, due to the large pixels size, the surface albedo databases from GOME and TOMS are affected by some cloud and aerosols contamination. MODIS [Vermote and Vermeulen, 1999] surface albedo is available at 470 nm and allows for aerosol correction and due to a very high spatial resolution (500 m) cloud contamination is unlikely to happen.

In order to determine which surface albedo database is suitable for use with OMI, the spectral dependence of surface albedo has been determined using data from the DANDELIONS (Dutch Aerosol and Nitrogen Dioxide Experiments

for vaLIdation of OMI and SCIAMACHY, [Brinksma et al., 2005]) campaign in Cabauw, The Netherlands. The TOA reflectances measured by OMI over Cabauw have been simulated for different surface reflectivities by means of radiative transfer calculations. Measured aerosol size distributions were used in these calculations and the optical properties were calculated using a MIE code assuming a complex refractive index of 1.4+0.01 i that is representative of an European urban area [Dubovik et al., 2002]. By comparing the computed reflectance with the one measured with OMI, the surface albedo and its wavelength dependence were derived using linear interpolation. Figure 3.2 shows data for both a clean day (19 June, 2005) with an aerosol optical depth of 0.097$\pm$ 0.004 at 440 nm during the OMI overpass and a polluted day (June 23, 2005) with an aerosol optical depth of 0.41$\pm$ 0.01. Figure 3.2 shows the derived surface albedo for those two days in June 2004. The results for both days are very close. The surface albedo is indeed low in this wavelength domain, but we also observe a definite wavelength dependence with an increase of 30% between 400 and 470 nm.

For the application of the multi-wavelength algorithm at a global scale we developed a monthly mean surface albedo database using MISR data. In the MISR retrieval scheme the aerosol and surface properties are derived simultaneously. Furthermore, it is our experience that merging data sets with different spectral ranges, one in the visible and one in the UV for example, usually leads to discontinuities in the spectral surface albedo,which induce large errors in aerosol retrieval algorithms. The monthly mean surface albedo database derived for the continents is based on MISR Component Global Land Surface Product Version F02 and F04, using five years worth of data Level 3 daily meshed product. The monthly minimum value of each meshed box was determined for the MISR bands

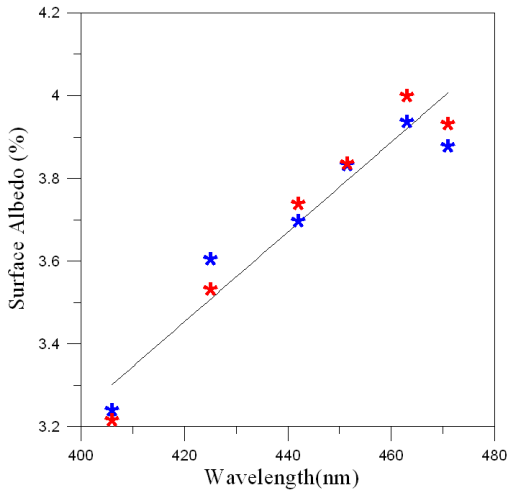

Figure 3.2: Surface albedo at the Cabauw site derived from the OMI signal for June 19^{th} (blue) and 23^{rd} (red) as described in the text

at 446, 558 and 672 nm. From the surface albedo database derived from GOME data [Koelemeijer et al., 2003], it was concluded that a linear extrapolation of the 443 and 670 nm bands toward shorter wavelengths provide a reasonable estimation of the surface albedo in the UV range, over most surfaces. A minimum value of 1% for the surface albedo has been set for the extrapolation. For a small amount of meshed boxes no data were available and a cosmetic fill was applied. Theses boxes were filled using the nearest neighbour filling over a distance of at most one box. Finally, all remaining empty boxes were filled using the GOME surface albedo database.

The spectral dependence of surface albedo derived for Cabauw, Figure 3.2, compares well with the surface albedo database derived from MISR. The surface albedo database derived from MISR compares favorably with TOMS and MODIS over vegetated surfaces whereas over dry surfaces, i.e. desert, the values

tend to be lower for the MISR database.

3.3.3 Cloud screening

When clouds are present they dominate the TOA reflectance. Criteria applied to discriminate between cloud-free pixels and clouded pixels strongly depend on the cloud screening purpose. The transition between aerosol and cloud is often gradual, so any cloud screening protocol leads to a dilemma. Either too many pixels are rejected and a considerable amount of data is lost, or a known bias is accepted due to cloud contamination. In case of the multi-wavelength algorithm three tests are performed, as described below, to determine whether a given pixel is cloud contaminated.

Reflectance threshold combined with aerosol absorption

The first test is based on the UV aerosol index and the value of the reflectance at 388 nm. The presence of cloud results in near-zero values for the UV aerosol index [Hsu et al., 1996]. When the UV aerosol index is near or below zero and the measured reflectance at 388 nm exceeds a fixed threshold, the pixel will be flagged as cloud contaminated and rejected from further analysis. For this study the threshold for the reflectance was set at 0.3 and for the UV aerosol index at 0.12.

Cloud fraction test

All pixels with effective cloud fraction larger than a pre-set threshold value are rejected. To determine this threshold, we take advantage of the A-train

formation by synergistic use of MODIS (Moderate Resolution Imaging Spectroradiometer) on the Aqua satellite and the OMI instrument on Aura. OMI passes over the same area as MODIS within 15 minutes.

MODIS provides a cloud mask grid [Ackerman et al., 2002]. Clouds are generally characterized by higher reflectance and lower temperature than the underlying earth surface. MODIS cloud detection takes place in the visible and infra-red range. Each test fails or succeeds depending on whether the pixel passes a given threshold. Each threshold is determined by the ground surface, the relative humidity, the aerosol load and the viewing angle.

OMI is only sensitive in the UV-visible range. An effective cloud fraction [Acarreta and de Haan, 2002] is retrieved from OMI data by comparing the measured reflectances to reflectances which are computed for both a cloud-free pixel and a fully cloudy pixel assuming a surface Lambert equivalent albedo of 0.8. The cloud fraction thresholds defined for the aerosol algorithm were determined by combining the cloud mask derived from MODIS and the cloud fraction from OMI. In order to do so, MODIS data have been meshed within the OMI grid for each matching orbit and compared to the OMI cloud fraction. Ideally, a given scene would be flagged the same way by both OMI and MODIS and yet it is not, as the assumptions are not the same for both algorithms. So as to define the cloud fraction threshold, a high correlation between MODIS and OMI diagnostic, as well as a stricter flagging in the MODIS case, were expected. Following these requirements a cloud fraction threshold of 0.075 has been determined for this study.

Homogeneity Test: small pixel variability threshold

Cloud free areas and thick clouds are more homogeneous than broken cloud fields. So the homogeneity within an OMI pixel can provide information on whether the pixel is cloud contaminated. The standard deviation within an OMI ground pixel is defined by means of the small pixel radiances. Small pixels are ground pixels with the same spatial resolution in the cross-track direction as the standard OMI ground pixel whereas in the in-flight direction they are smaller [van den Oord et al., 2002]. These pixels correspond to one column pixels (i.e. wavelength) of the CCD (Charge Coupled Device) for which no co-addition was done. It allows determining the standard deviation threshold for which an OMI pixel is set as not clear. In this study the radiances' standard deviation threshold has been set at 1×10^{20} photons s^{-1} nm $^{-1}$ cm $^{-2}$ sr^{-1} (which corresponds to about 0.00015% of typical values of the small pixel variance).

Cloud Screening: Example

Figure 3.3(a) is an RGB picture from MODIS where clouds are visible for June 14^{th} 2005. Figure 3.3(b) shows the cloudmask derived from the OMI multi-wavelength algorithm for the same day. The pixels marked as cloudy by all tests are colored in red. Cloudy pixels detected by the coherence spatial test are yellow, and the cloud free pixels are blue. The areas determined as cloudy by the cloud fraction test are colored purple.

Figure 3.4(a) is a composite map which presents a comparison of the cloud-mask derived from MODIS [Ackerman et al., 2002] and the cloudmask derived from OMI. In order to derive this composite map, the OMI cloudmask has been meshed into the MODIS cloudmask grid. The cloud screening protocol from

Table 3.2: Flag description of the combined cloudmask Figure 3.4(a). P stand for probably

MODIS	OMI	COMBINED	Interpretation
0	0	0	clear for OMI and MODIS
1	0	1	P clear for MODIS, clear for OMI
2	0	2	P cloudy for MODIS, clear for OMI
3	0	3	cloudy for MODIS, clear for OMI
0	1	4	clear for MODIS, cloudy for OMI
1	1	5	P clear for MODIS, cloudy for OMI
2	1	6	P cloudy for MODIS, cloudy for OMI
3	1	7	cloudy for OMI and MODIS

OMI has two positions, pixels are either cloudy or clear. In the MODIS cloud screening protocol, pixels can be flagged in four different ways, cloudy, probably cloudy, probably clear or clear. Therefore, each pixel information from OMI and MODIS have been combined into an unsigned integer, such as the two first bits code for MODIS cloudmask and the third one for the OMI cloudmask. Table 3.2 summarizes and gives interpretations for each observed value in the combined cloudmask Figure 3.4(a). Figure 3.4(b) is a histogram of the available pixels for this comparison. It can be seen that, 66. % of the pixels has been flagged the same way by MODIS and OMI. Both cloudmasks were in complete disagreement for 20. % of the pixels. This occurs mainly over cloud edges, in this case 81% of the pixels were set as cloudy by OMI whereas MODIS set them as clear, therefore, this disagreement can mainly be explained by the size of an OMI pixel. For 13. % of the pixels the comparison is not conclusive as the pixels were flagged as probably clear or uncertain by MODIS.

(b) OMI cloud mask

(a) MODIS RGB

Figure 3.3: The upper panel is a RGB picture derived from channels 1, 3 and 4 of MODIS for June 14^{th} 2005. The lower panel represents the OMI cloudmask i.e. a composite map of the cloud mask derived by the multi-wavelength algorithm for June 14^{th} 2005. Pixels determined cloudy by all tests are red. Pixels determined cloudy by the cloud fraction threshold only are purple. Pixels which did not pass the homogeneity test are yellow. Clear pixels are blue.

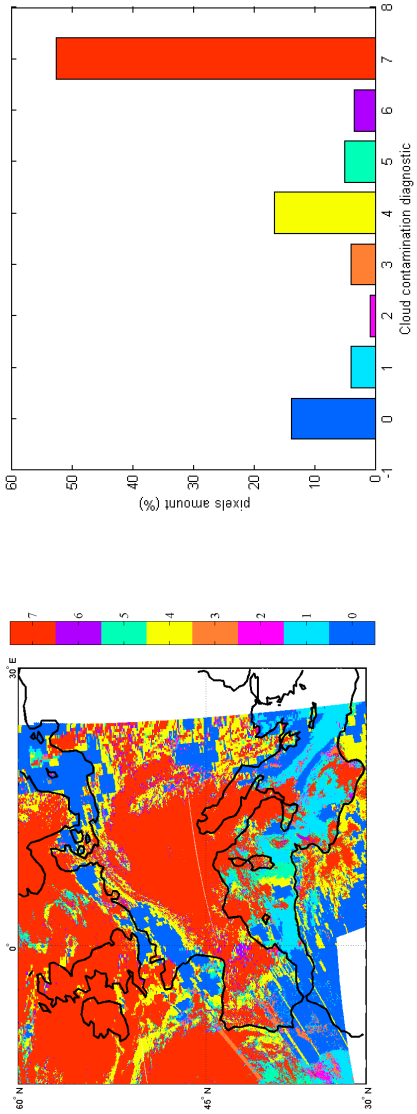

(a) (b)

Figure 3.4: Comparison of the OMI and MODIS cloud screening for June 14^{th} 2005. Dark blue and red represent pixels when MODIS and OMI diagnostics agree. Orange and yellow are representatives for pixels when OMI and MODIS disagree. The upper panel is a composite map of the combined cloudmask. The lower panel is an histogram of the number of pixels versus the cloudmask flag.

3.4 Results and validation for Western Europe

In this section the derived aerosol optical depth from OMI measurements by means of the multi-wavelength algorithm is validated. The validation is done in three steps, in Section 3.4.1 the aerosol optical depth retrieved from OMI is compared to ground measurement data. Section 3.4.2 presents a comparison between OMI retrieval and another spaceborne instrument, MODIS. Finally, monthly averaged composite maps of the aerosol optical depth are analyzed in Section 3.4.3

3.4.1 Comparison between OMI and ground measurements

In order to check the accuracy of the OMI multi-wavelength algorithm, the aerosol optical depth retrieved was compared with collocated Sun photometer data that are available from AERONET (http://aeronet.gsfc.nasa.gov/). The OMI derived aerosol optical depth at 442 nm was compared to the AERONET aerosol optical depth at 440 nm. The sites used for the validation were selected throughout Europe for their representativeness for different types of surfaces and aerosols, see Figure 3.5. OMI derived aerosol optical depths were averaged over an area of 50 km radius to provide a mean value for the ground site. The AERONET data (level 2, version 2) were used as available on the AERONET home page and the averaged of the aerosol optical depth measured between 11 UTC and 14 UTC at 440 nm was computed for comparison.

Figures 3.6 to 3.11 show the comparison between the OMI and AERONET retrieved aerosol optical depths, for the sites considered. Table 3.3 presents the correlation coefficient, R, between OMI and AERONET data. In general the agreement is within the standard deviation of the OMI area average, for both

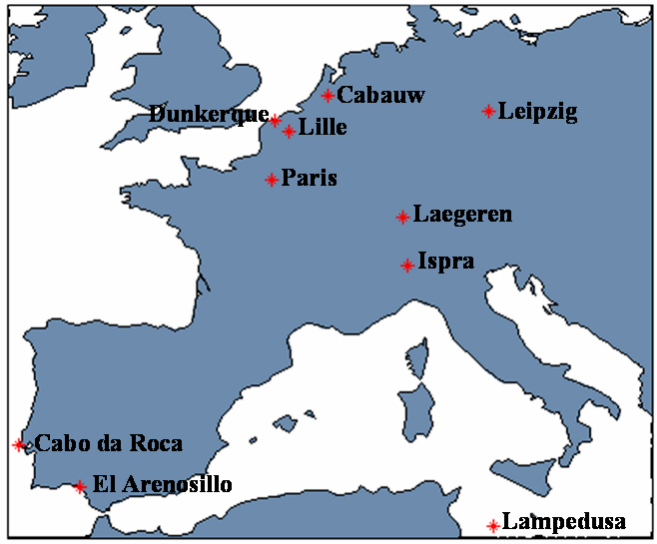

Figure 3.5: Map of location of the AERONET site used in this study

small and large aerosol optical depth values and for all sites considered except for El Arenosillo and Cabo da Roca. We also see some outliers which are discussed below. For every single ground site the OMI results trace the AERONET data. It appears that averaging the aerosol optical depth values over 50 km around a site may not be representative for highly polluted areas such as Ispra and Paris where there are significant gradients in the spatial distribution of the aerosol optical depth. However, spatial averaging is necessary to reduce pixel to pixel variability and provide a statistical significant result. In the comparisons for Cabauw and Dunkerque there are some outliers (marked by arrows), where the retrieved values are much higher than the AERONET aerosol optical depth. Likely, cloud screening in these cases was not strict enough.

Table 3.3: Direct comparison of OMAERO data and AERONET measurements. The Table shows the correlation coefficient, R, and probability, P, of getting a correlation as large as the observe value by random chance, when the true correlation is zero. When P is small the correlation, R, is significant. ndata is the amount of available data and cut-off represents the percentage of discarded data at each end of the dataset, to compute P and R.

Station	R	P	ndata	cut-off
Cabauw	0.0168	0.9608	15	10
Cabo da Roca	0.2897	0.2593	23	10
Dunkerque	0.4508	0.1413	16	10
El Arenosillo	0.6237	1.7×10^{-5}	52	10
Leipzig	0.4512	0.4457	7	10
Ispra	0.4191	0.0370	33	10
Laegeren	0.4952	0.2121	10	10
Lampedusa	0.1311	0.4746	40	10
Lille	0.6400	0.0463	14	10
Paris	0.6050	0.0219	18	10

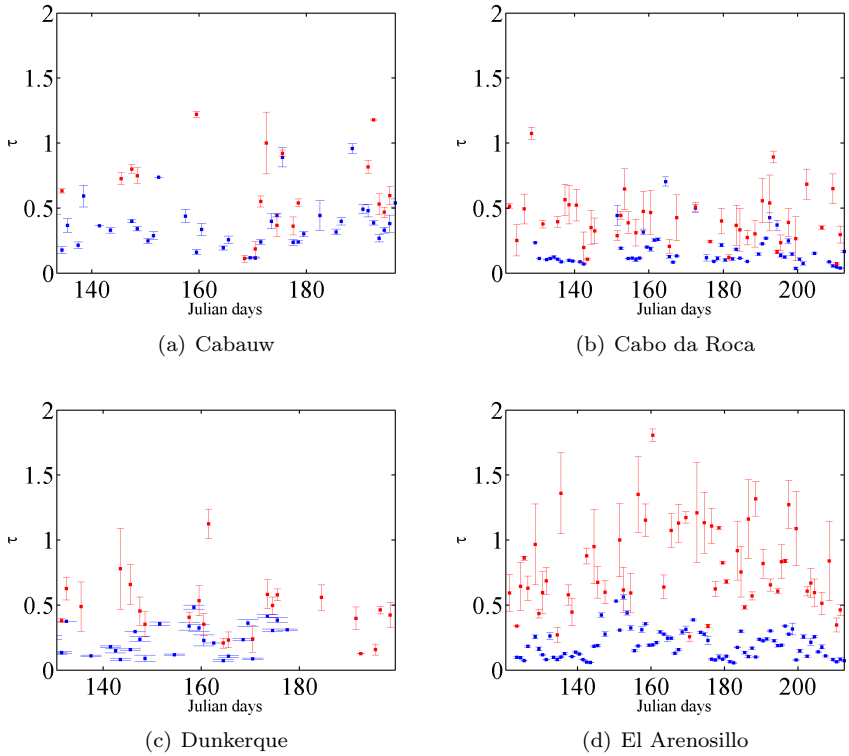

(a) Cabauw (b) Cabo da Roca

(c) Dunkerque (d) El Arenosillo

Figure 3.6: Time series of the aerosol optical depth for May to July 2005 for several AERONET sites in Western Europe. The red squares represent the spatially averaged aerosol optical depth retrieved at 442 nm from the multi-wavelength algorithm within a 50 km radius of the ground site and the errorbars denote its standard deviation. The blue squares represent the averaged aerosol optical depth measured between 11 UTC and 14 UTC at 440 nm with a sun photometer.

Besides cloud contamination, one of the main sources of discrepancy between satellite retrieved and measured aerosol optical depth is the effect of the

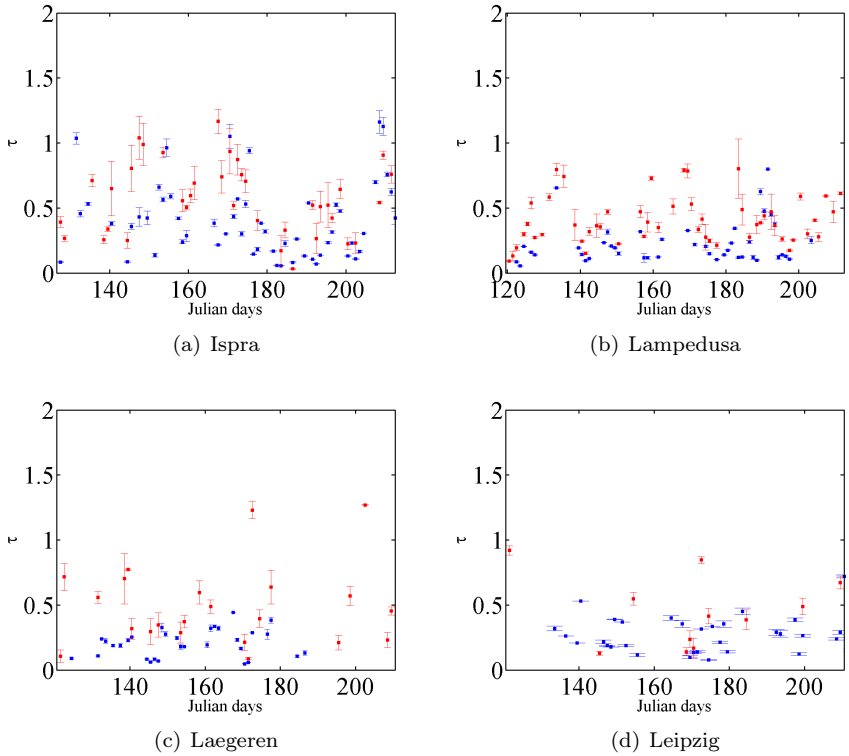

Figure 3.7: Timeseries at 442 nm continued

surface albedo. The El Arenosillo and Cabo da Roca sites are perfect examples of the consequences of a wrong estimation of the surface albedo. Similar patterns in the retrieved and measured aerosol optical depth values, but with a positive bias, indicate that one of our *a priori* assumptions could be wrong. Likely this is due to an underestimation of the surface contribution to the TOA reflectance over land. Figure 3.12 presents a histogram of the difference between the AERONET aerosol optical depth and the OMI aerosol optical depth

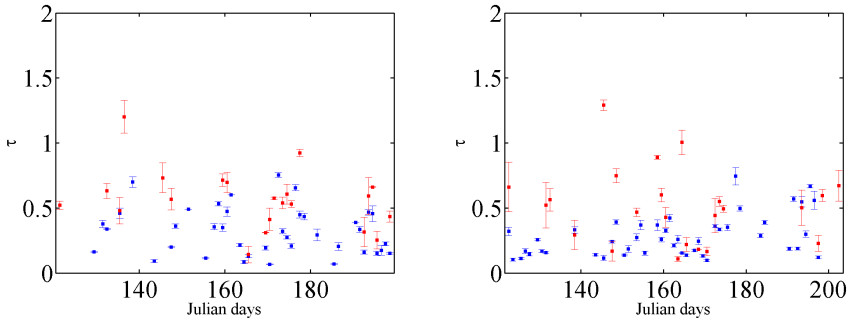

(a) Lille (b) Paris

Figure 3.8: Timeseries at 442 nm continued

respectively for El Arenosillo and Cabo da Roca. The pixels above water are colored in blue and the pixels over land are colored in red. As expected the differences are larger over land than over sea. This is very clearly observed in the data for Cabo da Roca. For El Arenosillo the differences are less obvious. This is explained mainly by the geolocation of the measurement sites and the size of the OMI pixels. It is possible that some pixels flagged as sea include both land and sea resulting in erroneous correction for the surface contribution. Figure 3.13 presents the same data as for Figure 3.12(a) but for the processing it was assumed that the measurement site was displaced 0.5° toward the sea, which results in better discrimination between sea and land pixels with a move of the sea pixels histogram to small values of the difference.

The comparison between the AERONET sun-photometer data and the OMI derived data for a variety of sites indicates that the aerosol optical depth trends are well reproduced by the multi-wavelength algorithm but with a positive bias, albeit this derived surface albedo is not reliable in coastal areas such as

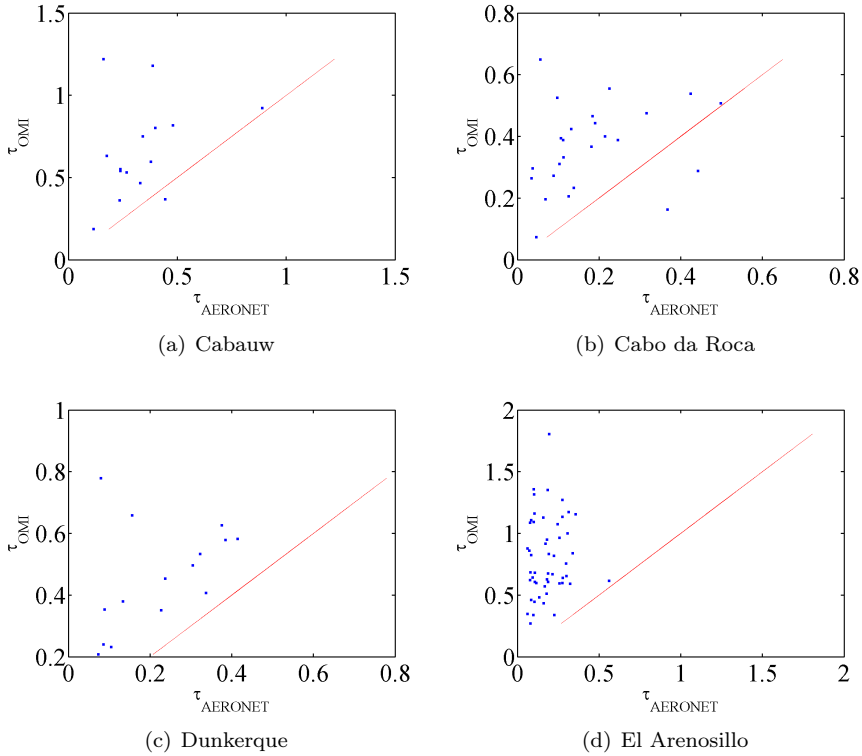

(a) Cabauw (b) Cabo da Roca

(c) Dunkerque (d) El Arenosillo

Figure 3.9: Scatter plot of the aerosol optical depth for May to July 2005 for several AERONET sites in Western Europe.

El Arenosillo and Cabo da Roca. Ongoing work to derive surface albedos from OMI itself is expected to be finalized in the fall of 2007.

3.4.2 Comparison between OMI and MODIS

MODIS and OMI are on different satellites in the A-train. The MODIS instrument is dedicated to, among others, monitoring aerosol and it is often used as a

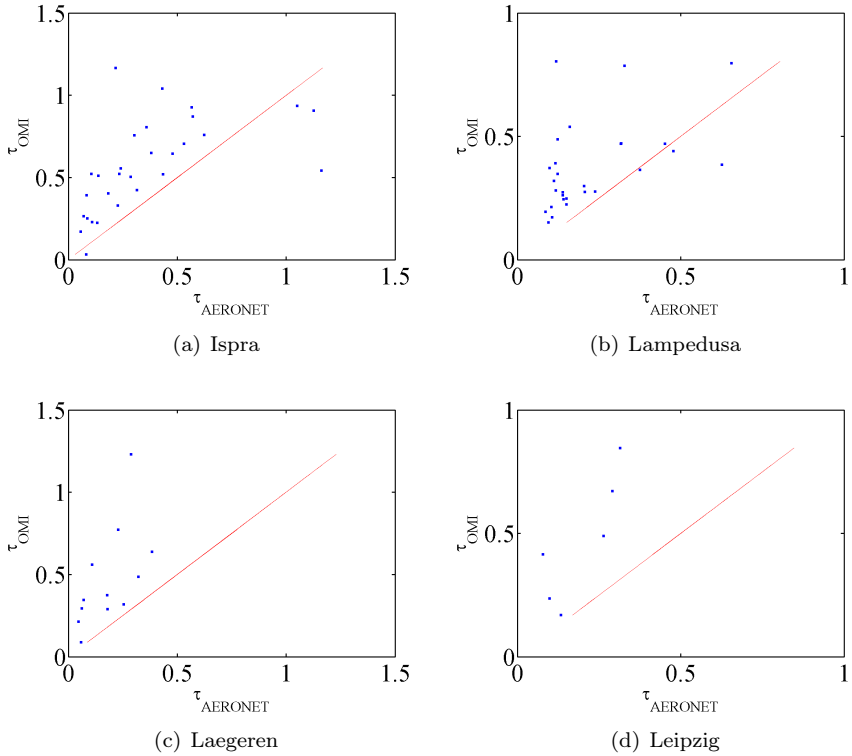

(a) Ispra (b) Lampedusa

(c) Laegeren (d) Leipzig

Figure 3.10: Scatterplot continued

reference for comparison with other data. Because MODIS and OMI view the same area within 15 minutes, the aerosol optical depth distribution should be very similar. Therefore we evaluate the results derived from OMI at 471 nm versus the MODIS aerosol optical depth at 470 nm. MODIS aerosol data (collection 4) have been meshed into the OMI grid for Europe. The observed area is located between latitudes 60°N and 35°N and longitudes 25°E and 15°W. For this study 178081 cloud free pixels were available. The comparison has been

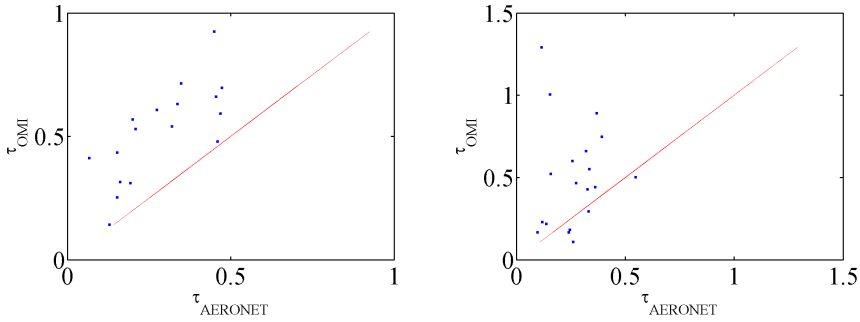

(a) Lil le (b) Paris

Figure 3.11: Scatterplot continued

done for 161528 pixels of the total available. Indeed, only the pixels entirely composed of MODIS pixels of a same surface type were selected. Table 3.4 gives an overview of available pixels.

The results for land and sea pixels are presented separately because both the multi-wavelength algorithm and the MODIS algorithm apply different methods to account for the surface reflection. Over water surfaces an ocean color model accounting for a wind speed-dependent surface roughness [Cox and Munk, 1954] is used. Over land surfaces the multi-wavelength algorithm uses a surface albedo database and the MODIS land algorithm derives the surface contribution to the TOA reflectance from measurement at 2130 nm [Remer et al., 2005] . Figures 3.14 to 3.16 present scatter density plots of the aerosol optical depth derived from OMI versus the aerosol optical depth derived from MODIS for May to July 2005. There is a clear correlation between both datasets, but also a systematic bias that indicates a tendency for OMI to overestimate the aerosol optical depth value with respect to MODIS. The correlation coefficient indicates

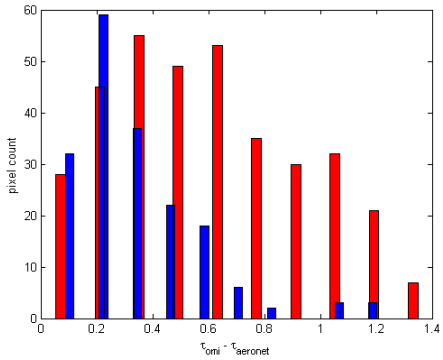

(a) El Arenosillo

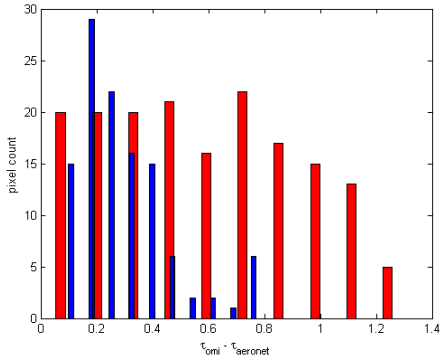

(b) Cabo da Roca

Figure 3.12: Histogram of the differences between the aerosol optical depth derived from OMI data and the aerosol optical depth measured for El Arenosillo (37.1°N 6.7°W) and for Cabo da Roca (38.77°N 9.5°W). Blue represents the pixels over the ocean and the pixels over land are shown in red

that the multi-wavelength algorithm performs better over sea than over land. This illustrates the limitation of the surface database used in this study. The lower correlation over land is also explained by the fact that MODIS over land

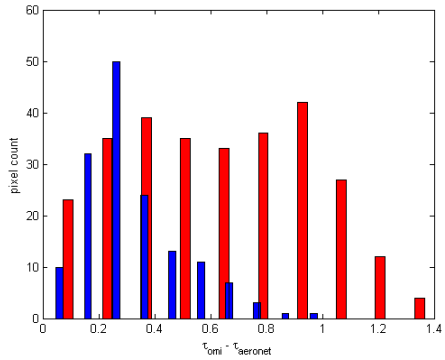

Figure 3.13: Same as figure 3.12(a) assuming that the new location of the El Arenosillo ground site is 37.1°N 7.2°W.

Table 3.4: Amount of pixels used for the OMI vs. MODIS comparison

Month	total	sea pixels	land pixels
May	47356	16265	26875
June	64724	17724	40845
July	66001	21034	38785

is less reliable than over sea (Remer et al. [2002] and Chu et al. [2002]). It is noted that after completion of this study, collection 5 data has become available with global aerosol optical depth values significantly lower than for collection 4.

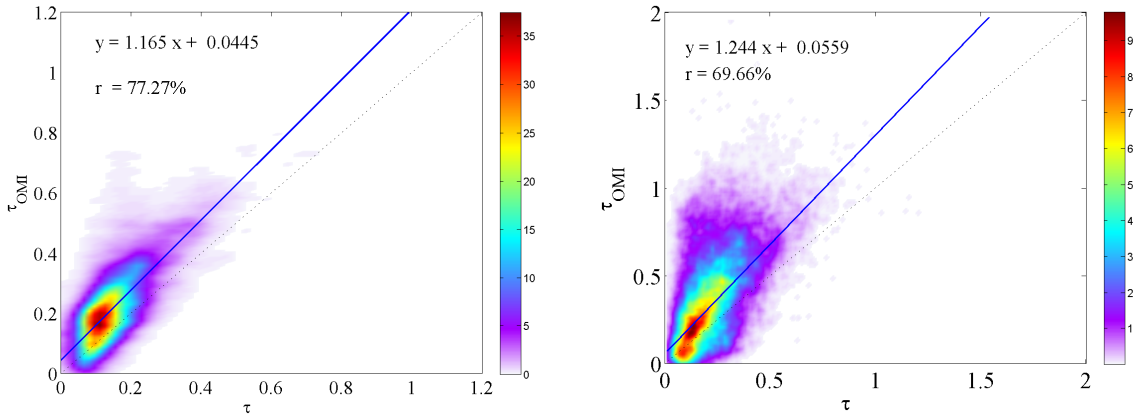

(a) Sea pixels

(b) Land pixels

Figure 3.14: Scatter density plot of the aerosol optical depth at 471 nm derived from OMI data as a function of the aerosol optical depth at 470 nm derived from MODIS data over Western Europe for May 2005. The upper panel represents sea pixels and the lower panel shows land pixels.

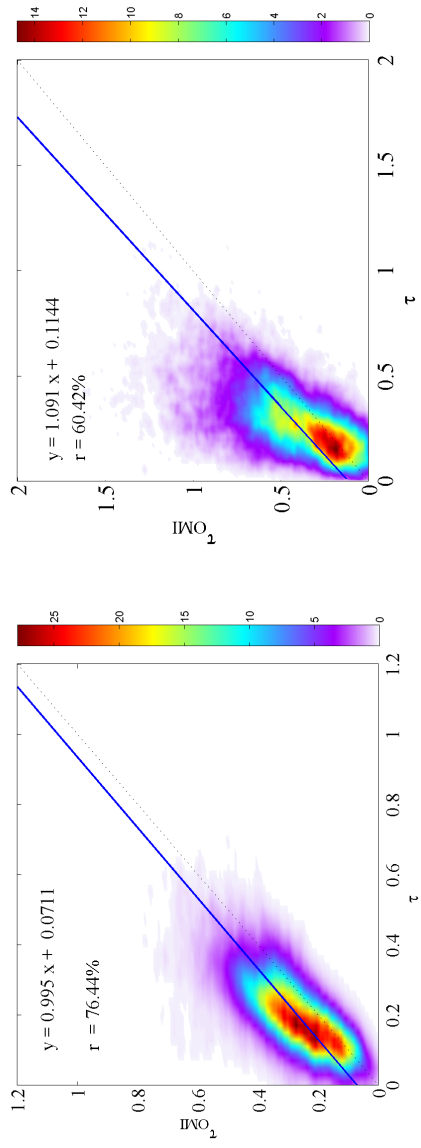

(a) Sea pixels

(b) Land pixels

Figure 3.15: Same as Figure 3.14 for June 2005.

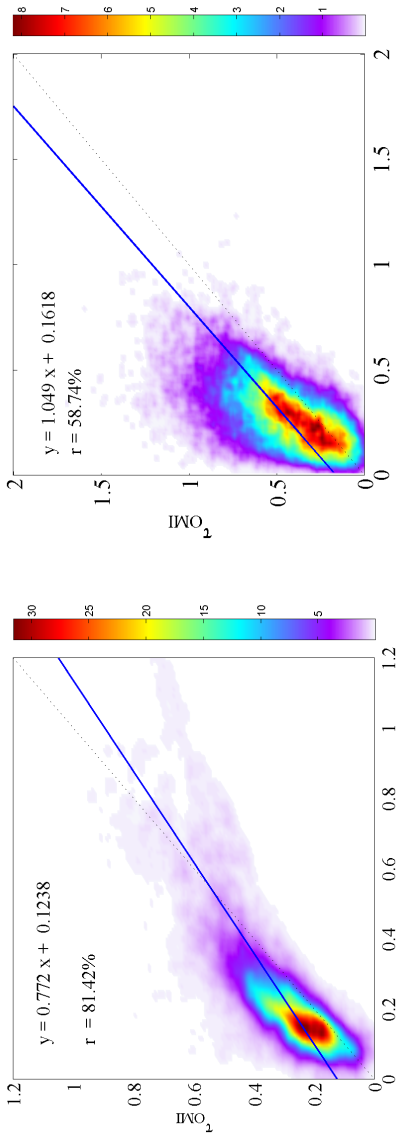

(a) Sea pixels

(b) Land pixels

Figure 3.16: Same as Figure 3.14 for July 2005.

3.4.3 Spatial variation of the aerosol optical depth

Figure 3.17 shows a composite map of the monthly aerosol optical depth at 442 nm over Europe for May to July 2005. The white areas indicate the occurrence of either cloud or high surface albedo. They present a large variation in the aerosol optical depth over Europe. The high aerosol optical depth values are associated with highly industrialized areas whereas low values are observed at remote places. Aerosol optical depth values as high as 1 are observed in some areas over Germany, Belgium, The Netherlands and Northern Italy whereas aerosol optical depth values of 0.2 to 0.4 were observed over Denmark and Ireland.

Northern Italy presents a situation with a strong spatial gradient due to the presence of the Alps which provides a natural barrier for transport of aerosol produced in the heavily industrialized areas in the Po Valley (Milano, Torino). Hence these aerosols can only be ventilated through the Po Valley to the Adriatic Sea.

The Iberian peninsula which contains the only European desert, presents an unrealistic pattern. Indeed, a severe drop of the aerosol optical depth is observed across the coast, which denotes clearly that the surface reflectance contribution over land is underestimated. This behavior is also observed for the timeseries of El Arenosillo and Cabo da Roca.

In June, the average aerosol optical depth values are lower across Europe, but the heavily industrialized areas are still noticeable. To better understand these values the aerosol optical depth composite map has been compared to the NO_2 composite map, Figure 3.18, derived from the NRT OMI algorithm [Boersma et al., 2006]. Aerosols and NO_2 are both produced by anthropogenic

activities so the observation of the NO_2 tropospheric column composite map can help to better understand the aerosol composite map. Due to the short lifetime of NO_2, monitoring the NO_2 concentration allows for the identification of source regions. The variation of the monthly mean concentration in NO_2 does not imply a reduction of the activities. The NO_2 concentration appears to be lower in May than in June, whereas the monthly mean observed for July and June are similar. Comparison of the NO_2 concentration and the aerosol optical depth maps indicates that the low aerosol optical depth values observed in June are in part due to a difference in the meteorological conditions resulting in a difference in the transport. The aerosol optical depth composite map for July presents very high values from Orleans (47.9°N 1.9°E) to Nantes (47.23°N 1.58°W). Unfortunately no groundbased data were available for this area.

Table 3.5 summarizes the monthly mean aerosol optical depth measured or derived for Cabauw, Ispra and Paris. The AERONET mean values were computed using all available aerosol optical depths measured between 11 UTC and 14 UTC. The OMI mean aerosol optical depth used all available values derived within a raduis of 50 km to the ground site. As observed earlier the aerosol optical depth values derived from OMI are higher than their measured counterparts. However, the monthly mean values reproduce qualitatively the aerosol optical depth evolution across Western Europe.

3.5 Conclusion and Perspectives

The aerosol optical depth retrieved by means of the OMI multi-wavelength algorithm has been compared to ground based and satellite data. A major source of uncertainty in the retrieval of aerosol optical properties over land is

Table 3.5: Monthly mean aerosol optical depth derived from AERONET and OMI data. The monthly mean aerosol optical depth computed form all available aerosol optical depth measured between 11 UTC and 14 UTC. The OMI monthly mean aerosol optical depth computed form all available aerosol optical depth derived within a raduis of 50 km to the ground site.

	OMI			AERONET		
location	May	June	July	May	June	July
Cabauw	0.89	0.53	0.75	0.41	0.36	0.45
Ispra	0.78	0.84	0.50	0.38	0.42	0.29
Paris	0.56	0.53	0.55	0.40	0.32	0.40

the surface albedo. The ground-based data from the DANDELIONS campaign allowed us to derive the spectral dependance of the surface albedo which is representative for almost all Europe for this time period. Unfortunately this *a priori* constraint still remains a problem for the Iberian peninsula. This may be solved when a more reliable surface albedo database will be available. A surface albedo database is currently being developed based on OMI observations.

Another major problem in aerosol remote sensing is the inability to retrieve aerosol properties in the presence of clouds. Therefore, accurate cloud detection is crucial. The cloud screening procedure, developed for the OMI multi-wavelength algorithm, is found to be satisfactory as MODIS and OMI cloud mask agree in 76.36 % of the conclusive cases. In the cloud screening procotol the OMI pixel size remains the main drawback for area such as cloud edges or broken cloud fields. Both the sensitivity of the multi-wavelength algorithm for retrieval of aerosols over various terrains and better cloud screening remain to be explored.

Presented results from the OMI multi-wavelength algorithm show that the timeseries for different sites over Europe compare favorably with the AERONET

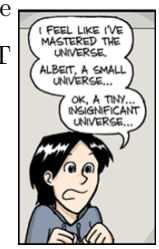

values. The direct ground based observations and the OMI derived aerosol optical depth show similar trends in spite of the size of the OMI pixels. The correlation between OMI and AERONET data is as high as 0.6 for ground sites such as Lille, Paris and El Arenosillo, about 0.4 for Ispra and no significant correlation was found for the other ground sites. The aerosol optical depth derived from the multi-wavelength algorithm also correlates well with the MODIS aerosol optical depth. A correlation coefficient of 0.66 over land and 0.79 over sea was derived for the period from May to July 2005. The correlation is better over dark water surfaces than over bright land surfaces, although the latter is still quite reasonable. However, there is a bias in the OMI vs MODIS comparison with an apparent overestimation of the OMI aerosol optical depth. The situation over land is expected to improve when the OMI based surface albedo database becomes available and can be used in the aerosol optical depth retrieval over land.

The spatial distribution of the aerosol optical depth over Europe for May, June and July 2005 was derived from OMI data. The retrievals show strong horizontal aerosol optical depth gradients with high aerosol optical depth values in the vicinity of highly industrialized areas and low values around remote places.

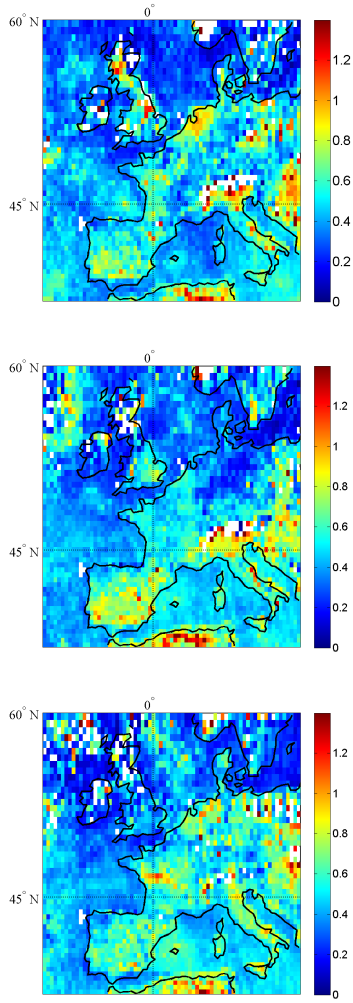

Figure 3.17: Composite map of the aerosol optical depth at 442 nm over Europe for May (upper panel), June (center panel) and July (lower panel) 2005. Aerosol optical depth has been retrieved by applying the multi-wavelength method to OMI satellite data. White areas indicate that no mean values were computed

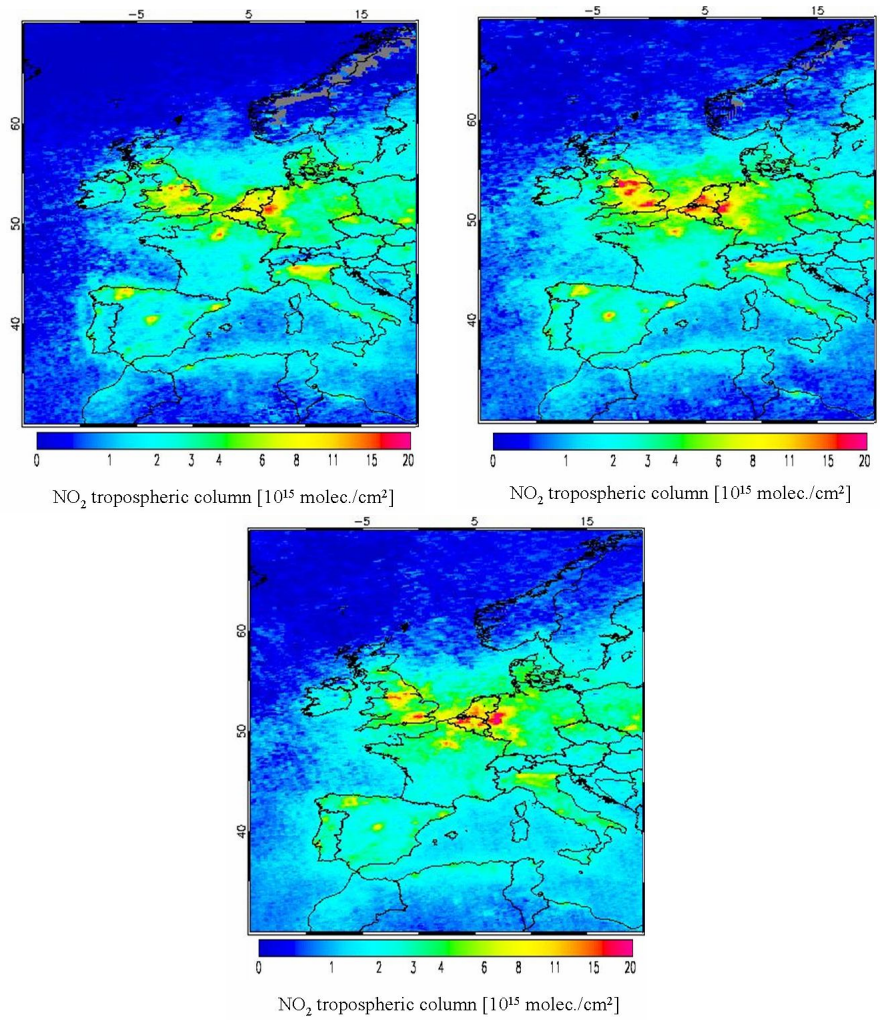

Figure 3.18: Composite map of spatial variation of the nitrogen dioxyde tropospheric column (10^{15} molec.cm^{-2}) over Europe for May (upper panel), June (center panel) and July (lower panel) 2005. Grey areas indicate that no mean values were computed

3.6 Acknowledgement

The work described in this paper is supported by SRON (The Netherlands Space Research Organization) and TNO internal funding. OMI, a Dutch Finnish instrument, is part of NASA's EOS Aura payload. The OMI project is managed by NIVR and KNMI in the Netherlands. The authors thank the different P.I.'s for the AERONET sunphotometer data.

Chapter 4

Aerosol optical depth over the Amazon Basin from OMI

This chapter is in preparation for submission.

Abstract

In this study, the multi-wavelength algorithm is tested for biomass burning generated aerosols and for the aerosol layer height. It occurs that the aerosol optical depths derived by the current implementation of the multi-wavelength algorithm which provide with the OMI Aerosol Product (Torres et al. [2002b]) presents an overestimation with respect to AERONET. The results after the introduction of various constraint on the aerosol models and/or the aerosol height layer were mitigated when solely observing the aerosol optical depth.

4.1 Introduction

The aerosol impact on the Earth's radiative balance is twofold. The aerosol direct radiative effect is due to scattering and/or absorption of the incoming solar radiation. The aerosol indirect radiative effect is the modification of the microphysical properties of clouds and thus their radiative properties and lifetime. The changes in cloud radiative properties are referred as the *cloud albedo effect* and the aerosol effect on the cloud lifetime is referred as *cloud lifetime effect*. The Fourth assessment report of the IPCC [IPCC, 2007] estimates that the combined aerosol direct and cloud albedo effects exert a negative radiative forcing, with a median of -1.3 $W \cdot m^{-2}$ with a 90% confidence range between -2.2 and -0.5 $W \cdot m^{-2}$. Aerosols compensate about 45% of the positive radiative effect induced by long-lived greenhouse gases.

The aerosol direct radiative effect (DRE) is an important component on global to regional scales, because it influences land surface, atmosphere boundary layer processes and global surface temperatures. Until recently, estimates of the aerosol effect on climate were mainly based on model calculations and evaluated against aerosol ground-based measurements. During the last decades, significant progress has been achieved in aerosol remote sensing (satellite, surface network, field campaign), allowing for measurement-based assessment of the aerosol DRE.

Uncertainties in the spatial and vertical distribution and the physical and chemical properties of aerosol particles, as well as the lack of understanding of aerosol-cloud interactions, cause large uncertainties in the current estimate of the DRE. Measurement-based estimates of the clear-sky DRE at TOA are about -5.5$\pm$ 0.2 $W \cdot m^{-2}$ over the global ocean and integration of satellite retrievals and

model simulation provides a DRE of -4.9± 0.7 W·m^{-2} over land [Yu et al., 2006]. However, the uncertainties in the DRE estimates are much larger on regional scales than on global scale, clear-skies aerosol DRE is mainly driven by geographical variations of aerosol optical properties[Hatzianastassiou et al., 2007].

In this study we assess the aerosol optical depth (τ) using the Ozone monitoring instrument (OMI) over the Amazon Basin for the area between latitudes 4°S and 25°S and longitudes 35°W and 72°W. The climate in Central Amazonia is characterized by a wet season, from December to May, and a dry season, from June to November. We analyze the aerosol optical depth for June to December 2006. The analysis of the aerosol DRE is done for the dry season, which is split in two periods, June to August (JJA) and September to November (SON). For the area and the period observed, data are available from two ground-based measurement sites, Alta Floresta (9.92°S 56.02°W) and Cuiabá-Miranda (15.73°S 56.02°W). These ground-based measurement sites are part of the AEROsol Robotic Network (AERONET, Holben et al. [1998]). The site of Alta-Floresta is located in central south of the Amazon basin, the tropical forested region. This site is representative for agricultural and forest biomass burning activities. The site of Cuiabá-Miranda is located in a transition area between the Amazonia, the *Cerrado* and the *Pantanal* and is heavily affected by regional savanna biomass burning.

The daily aerosol optical depth retrieved from OMI measurements, by means of the multi-wavelength algorithm, is used to estimate the spatial distribution of the biomass burning aerosols from June to December 2006. In this section, the ability of the multi-wavelength algorithm to reproduce the aerosol optical depth in the Amazon basin is examined. First, the ability of the multi-wavelength algorithm to differentiate between aerosol generated by forest fire and aerosol

generated by savanna fire is analyzed. Then, the sensitivity to the aerosol layer height is investigated (Section 4.4). A brief overview of the multi-wavelength algorithm is presented Section 4.2. A detailed description of the aerosol models used by the multi-wavelength algorithm in this study is given Section 4.3

4.2 Overview of the multi-wavelength algorithm

The multi-wavelength algorithm is a pixel-by-pixel approach using 14 wavelength bands between 342.5 nm and 483.5 nm which applies only to cloud-free areas. The wavelength have been selected to exclude spectral features in the surface albedo related to surface vegetation and ozone absorption in the UV. The main assumption in the multi-wavelength algorithm is that the TOA up-welling radiance is given by the sum of the atmospheric and surface components. The atmospheric component contains information about the molecular scattering, clouds and aerosols. The surface component is accounted for depending on the surface type. Over ocean the surface contribution to the TOA reflectance is relatively small and an ocean color model based on the Cox and Munk, [Cox and Munk, 1954], parametrization is embedded in the operational algorithm. Over land the surface contribution is provided by means of a monthly mean surface albedo database. The monthly mean surface albedo database used in this study, is derived from MISR (Multiangle Imaging SpectroRadiometer, [Wanner et al., 1997]) data Component Global Land Surface Product Version F02 and F04, using five years worth of data Level 3 daily meshed product. Once the surface contribution is accounted for in the TOA reflectance, the retrieval uses look up tables based on detailed radiative transfer calculations for several models at various aerosol optical depths, solar zenith angles, viewing zenith angles and

relative azimuth angles to determine the aerosol model which best describes the measured reflectance. In the current implementation, 24 models which differ by their size distribution and/or complex refractive index and/or altitude of aerosol layer are used. To account for the aerosol spatial and temporal variability, a database restricts the use of each model according to three generic aerosol types, weakly-absorbing, carbonaceous, mineral.

4.3 Aerosol properties

The net effect of the aerosol on climate is cooling of the surface, but depending on their absorbing properties they either warm or cool the atmosphere. The radiative properties of an aerosol particle are mainly driven by its composition, size and shape. According to Mie theory the aerosol extinction is largest when the aerosol radius is similar to the wavelength of the radiation. Because particle size varies with particle origin, this implies that particles emitted by different sources affect the Earth's radiative balance in different ways. Thus, it can be expected that the longwave aerosol radiative effects will be mainly dominated by large particles whereas fine particles will affect the shortwave aerosol radiative effects.

The aerosol absorption properties depend mainly on the black carbon concentration and on its mixing state (internal versus external) [Dubovik et al., 2002]. The aerosol particles emitted by biomass burning contain high concentrations of black carbon, however, several studies of the single scattering albedo indicate that the light is predominantly scattered.

The biomass burning aerosol particles present over the Amazon basin are

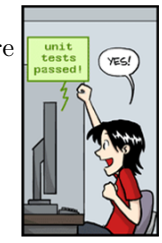

mainly generated by forest fires or savanna fires. Ground-based observations indicate that the size distribution of the aerosol particles produced during biomass burning is well represented by the sum of two lognormal distributions representing a fine and a coarse mode:

$$n(ln\ r) = \sum_{i=1}^{2} \frac{N_i}{(2\pi)^{\frac{1}{2}}\ ln\ \sigma_i} \exp\left(-\frac{(ln\ r_i - ln\ \overline{r}_{gi})^2}{2\ ln^2\ \sigma_i}\right) \tag{4.1}$$

where N_i is the number concentration, $\overline{r}_{gi}$ is the mean geometric radius and σ_i is the standard deviation for the i^{th} mode.

For the present analysis, new sets of aerosol models, representative for aerosol particles originating from forest and savanna fires, have been generated in addition to the nominal biomass burning aerosol models present in the current implementation of the algorithm. The new aerosol models have been defined using size distributions, aerosol optical depth, and single-scattering albedo data derived from AERONET sunphotometer observations at Alta Floresta (9.92°S 56.02°W) and Cuiabá-Miranda(15.73°S 56.02°W) [Schafer et al., 2008]. The observations at Alta Floresta and Cuiabá-Miranda are representative for forest fire and savanna fire cases respectively. The main information from these observations was that the fine aerosol mode is strongly correlated with the aerosol optical depth, as previously pointed out by Reid et al. [1999] and Kaskaoutis et al. [2007]. Therefore in the newly generated set of aerosol models a dependence between the size distribution and the aerosol optical depth has been introduced. This feature is the major difference between the dedicated aerosol models and the nominal ones. The altitude of the aerosol layers is also prescribed differently in the new set of aerosol models. In the nominal aerosol

Model	$r_{g,1}$	$r_{g,2}$	$\sigma_{g,1}$	$\sigma_{g,2}$	x_2	real	imag
BB_{2101}	0.074	0.511	1.537	2.203	1.70e-4	1.5	0.010
BB_{2102}	0.087	0.567	1.537	2.203	2.06e-4	1.5	0.010
BB_{2103}	0.124	0.719	1.537	2.203	2.94e-4	1.5	0.010
BB_{2201}	0.074	0.511	1.537	2.203	1.70e-4	1.5	0.020
BB_{2202}	0.087	0.567	1.537	2.203	2.06e-4	1.5	0.020
BB_{2203}	0.124	0.719	1.537	2.203	2.94e-4	1.5	0.020
BB_{2301}	0.074	0.511	1.537	2.203	1.70e-4	1.5	0.030
BB_{2302}	0.087	0.567	1.537	2.203	2.06e-4	1.5	0.030
BB_{2303}	0.124	0.719	1.537	2.203	2.94e-4	1.5	0.030

Table 4.1: Size distributions and refractive indices of the biomass burning aerosol models used in the current study. Geometric mean radii, r_g, and geometric standard deviation, σ_g, of modes 1 and 2 of the bimodal size distribution are listed together with the particle number fraction x_2 of the second mode.

models the aerosol layer is assumed to be 2 km thick and the base of the layer is set at three different altitudes, i.e. 0, 2 or 4 km. For the dedicated aerosol models a thin aerosol layer at 0, 1, 2, 3, 4 or 5 km is assumed.

Detailed information and radiative transfer results for each aerosol model were stored in dedicated look-up tables labelled BB, BF and BS, respectively, for nominal, forest and savanna aerosol models. Tables 4.1 to 4.3 summarize the size distribution parameters and the refractive indices of each aerosol model used in this study.

4.4 Impact of the aerosol properties

In this section the aerosol optical depth retrieved by means of the multi-wavelength algorithm is presented. First, the algorithm is tested for different aerosol models to evaluate its sensitivity for biomass burning generated aerosols. In

Model	$r_{g,1}$	$r_{g,2}$	$\sigma_{g,1}$	$\sigma_{g,2}$	x_2	real	imag
BS_{2101}	0.009	2.020	2.710	1.598	7.53e-6	1.500	0.036
BS_{2201}	0.009	2.020	2.710	1.598	7.53e-6	1.500	0.024
BS_{2301}	0.009	2.020	2.710	1.598	7.53e-6	1.500	0.015
BS_{2401}	0.009	2.020	2.710	1.598	7.53e-6	1.500	0.007
BS_{2102}	0.081	1.715	1.463	1.671	0.000131	1.500	0.036
BS_{2202}	0.081	1.715	1.463	1.671	0.000131	1.500	0.024
BS_{2302}	0.081	1.715	1.463	1.671	0.000131	1.500	0.015
BS_{2402}	0.081	1.715	1.463	1.671	0.000131	1.500	0.007
BS_{2103}	0.084	1.849	1.491	1.644	0.000103	1.500	0.036
BS_{2203}	0.084	1.849	1.491	1.644	0.000103	1.500	0.024
BS_{2303}	0.084	1.849	1.491	1.644	0.000103	1.500	0.015
BS_{2403}	0.084	1.849	1.491	1.644	0.000103	1.500	0.007
BS_{2104}	0.093	1.560	1.470	1.702	9.78e-5	1.500	0.036
BS_{2204}	0.093	1.560	1.470	1.702	9.78e-5	1.500	0.024
BS_{2304}	0.093	1.560	1.470	1.702	9.78e-5	1.500	0.015
BS_{2404}	0.093	1.560	1.470	1.702	9.78e-5	1.500	0.007
BS_{2105}	0.101	1.046	1.489	1.870	0.00013	1.500	0.036
BS_{2205}	0.101	1.046	1.489	1.870	0.00013	1.500	0.024
BS_{2305}	0.101	1.046	1.489	1.870	0.00013	1.500	0.015
BS_{2405}	0.101	1.046	1.489	1.870	0.00013	1.500	0.007
BS_{2106}	0.103	1.548	1.482	1.689	6.43e-5	1.500	0.036
BS_{2206}	0.103	1.548	1.482	1.689	6.43e-5	1.500	0.024
BS_{2306}	0.103	1.548	1.482	1.689	6.43e-5	1.500	0.015
BS_{2406}	0.103	1.548	1.482	1.689	6.43e-5	1.500	0.007

Table 4.2: Same as Table 4.1 for savanna dedicated aerosol models

Model	$r_{g,1}$	$r_{g,2}$	$\sigma_{g,1}$	$\sigma_{g,2}$	x_2	real	imag
BF_{2101}	0.094	1.419	1.365	1.744	0.00038	1.500	0.003
BF_{2201}	0.094	1.419	1.365	1.744	0.00038	1.500	0.010
BF_{2301}	0.094	1.419	1.365	1.744	0.00038	1.500	0.020
BF_{2102}	0.096	0.376	1.383	2.257	0.00172	1.500	0.003
BF_{2202}	0.096	0.376	1.383	2.257	0.00172	1.500	0.010
BF_{2302}	0.096	0.376	1.383	2.257	0.00172	1.500	0.020
BF_{2103}	0.098	1.226	1.420	1.840	0.000191	1.500	0.003
BF_{2203}	0.098	1.226	1.420	1.840	0.000191	1.500	0.010
BF_{2303}	0.098	1.226	1.420	1.840	0.000191	1.500	0.020
BF_{2104}	0.099	1.058	1.456	1.905	0.000168	1.500	0.003
BF_{2204}	0.099	1.058	1.456	1.905	0.000168	1.500	0.010
BF_{2304}	0.099	1.058	1.456	1.905	0.000168	1.500	0.020
BF_{2105}	0.102	1.354	1.479	1.768	8.65e-5	1.500	0.003
BF_{2205}	0.102	1.354	1.479	1.768	8.65e-5	1.500	0.010
BF_{2305}	0.102	1.354	1.479	1.768	8.65e-5	1.500	0.020
BF_{2106}	0.101	1.229	1.486	1.823	7.37e-5	1.500	0.003
BF_{2206}	0.101	1.229	1.486	1.823	7.37e-5	1.500	0.010
BF_{2306}	0.101	1.229	1.486	1.823	7.37e-5	1.500	0.020
BF_{2107}	0.105	0.936	1.465	1.939	8.98e-5	1.500	0.003
BF_{2207}	0.105	0.936	1.465	1.939	8.98e-5	1.500	0.010
BF_{2307}	0.105	0.936	1.465	1.939	8.98e-5	1.500	0.020

Table 4.3: Same as Table 4.1 for forest dedicated aerosol models

Sections 4.4.1 and 4.4.3, the retrieved aerosol optical depth is compared to other measurement-based aerosol optical depth.

4.4.1 Comparison with ground based measurement

The accuracy of the aerosol optical depth retrieved by the multi-wavelength algorithm is tested by comparison with collocated ground-based sun photometer data, available from the AERONET (http://aeronet.gsfc.nasa.gov/). To this end, the OMI retrieved aerosol optical depths were averaged over an area of 50 km radius to provide a mean value for the ground site. AERONET data (level 2, version 2) were used, as provided on the AERONET home page, and observations between 16.15 UTC and 17.30 UTC i.e. ± 30 minutes to the OMI overpass time, were averaged. The aerosol optical depths at 442 nm are compared to the AERONET aerosol optical depth at 440 nm for Alta Floresta and Cuiabá-Miranda.

The Amazon basin is located in the InterTropical Convergence Zone (ITCZ), a low-pressure zone near the equator, which is associated with considerable cloud formation. Figure 4.1 shows histograms of the averaged effective cloud fraction derived from OMI measurements [Acarreta et al., 2004; Sneep et al., 2008] during the observed period. The study area is between latitudes 4°S and 25°S and longitudes 35°W and 72°W and all available OMI effective cloud fraction data were meshed on a $0.25° \times 0.25°$ grid. On average, 73% of the observed pixels present an effective cloud fraction larger than 20%.

Although cloud free pixels were required, the cloudiness of this area still remains important and therefore the aerosol optical depth retrieved by means of the multi-wavelength algorithm might be affected by the 3-D aerosol-cloud

radiative interactions. In fact, in the clear region near to cloud, 3-D aerosol-cloud radiative interactions have a large impact on the clear region reflectance and thus on the aerosol retrieval. From a study made over the biomass burning area of the Amazon basin, Wen et al. [2007] concluded that the 3-D aerosol-cloud radiative interaction enhances extensively the reflectance in clear regions around broken clouds. On the other hand the aerosol optical depths (level 2, version 2) provided by AERONET are not affected by the 3-D aerosol-cloud radiative interactions. The mean cloud fraction was 15% for the observed period and the 50 km radius area around the ground-based measurement site, therefore an overestimation with respect to AERONET retrieved aerosol optical depth might be observed.

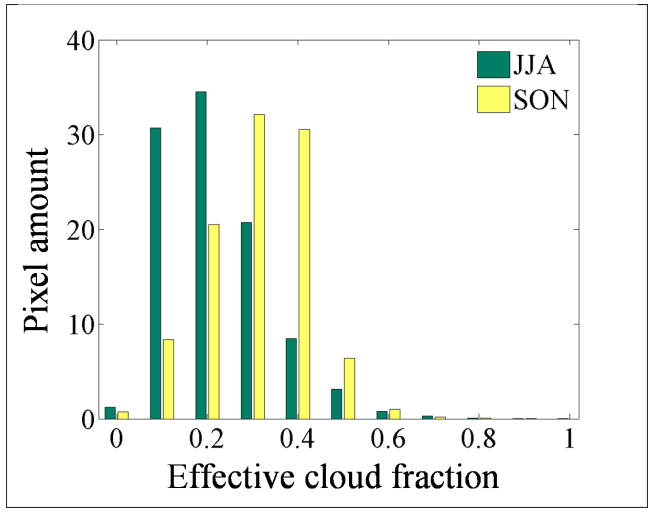

Figure 4.1: Averaged cloud fraction derived by the multi-wavelength algorithm for June to November 2006 over the Amazon basin. The period from June to August (JJA) is represented in green and September to November(SON) is in yellow

Figure 4.2 presents scatter plots of aerosol optical depths retrieved by the multi-wavelength algorithm, using the nominal biomass burning aerosol models and AERONET, for Alta Floresta and Cuiabá-Miranda. The data seem to be less scattered for Cuiabá-Miranda than for Alta Floresta. For Cuiabá-Miranda, Figure 4.2(b), OMI aerosol optical depths correlate well with the AERONET data but there is an offset of ca. 0.12, with a correlation coefficient close to 0.80. The comparison for Alta Floresta is less favorable. In particular for low aerosol optical depth $\tau \in [0.1\ 0.2]$ measured by AERONET sunphotometers, the OMI retrieved values varies betwen [0 2].

Figures 4.3 et 4.4 show a similar comparison between the AERONET and the multi-wavelength algorithm, but with either the forest or the savanna aerosol models used in the retrieval. The aerosol optical depth retrieved for Cuiabá-Miranda did not show substantial improvement. The modest correlation for Alta Floresta increased by 10 % by the introduction of the forest dedicated aerosol models, with a slope close to unity, but a systematic biais of 0.39 still remains.

The overestimation of the aerosol optical depth finds several explanations, the surface reflectance, cloud contamination and 3-D aerosol-cloud radiative interactions. The wrong approximation of the surface reflectance still remain a major source of uncertainty in retrieval of aerosol optical depths over land. Despite significant improvement in cloud screening procedures for satellite remote sensing, cloud contamination still is an issue. The enhancement of the aerosol optical depth in the vicinity of cloud is estimated by Wen et al. [2007] to range from 50% to 140% for broken cumulus.

The exercise described above shows that the use of dedicated aerosol models leads to some improvements, but is not satisfactory. However, this exercise

should be repeated when a more reliable surface albedo database will be available.

4.4.2 Spatial variation of aerosol optical depth

Figure 4.5(a) shows a composite map of the averaged aerosol optical depth derived at 442 nm over the Amazon basin using the nominal aerosol models (June to December 2006). The white areas indicate places where no values were derived. The original values at 13×24 km^2 (at nadir), were averaged on a 0.25°×0.25° grid. Some high aerosol optical depths are observed in or near cloud areas, likely due to residual cloud contamination, 3-D aerosol-cloud radiative interaction, or enhanced relative humidity in these areas causing swelling of the aerosol particles and thus high extinction. The area around the ground-based measurement site Cuiabá-Miranda (15.73°S 56.02°W), is more homogeneous than arround Alta Floresta (9.92°S 56.02°W). The averaged aerosol optical depth for the observed period is 0.33 ±0.22. Averaging the aerosol optical depth values over 50 km around the Alta Floresta site where significant spatial gradients are observed might partly explain the mediocre correlation observed earlier. However, spatial averaging is necessary to reduce pixel to pixel variability and provide a statistical significant result.

Figures 4.6(a) and 4.7(a) are similar to Figure 4.5(a), except for the use of the forest and savanna dedicated aerosol models to retrieved the aerosol optical depth. These composite maps show similar spatial patterns as Figure 4.5(a). The averaged aerosol optical depth derived for the sets of forest and savanna aerosol models are respectively, 0.31 ±0.19 and 0.34 ±0.24.

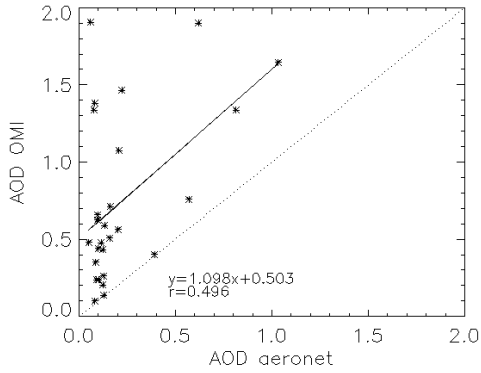

(a) Alta Floresta

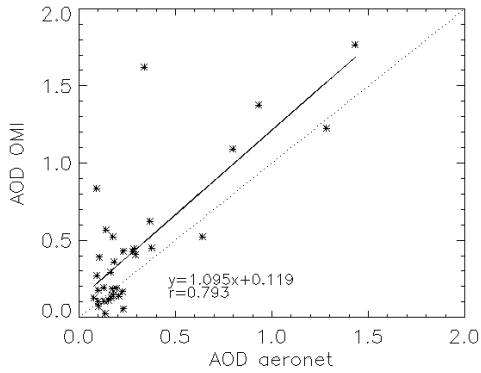

(b) Cuiabá-Miranda

Figure 4.2: Scatter plot of the aerosol optical depth for June to December 2006 for Alta Floresta and Cuiabá-Miranda. The aerosol optical depths retrieved at 442 nm was averaged over a 50 km radius around the ground site. All aerosol optical depth measured between 16.15 UTC and 17.30 UTC at 440 nm were averaged. The nominal set of Biomass Burning aerosol models was used by the multi-wavelength algorithm to derived the aerosol optical depth.

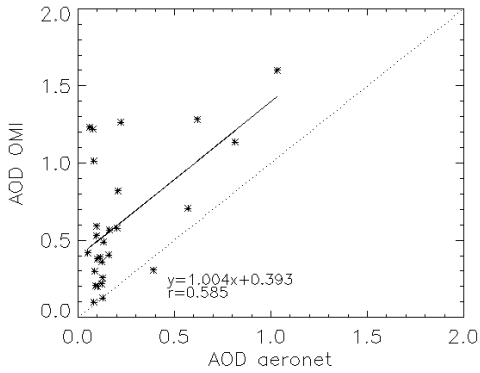

(a) Alta Floresta

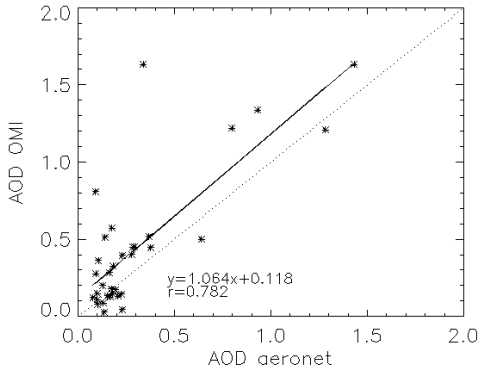

(b) Cuiabá-Miranda

Figure 4.3: Same as Figure 4.2 but the forest dedicated set of Biomass Burning aerosol models was used by the multi-wavelength algorithm to derived the aerosol optical depth.

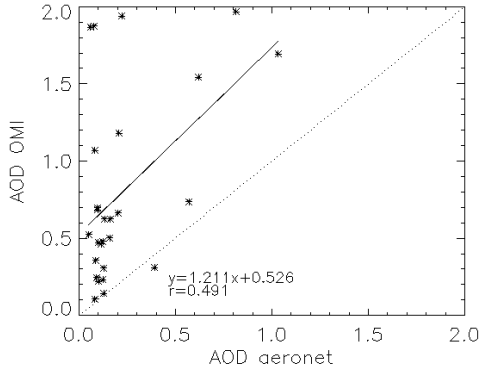

(a) Alta Floresta

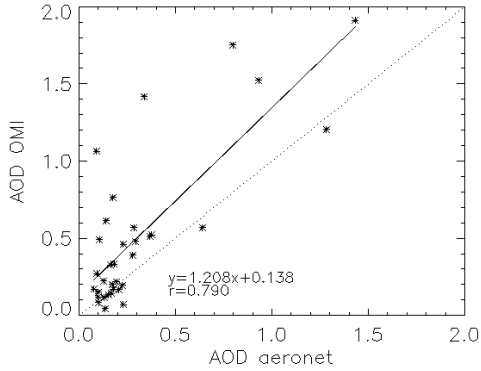

(b) Cuiabá-Miranda

Figure 4.4: Same as Figure 4.2 but the savannah dedicated set of Biomass Burning aerosol models was used by the multi-wavelength algorithm to derived the aerosol optical depth.

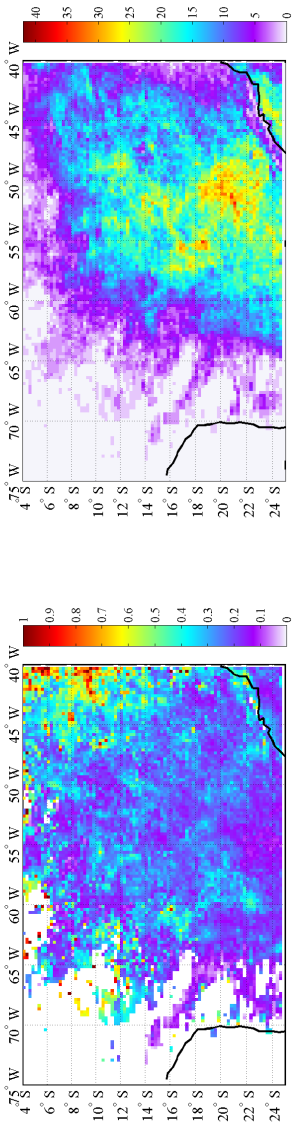

(a) (b)

Figure 4.5: The left panel is a composite map of the mean aerosol optical depth derived at 442 nm, by means of the multi-wavelength algorithm, for June to December 2006 using the nominal set of aerosol models. The right panel is a count of the number of values used to compute the mean aerosol optical depth.

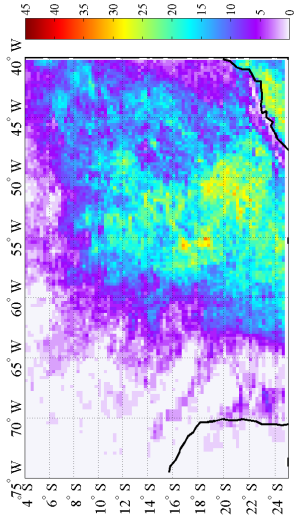

(b)

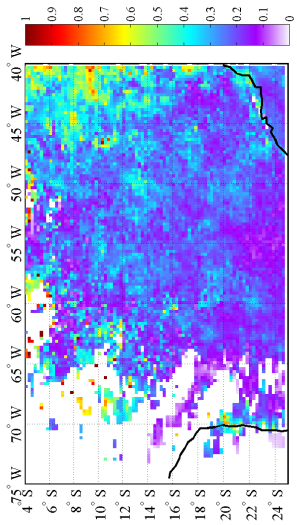

(a)

Figure 4.6: Same as Figure 4.5 but with the forest dedicated set of aerosol models.

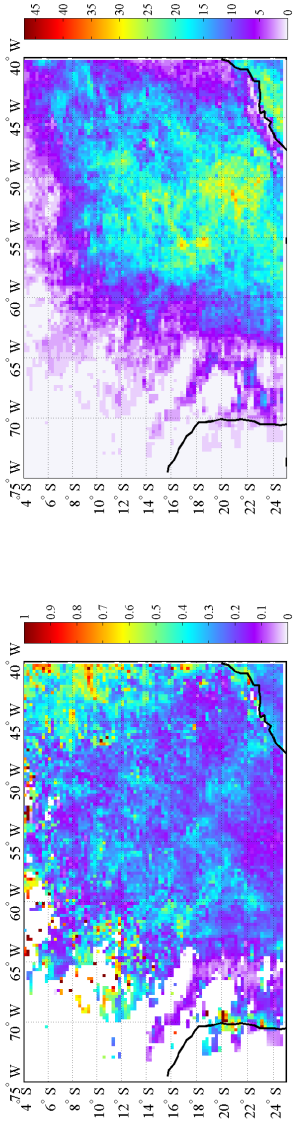

(a) (b)

Figure 4.7: Same as Figure 4.5 but with the savanna dedicated set of aerosol models.

4.4.3 Comparison with aerosol optical depth derived from MODIS

MODIS (Moderate Resolution Imaging Spectroradiometer) on Aqua and OMI onboard Aura are both part of the A-train constellation, they view the same area within 15 minutes, thus the derived aerosol optical depth distribution from both instruments should be similar. It is, therefore, worthwhile to compare the results derived from OMI at 477 nm and the MODIS aerosol optical depth at 470 nm. To this end, MODIS aerosol data (collection 5, Levy et al. [2007b]) have been meshed within the OMI grid for each matching orbit, the pixel-by-pixel difference was determined and meshed on a new latitude longitude grid ($0.25° \times 0.25°$) for the domain of interest.

Figure 4.8 presents the composite map of the difference between the aerosol optical depth derived from MODIS and OMI, ($\tau_{modis} - \tau_{omi}$), for the nominal aerosol models used with the multi-wavelength algorithm. The histograms of this difference are presented in Figure 4.8(b), for each set of aerosol models. The spatial variation of the difference for the forest and savanna dedicated aerosol models present a similar pattern as for the nominal aerosol models [Composite maps not shown]. The histograms, Figure 4.8(b), indicate that in about 90% of the cases OMI overestimates the aerosol optical depth with respect to MODIS. The histograms have a bimodal shape in all three cases and show that in about 55% of the cases the overestimation is between -0.5 and -0.15 and in about 40% of the pixels MODIS and OMI agree with an absolute value of less than 0.1.

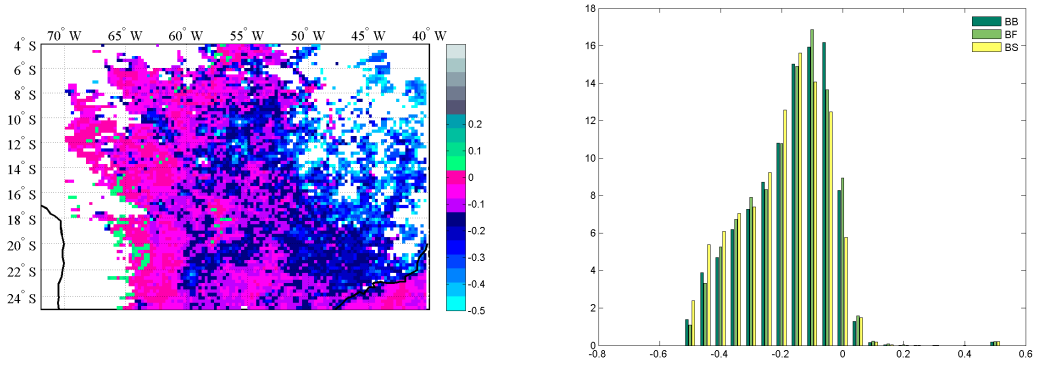

(a) nominal

Figure 4.8: Composite map of the difference between the mean aerosol optical depth derived from OMAERO at 477 nm and the mean aerosol optical depth derived from MODIS at 470 nm, for June to December 2006. Figure 4.8(b) is an histogram of the difference between the mean aerosol optical depth derived

4.5 Impact of the aerosol layer height

The vertical distribution of aerosols varies substantially and is determined by the injection height and a variety of atmospheric processes.

In this section an attempt is made to constrain the aerosol optical depth retrieved, by means of the multi-wavelength algorithm, using independent height information from spaceborne lidar measurements. The introduction of an additional constraint on the aerosol height layer should reduce correlated errors allowing for better estimates of the aerosol optical properties (τ, ω_0).

4.5.1 Introduction of the height constraint

In order to achieve this, the aerosol vertical distribution from the Cloud-Aerosol LIdar with Orthogonal Polarization [CALIOP, Winker et al. [2007]] is used. Detailed descriptions can be found on the CALIOP mission website (http://www-calipso.larc.nasa.gov/) and references therein. CALIOP is a two-wavelength polarization-sensitive lidar onboard the Cloud Aerosol Lidar and Infrared Pathfinder Satellite Observation (CALIPSO) satellite. CALIOP provides profiles of total backscatter at two wavelengths allowing for the derivation of the altitude of the aerosol layers. In this study, we used the aerosol layer product [Level 2, version 1, Vaughan et al. [2004]], which provides information on the aerosol layers such as the top and bottom height of the layers. The release of the CALIOP product used for this study presented some errors by identifying aerosols as cloud and vice-versa. However, this did not affect our study as we used the cloud detection protocol of the multi-wavelength algorithm.

Lidar altitude information is valuable but it is only available for a narrow track. During the study period the CALIPSO track closest to the measurement

sites was about 100 km. Therefore, the aerosol layer is assumed homogeneous over 150 km along and across the CALIPSO track. The altitude of the detected aerosol layer is introduced as *a priori* knowledge to the multi-wavelength algorithm, which constrains the inversion protocol to a specific part of the look-up table for each aerosol model. The CALIOP product provides the top and bottom height for up to ten layers. The geometric middle of the layer round to the closest integer was chosen as the aerosol layer height, when more than one layer was detected by CALIOP a weighted average geometric thickness was determined and the geometric middle of the layer was determined. The forest and savanna aerosol models were generated for layers at 0, 1, 2, 3, 4 and 5 km, only the models corresponding to geometric middle were allowed for the retrievals. The introduction of the aerosol height layer is analyzed for the nominal aerosol models as well as the forest and savannah dedicated ones. The aerosol optical depths derived are compared, like earlier, to ground-based and MODIS derived aerosol optical depths.

4.5.2 Comparison with ground based measurement

Figure 4.9 presents the comparison between the aerosol optical depth derived at 442 nm using of the multi-wavelength algorithm, constrained by CALIOP's height, and their measured counterparts at 440 nm. The multi-wavelength retrievals trace the temporal variation of the aerosol optical depth measured at both sites. The aerosol optical depth derived by means of the multi-wavelength algorithm are still overestimated with respect to the AERONET measurements at both sites, but the introduction of the height constraint reduced the offset by about 0.1.

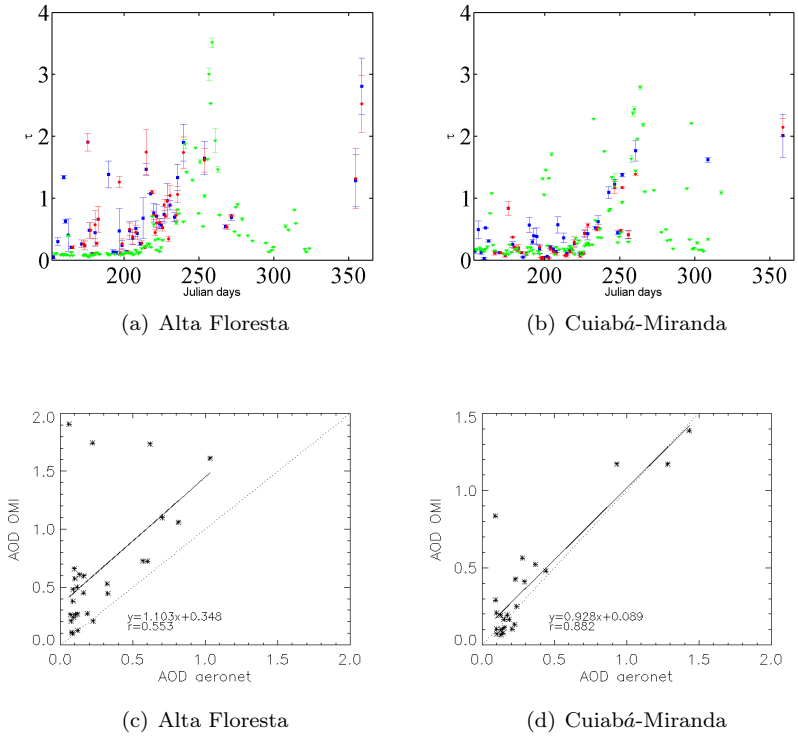

(a) Alta Floresta (b) Cuiabá-Miranda

(c) Alta Floresta (d) Cuiabá-Miranda

Figure 4.9: Timeseries (Upper panel) and scatterplot (lower panel) of the aerosol optical depth for June to December 2006 for Alta Floresta and Cuiabá-Miranda when applying the height constraint. The aerosol optical depths retrieved at 442 nm from the multi-wavelength algorithm was averaged over a 50 km radius around the ground site(in the upper panel the aerosol optical depth derived with the aerosol model constraint are marked in blue and the aerosol optical depth derived with both the aerosol model and the height constraint are marked in red). The aerosol optical depths measured between 16.15 UTC and 17.30 UTC at 440 nm were averaged(marked in green in upper panel). The default set of Biomass Burning aerosol models and a height constraint were used by the multi-wavelength algorithm.

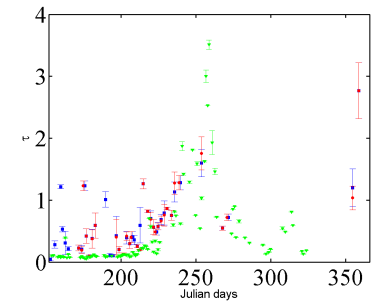

(a) Alta Floresta

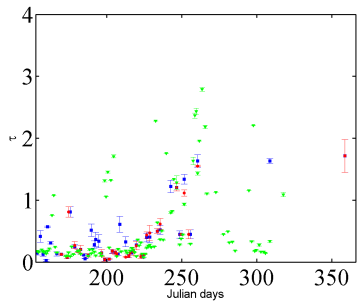

(b) Cuiabá-Miranda

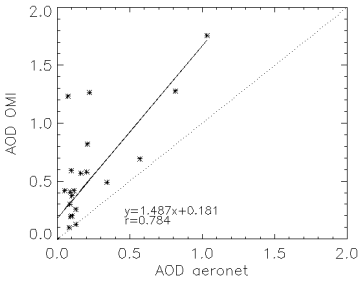

(c) Alta Floresta

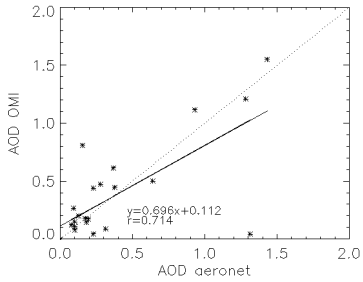

(d) Cuiabá-Miranda

Figure 4.10: Same as Figure 4.9 but the forest set dedicated Biomass Burning aerosol models as well as a height constraint from CALIOP were used by the multi-wavelength algorithm to derived the aerosol optical depth.

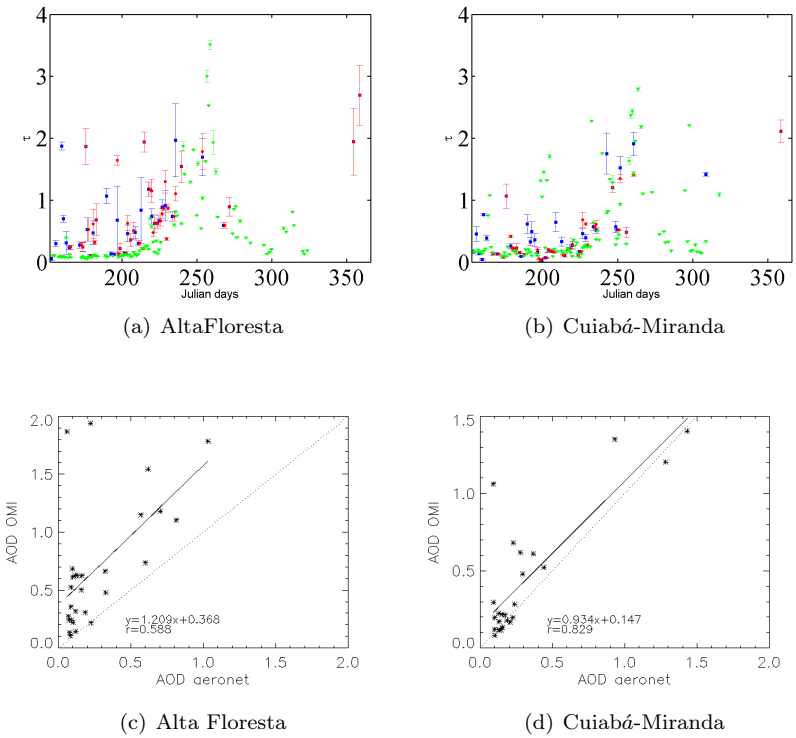

(a) AltaFloresta (b) Cuiabá-Miranda

(c) Alta Floresta (d) Cuiabá-Miranda

Figure 4.11: Same as Figure 4.9 but the savanna dedicated set of Biomass Burning aerosol models as well as a height constraint from CALIOP were used by the multi-wavelength algorithm to derived the aerosol optical depth.

Figures 4.10 and 4.11 show the same comparison as Figure 4.9 except that an additional constraint on the aerosol model, either forest or savannah, has been introduced in the multi-wavelength algorithm. At the Alta Floresta site, the introduction of a combined constraint, height and forest dedicated aerosol models, induces a large deviation of the slope from 1, with a simultaneous reduction of the offset by a factor of 2.7 and the correlation coefficient obtained, 0.78, is the highest. In contrast, at the Cuiabá-Miranda site, a severe drop in the slope is observed (from 1.09 to 0.7.), but a correlation of 70% remains between the datasets. On the other hand , the introduction of the combined constraint, height and savanna dedicated aerosol models, provides the best correlation retrieved for Cuiabá-Miranda with 83% of correlation between the datasets and a slope which is closer to 1, at the expense of a small increase of the offset. From the Alta Floresta point of view these constraints seems to deteriorate the correlation between the datasets with a slope deviating largely from one and an important offset, improving the correlation by less than 3%.

4.5.3 Spatial variation of the aerosol optical depth

Figure 4.12 is a composite map of the mean aerosol optical depth derived at 442 nm using the multi-wavelength algorithm and a height constraint. It has been shown earlier that the introduction of the height constraint has a favorable impact on the retrieved aerosol optical depth. However, the composite maps show that the introduction of the height constraint has no effect on the spatial distribution of the aerosol optical depth. The study of the various composite maps of the mean aerosol optical depth derived at 442 nm for combined constraints (not presented), leads to the same conclusion.

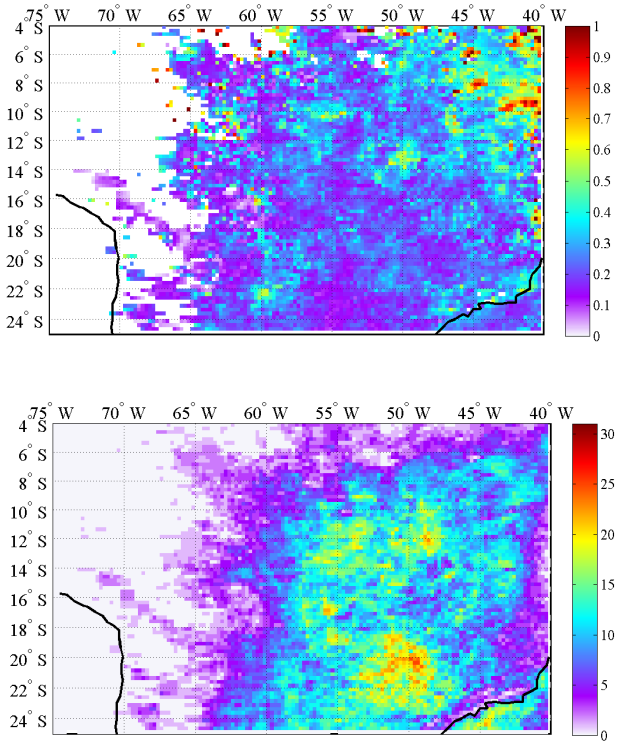

Figure 4.12: The upper panel is a composite map of the mean aerosol optical depth derived at 442 nm, by means of the multi-wavelength algorithm, for June to December 2006. The lower panel is a count of the number of values used to compute the mean aerosol optical depth. The nominal set of Biomass Burning aerosol models as well as a height constraint were used by the multi-wavelength algorithm to derived the aerosol optical depth.

Conclusion

The goal of the study was twofold. The sensitivity of the multi-wavelength algorithm for various models of aerosol generated by biomass burning and for

the aerosol height layer was tested.

The aerosol optical depths derived by the current implementation of the multi-wavelength algorithm which provide with the OMI Aerosol Product (OMI-AEROsol, OMAERO, Torres et al. [2002b]) present an overestimation with respect to AERONET. The overestimation of the aerosol optical depth finds several explanations such as the surface reflectance, cloud contamination and 3-D aerosol-cloud radiative interactions. This may be solved when a more reliable surface albedo database will be available and by accounting for the 3-D aerosol-cloud radiative interactions when retrieving aerosol optical over an area such as the Amazon basin where clouds are always present.

The multi-wavelength algorithm has been tested for different aerosol models representing savanna and forest fire originated particles. The aerosol optical depth retrieval results improved significantly in case of forest fire originated particles. The correlation with the aerosol optical depth provided by the AERONET networkincreased by 10%. However, in case of savanna fire originated particles no sigificant change was observed.

The introduction of the height constraint in the current implementation of the multi-wavelength algorithm reduces the observed offset by about 0.1. The results from the simultaneous introduction of a constraint on the aerosol models and on the aerosol layer altitude did not allow for any conclusion.

Acknowledgement

The work described in this paper is supported by SRON (The Netherlands Space Research Organization) and TNO internal funding. The OMI project is managed by NIVR and KNMI in the Netherlands. The authors thank Paulo

Artaxo and Brent Holben, P.I.'s for the AERONET sunphotometer data. The authors thank Joel Schafer for kindly provinding the aerosol size distribution for Alta Floresta and Cuiabá-Miranda.

Chapter 5

Concluding Remarks

Aerosol particles have short lifetimes and complex chemical composition and interact with clouds resulting in large spatial and temporal hetereogeneities. Therefore, satellite remote sensing is, nowadays, the most appropriate way to obtain measurement-based characterisation of aerosol optical properties on regional to global scale [IPCC, 2001, 2007]. In this thesis two algorithms were used to retrieve aerosol optical depth from satellite data. These algorithms apply only to cloud free scenes. The TNO DV-AATSR algorithm, is the first one and was presented in Chapter 2. This algorithm is an upgrade and coupling of two existing algorithms developed by Veefkind and de Leeuw [1998] and Veefkind et al. [1998] for ATSR-2. It allows for retrieving aerosol optical depth at three visible wavelengths over sea and two over land as well as the mixing ratio of the dominant aerosol models from ATSR-2 and AATSR measurements.

A new set of aerosol models that span the range of global aerosol conditions was built. In a pre-processing step two of the aerosol models which represent best the AATSR-observed scenes are selected to retrieve the aerosol optical properties.

The TNO DV-AATSR algorithm was applied to an area over Germany and

Northern Italy. In both cases the regional rather than global distribution of the aerosol population could be observed with the presence of an horizontal gradient where the high aerosol optical depth values are associated with strongly industrialized areas and low values appear at remote places. The aerosol optical depth retrieved by means of the TNO DV-AATSR algorithm has been compared with other measurement-based results. The favorable correlation observed provides confidence in the ability of the TNO DV-AATSR algorithm to retrieve aerosol optical depth.

The second algorithm, used in this thesis, is the multi-wavelength algorithm, introduced in Chapter 3. This algorithm provides aerosol optical depth at 14 wavelengths in the near ultraviolet and visible domains over both land and sea.

In a first study the multi-wavelength algorithm was first applied to North Western Europe for May to July 2005, see Chapter 3. The aerosol optical depth estimated by means of the multi-wavelength algorithm has been compared to other measurement-based data. The major discrepancies observed during this comparison were either due to cloud contamination or wrong estimation of the surface contribution over land. This last issue should be solved by the creation of a surface albedo database which is currently being developed based on OMI observations. Concerning the cloud screening procotol a compromise has to be reached mainly when working in the presence of broken cloud fields.

The goal of the second study using the multi-wavelength algorithm was twofold. This study took place over the amazon basin during the biomass burning season, first the sensitivity of the multi-wavelength algorithm for various models of aerosol generated by biomass burning was tested then the impact of aerosol layer height was estimated. It appears from this the study, that

the current implementation of the multi-wavelength algorithm presents an overestimation with respect to AERONET. This overestimation was explained by several phenomenon such as the surface reflectance, cloud contamination and 3-D aerosol-cloud radiative interactions. In case of forest fire generated particles, the aerosol optical depths were significantly improved, by the introduction of dedicated aerosols models, see Chapter 4. However, in case of savanna fire originated particles no significant change were observed. The introduction of the height constraint in the current implementation of the multi-wavelength algorithm reduces the observed offset by about 0.1. The results from the OMI multi-wavelength and the TNO DV-AATSR algorithms presented a favorable comparison with other measurement-based results which is encouraging. However, more application to various cases with different aerosol content, such as dust and/or biomass burning event, should be carried out to test behavior of the algorithms

In a second step, a synergistic use of these two algorithms should be considered. In fact, the monthly averaged aerosol optical depth derived by both the multi-wavelength and TNO DV-AATSR algorithms will provide the spectral variation of the aerosol optical depth from near-UV to Near-IR. This information will be useful as an a priori knowledge for both 3-D chemical transport model and to derive the aerosol global effect on the global radiative budget.

The following step in aerosol remote sensing is to use active remote sensing such as CALIOP and surface lidar network. Although this instrument focusses on narrow track they provide information on the vertical distribution of the aerosol fields. The combined passive and active remote sensing information will be a key parameter for a better understanding of climate and air quality issues.

Bibliography

J. R. Acarreta, J. F. De Haan, and P. Stamnes. Cloud pressure retrieval using the O_2-O_2 absorption band at 477 nm. *J. Geophys. Res.*, 109,D05204, 2004.

J.R. Acarreta and J.F. de Haan. Cloud pressure algorithm based on O_2-O_2 absorption. In P. Stammes and R. Noordhoek. OMI Algorithm Theoritical Basis Document Volume III: Clouds, Aerosols and Surface UV irradiance. *ATBD-OMI-03*, pages 17–30, 2002.

A. S. Ackerman, Strabala, Menzel, Frey, Moeller, Gumley, Baum, Schaaf, and Riggs. Discriminating Clear-Sky from cloud with MODIS- Algorithm Theoritical Basis Document. *ATBD-MOD-06*, 2002.

B. A. Albrecht. Aerosols, cloud microphysics and fractional. *Science*, 245:1227–1230, 1989.

B.E. Anderson, W.B. Grant, G.L. Gregory, E.V. Browell, J.E. Collins Jr, G.W. Scahse, D.R. Bagwell, C.H. Hudgins, and D.R. Blake N.J. Blake. Aerosols from biomass burning over the tropical South Atlantic region: Distribution and impacts. *J. Geophys. Res.*, 101 No. D19, 1996.

M. O. Andreae and P. J. Crutzen. Atmospheric aerosols: Biogeochemical sources and role in atmospheric chemistry. *Sciences*, 276:1052–1058, 1997.

H. Bauer, A. Kasper-Giebl, M. Löflund, H. Giebl, R. Hitzenberger, F. Zibuschka, and H. Puxbaum. The contribution of bacteria and fungal spores to the organic carbon content of cloud water, precipitation and aerosols. *Atmos. Res.*, 64:109 – 119, 2002.

N. O. Bellouin, O. Boucher, J. Haywood, and M. S. Reddy. Global estimate of aerosol direct radiative forcing from satellite measurement. *Nature*, 438, 2005.

F. K. Boersma, H. J. Eskes, J. P. Veefkind, E. J. Brinskma, R. J. van der A, M. Sneep, G. H. J. van Oord, P. F. Levelt, P. Stammes, J. F. Gleason, and E. J. Bruscela. Near-real time retrieval of tropospheric NO_2 from OMI. *Atmos. Chem. Phys. Dis.*, 6:12,301–12,345, 2006.

E. J. Brinksma, M. Roozendael van, T. Wagner, O. Ibrahim, A. Richter, F. Wittrock, H. Oetjen, G. Pinardi, C. Hermans, and C. Fayt. DANDELIONS Campaign held at the Cabauw Experimental Site for Atmospheric Research, The Netherlands. *Meeting Report*, published at Accent-Troposat2 website, 2005.

S. Chandrasekhar. Radiative transfer. *Oxford University Press*, London, 1960.

D. A. Chu, Y. J. Kaufman, C. Ichoku, L.A.Remer, D. Tanre, and B.N. Holben. Validation of MODIS aerosol optical depth retrieval over land. *Geophys. Res. Lett.*, 29, No. 12:1617, 2002.

A. D. Clarke, S. R. Owens, and J. Zhou. An ultra fine sea -salt flux from breaking waves: Implications for cloud condensation nuclei in the remote marine atmosphere. *J. Geophys. Res.*, 111, D06202, 2006.

C. Cox and W. Munk. Statistics of the sea surface derived from sun glitter. *J. Marine Res.*, 13:pp. 198–227, 1954.

R. l. Curier, G. de Leeuw, P. Kolmonen, A. ŰM. Sundström, L. Sochageva, and Y. Bennouna. Aerosol retrieval over land using the atsr dual-view algorithm.

In: A. A. Kokhanovsky and G. de Leeuw (Eds.), Satellite Aerosol Remote Sensing Over Land, 2008a.

R. L. Curier, J.P. Veefkind, R. Braak, B. Veihelmann, O. Torres, and G. de Leeuw. Retrieval of aerosol optical properties from omi radiances using a multi-wavelength algorithm: Application to western europe. *Accepted for publication in J. Geophys. Res.*, 2008b.

M. de Graaf, P. Stammes, O. Torres, and R. B. A. Koelemeijer. Absorbing aerosol index: Sensitivity analysis, application to GOME and comparison with TOMS. *J. Geophys. Res.*, 110, 2005.

J.F. de Haan, P. B. Bosma, and J.W. Hovenier. The adding method for multiple scattering calculations of polarized light. *Astron. Astrophys.*, 183:371–391, 1987.

G. de Leeuw, K. L. Davidson, S. G. Gathman, and R. V. Noonkester. Modelling of aerosols in the marine mixed layer. *SPIE conference on "Propagation Engeneering", Orlando, FL, USA*, 1989.

G. de Leeuw, A.N. de Jong, J. Kusmierczyk-Michulec, R. Schoemaker, M. Moerman, P. Fritz, J. Reid, and B. Holben. Aerosol retrieval using transmission and multispectral aatsr data. in: A summary of first year activities of the united arab emirates unified aerosol experiment: Uae2, reid, j.s., s.j. piketh, r. kahn, r.t. bruintjes and b.n. holben. *(Eds.). NRL Report Nr. NRL/MR/7534–05-8899*, pages pp 105–110., 2005.

F. Dentener, S. Kinne, T. Bond, O. Boucher, J. Cofala, S. Generoso, P. Ginoux, S. Gong, J. J. Hoelzemann, A. Ito, L. Marelli, J. E. Penner, J.-P. Putaud, C. Textor, M. Schulz, G. R. van der Werf, and J. Wilson. Emissions of primary

aerosol and precursor gases in the years 2000 and 1750, prescribed data-sets for AeroCom. *Atmospheric Chemistry Physics*, 6:4321–4344, 2006.

O. Dubovik, N. Holben, T. F. Eck, A. Smirnov, Y. J. Kaufman, M. D. King, D. Tanre, and I. Slutsker. Variability of absorption and optical properties of key aerosol types observed in worldwide locations. *Journal of Atmospheric Sciences*, 59:590–608, 2002.

P. A. Durkee, D. R. Jensen, Hindman E. E., and T. H. VonderHaar. The relationship between marine aerosols and satellite detected radiance. *Journal of Geophysical Research*, 91:4063 – 4072., 1986.

P. A. Durkee, F. Pfeil, E.Frost, and R. Shema. Global analysis of aerosol particle characteristics. *Atmos. Environ.*, 24A:2457–2471, 1991.

G Feingold. Modelling of the first indirect effect: Analysis of measurement requirements. *Geophys. Res. Lett.*, 30, 2003.

R. J. Flowerdew and J. D. Haigh. An approximation to improve accuracy in the derivation of surface reflectance from multi-look satellite radiometers. *Goephys. Res. Lett.*, 22:1693–1696, 1995.

P. Forster, V. Ramaswamy, P. Artaxo, T. Berntsen, R. Betts, D.W. Faheyand J. Haywood, J. Lean, D.C. Lowe, G. Myhre, J. Nganga, R. Prinn, G. Raga, M. Schulz, and R. Van Dorland. Changes in atmospheric constituents and in radiative forcing. in: Climate change 2007: The physical science basis. contribution of working group i to the fourth assessment report of the intergovernmental panel on climate change [solomon, s., d. qin, m. manning, z. chen, m. marquis, k.b. averyt, m.tignor and h.l. miller (eds.)]. *Cambridge University Press, Cambridge, United Kingdom and New-York, NY, USA*, 2007.

R. S. Fraser. satellite measurements of mass of saharan dust in the atmosphere. *Appl. Opt.*, 15:2471 – 2479, 1976.

W.M.F. Grey, P.R. North, S. O. Los, and R. M.Mitchell. Aerosol optical depth and land surface reflectance from multi-angle aatsr measurements: global validation and inter-sensor comparisons. *IEEE Trans. Geosciences Remote Sensing*, 44:2184 – 2197, 2006.

M. Griggs. Measurements of atmospheric aerosol optical thickness over water using erts-1 data. *Journal of the Air Pollution Control Association*, 25:622 – 626, 1975.

N Hatzianastassiou, C. Matsoukas, E. Drakakis, P.W. Stackhouse Jr., P. Koepke, A. Fotiadi, K. G. Pavlakis, and I. Vardavas. The direct effect of aerosols on solar radiation based on satellite observations, reanalysis datasets, and spectral aersol optcal properties from global aerosol data set (gads). *Atmos. Chem. Phys.*, 7:2585–2599, 2007.

J. Haywood and O. Boucher. Estimate of the direct and indirect radiative forcing due to tropospheric aerosol: a review. *Rev. Geophys.*, 38(4):513–543, 2000.

J. M. Haywood, R. S Osborne, P. N. Francis, A. Keil, P. Formenti, M. O. Andreae, and P. H. Kaye. The mean physical and optical properties of regional haze dominated by biomass burning aerosol measured from the c-130 aircraft during safari 2000. *J. Geophys. Res.*, 108 No.D13, 2003.

J. Heintzenberg. Fine particles in the global troposphere a review. *Tellus*, 41B, 1989.

B. M. Herman and E. Celarier. Earth surface climatology at 340 nm and 380 nm from TOMS data. *Journal of Geophysical Research*, 102:12,059 –12,076, 1997.

M. P. Hess, P. Koepke, and I. Schult. Optical prpoerties of aerosols and clouds: The software package opac. *Bull. Amer. Meteor. Soc.*, 79(No.5), 1998.

B. Holben, T. Eck, I. Slutsker, D. Tanre, J. Buis, A. Setzer, E. Vermote, J. Reagan, Y. Kaufman, T. Nakajima, F. Lavenu, I. Jankowiak, and A. Smirnov. Aeronet- a federated instrument network and data archive for aerosol characterization. *Remote Sens. Environ.*, 66:1–16, 1998.

N. C. Hsu, J. R. Herman, P. K. Bhartia, C. J. Seftor, O.Torres, A. M. Thompson, J. F. Gleason, T. F. Eck, and B. N. Holben. Detection of biomass burning smoke from TOMS measurements. *Geophys. Res. Lett.*, 23:745–748, 1996.

R. B. Husar, J. M. Prospero, and L. L. Stowe. Characterization of tropospheric aerosols over the oceans with the NOAA advanced very high resolution radiometer optical thickness operational product. *J. Geophys. Res.*, 102:16889–16909, 1997.

IPCC. Climate change 2001: The scientifc basis. contribtuion of working group i to the third assessement report of the intergovernemental panel on climate change. *Houghton, J.T., et al. (eds). Cambridge University Press*, United Kkingdom and New York:881 pp., 2001.

IPCC. Climate change 2007: The physical science basis. contribution of working group i to the fourth assessment report of the intergovernmental panel on climate change. *Solomon, S., D. Qin, M. Manning, Z. Chen, M. Marquis, K.B. Averyt, M. Tignor and H.L. Miller (eds.). Cambridge University Press, Cambridge, United Kingdom and New York, NY, USA*, page 996, 2007.

M. et al. Kanakidou. Organic aerosol and global climate modelling:a review. *Atmos. Chem. Phys.*, 5:1053 – 1123, 2005.

D. G. Kaskaoutis, Kambezidis, H. D. Hatzianastassiou, N. Kosmopoulos, P. G., and K. V. S. Badarinath. Aerosol climatology: on the discrimination of aerosol types over four aeronet sites. *Atmos. Chem. Phys. Discuss.*, 7:6357–6411, 2007.

Y. Kaufman, O. Boucher, D. Tanre, M. Chin, L. A. Remer, and T. Takemura. Aerosol anthropogenic component estimated from satellite data. *Geophysical Research Letters*, 32, 2005.

Y. J. Kaufman, Wald A. E., Remer L. A., Gao B. C., Li R. R., and Flynn L. The MODIS 2.1μ m channel correlation with the visible reflectances for use in remote sensing aerosol. *IEEE Trans. on Geosci. and Rem. Sensing*, 30: 223–230, 1997.

S. Kinne, M. Schulz, C. Textor, S. Guibert, Y. Balkanski, S.E. Bauer, T. Berntsen, T.F. Berglen, O. Boucher, M. Chin, W. Collins, F. Dentener, T. Diehl, R. Easter, J. Feichter, D. Fillmore, S. Ghan, P. Ginoux, S. Gong, A. Grini, J. Hendricks, M. Herzog, L. Horowitz, I. Isaksen, T. Iversen, A. Kirkevåg, S. Kloster, D. Koch, J.E. Kristjansson, M. Krol, A. Lauer, J.F. Lamarque, G. Lesins, X. Liu, U. Lohmann, V. Montanaro, G. Myhre, J. Penner, G. Pitari, S. Reddy, O. Seland, P. Stier, T. Takemura, and X. Tie. An AeroCom initial assessment optical properties in aerosol component modules of global models. *Atmos. Chem. Phys.*, 6:1815–1834, 2006.

R. B. Koelemeijer, P. Stammes, J. W. Hovenier, and J. D. de Haan. A fast method for retrieval of cloud parameters using oxygen a-band measurements

frome the global ozone monitoring instrument. *J. Geophys. Res.*, 106:3475–3490, 2001.

R. B. A. Koelemeijer, J. F. de Haan, and P. Stammes. A database of spectral surface reflectivity in the range 335-772 nm derived from 5.5 years GOME observations. *Journal of Geophysical Research*, 108, 2003.

A. A. Kokhanovsky and G. de Leeuw. *Satellite Aerosol Remote Sensing Over Land*. 2009.

A.A. Kokhanovsky, R. L. Curier, G. de Leeuw, W. M. F. Grey, K.H. Lee, Y. Bennouna, R. Schoemaker, and P. R. J. North. The inter-comparison of AATSR dual view aerosol optical thickness retrievals with results from various algorithms and instruments. *Int. J. Remote Sensing*, 2008.

P. F. Levelt, E. Hilsenrath, G. W. Leppelmeier, G. H. J. van Oord, P. K. Barthia, J. Tamminen, J. F. de Haan, and J. P. Veefkind. Science Objective of the Ozone Monitoring Instrument. *IEEE Trans. Goe. Rem. Sens.*, 44, No.5:1199 – 1208, 2006a.

P.F. Levelt, G.H.J. van Oord, M.R. Dobber, M. Malkki, H. Visser, J. de Vries, P. Stammes, J. Lundell, and H. Saari. The Ozone Monitoring Instrument. *IEEE Trans. Goe. Rem. Sens.*, 44, No. 5:1093 – 1101, 2006b.

R. C. Levy, L. A. Remer, and O. Dubovik. Global aerosol optical properties and application to moderate resolution imaging spectrometer aerosol retrieval over land. *J. Geophys. Res.*, 112, 2007a.

R. C. Levy, L. A. Remer, S. Mattoo, E.F. Vermote, and J. Kaufman. Second-generation operational algorithm: Retrieval of aerosols prpoerties over land

from inversion of moderate imaging spectroradiometer spectral reflectance. *Journal of Geophysical Research*, 112, D13211, 2007b.

X. Li-Jones, H. B. Maring, and J. M. Prospero. Effect of relative humidity on light scattering by mineral dust aerosol as measured in the marine boundary layer over the tropical atlantic ocean. *J. Geophys. Res.*, 103:31113–31122, 1998.

U. Lohmann and J. Feichter. Global indirect aerosol effects: a review. *Atmos. Chem. Phys.*, 5, 2005.

G. Mie. Beiträge zur Optik trüber Medien, speziell kolloidaler Metallösungen. *Ann. Phys. Leipsig*, 25:377–445, 1908.

M. I. Mishchenko, A. A. Lacis, B. E. Carlson, and L. D. Travis. Nonsphericity of dustlike tropospheric aerosols: implications for aerosol remote sensing and climate modeling,. *Geophys. Res. Lett.*, 22:1077 – 1080, 1995.

P. R. J. North, Briggs S. A., Plummer S. E., and Settle J. Retrieval of land surface bidirectional reflectance and aerosol opacity from ATSR-2 multianlge imagery. *IEEE Trans. Goe. Rem. Sens.*, 37, 1999.

T. Novakov, D. A. Hegg, and P. V. Hobbs. Airborne measurements of carbonaceous aerosols during tarfox. *J. Geophys. Res.*, 102, 1997.

C.D. O'Dowd and G. de Leeuw. Marine aerosol production: a review of the current knowledge. *Phil. Trans. R. Soc. A*, 2007.

J. M. Prospero, P. Ginoux, O. Torres, S. E. Nocholson, and T. E. Gill. Environnemental characterization of global sources of atmospheric soil dust identified

with the Nimbus-7/TOMS absorbing aerosol product. *Rev. Geophys.*, 40(1), 2002.

H. R. Pruppacher and J. D. Klett. *Microphysics of clouds and precipitation.* Kluwer Acad., 1997.

P. K. Quinn, D. J. Coffman, T. S. Bates, T. L. Miller, J. E. Johnson, E. J. Welton, C. Neususs, M. Miller, , and P. J. Sheridan. Aerosol optical properties during INDOEX 1999: Means, variability, and controlling factors. *Journal of Geophysical Research*, 107, 2002.

J.S. Reid, T.F. Eck, S.A. Christopher, P.V. Hobbs, and B. Holben:. Use of the ångstrom exponent to estimate the variability of optical and physical properties of aging smoke particles in brazil. *J. Geophys. Res.*, 104 No. D22: 27,473Ű27,489, 1999.

L. A. Remer, Y. J. Kaufman, D. Tanre, S. Mattoo, D. A. Chu, J. V. Martins, R.-R. Li, C. Ichoku, R. C. levy, R. G. Kleidman, T. F. Eck, and E. Vermoteand B. N. Holben. The MODIS Aerosol Algorithm, Products, and Validation. *Journal of Atmos. Sci.*, Special Issue, 62:947–973, 2005.

L.A. Remer, D. Tane, Y.J. Kaufman, C. Ichoku, S. Mattoo, R. Levy, D.A. Chu, B. Holben, O. Dubovik, A. Smirnov, J. V. Martins, R.R. Li, and Z. Ahmad. Validation of MODIS aerosol retrieval over ocean. *Geophys. Res. Lett.*, 29, No. 12:1618, 2002.

C. Robles Gonzalez. *Retrieval of Aerosol Properties using ATSR-2 Observations and their Interpretation.* PhD thesis, University of Utrecht, Utrecht, The Netherlands., 2003.

C. Robles-Gonzalez and G. G. de Leeuw. Aerosol properties over the SAFARI-2000 area retrieved from ATSR-2. *J. Geophys. Res.*, in press, 2007.

C. Robles-Gonzalez, G de Leeuw, R. Decae, J. Kusmierczyk-Michulec, and P. Stammes. Aerosol properties over the indian ocean experiment (indoex) campaign area retrieved from ATSR-2. *Journal of Geophysical Research*, 111: D15205, doi:10.1029/2005JD006184, 2006.

R. W. Saunders and K. T. Kriebel. An improved method for detecting clear sky and cloudy radiances from avhrr data. *Int. J. Remote Sensing*, 9:123–150, 1988.

J.S. Schafer, T. F. Eck, B. N. Holben, P. Artaxo, and A. Duarte. Characterization of the optical properties of atmospheric aerosols in Amazônia from long-term AERONET monitoring (1993-1995 and 1999-2006). *J. Geophys. Res.*, 113, D04204, 2008.

M.R. Schoeberl, A. R. Douglass, E. Hilsenrath adn P.K. Barthia, R.Beer, J.W. Waters, M.R. Gunson, L. Froidevaux andJ. C. Gille, J.J. Barnett, P.F. Levelt, and P. DeCola. Overview of the EOS Aura Mission. *IEEE Trans. on Geosci. and Rem. Sensing*, 44, 2006.

M. Schulz, C. Textor, S. Kinne, Y. Balkanski, S. Bauer, T. Berntsen, T. Berglen, O. Boucher, F. Dentener, S. Guibert, I. S. A. Isaksen, T. Iversen, D. Koch, A. Kirkevag, X. Liu, V. Montanaro, G. Myhre, J. E. Penner, G. Pitari, S. Reddy, O. Seland, P. Stier, and T. Takemura. Radiative forcing by aerosols as derived from the AeroCom present-day and pre-industrial simulations. *Atmospheric Chemistry and Physics*, 6:5225–5246, 2006.

J.H. Seinfeld and S.N. Pandis. *Atmospheric Chemistry and Physics*. ISBN 0-471-17815-2. Wiley-interscience publication, 1998.

A. Smirnov, B. N. Holben, T. F. Eck, O. Dubovik, and I. Slutsker. Cloud screening and quality control algorithm for the AERONET database. *Remote Sensing of the Environment*, 73, 3:337–349, 2000.

M. Sneep, J.F. De Haan, P. Stammes, P. Wang, C. Vanbauce, J. Joiner, A. Vasilkov, and P. Levelt. Three-way comparison between OMI and PARASOL cloud pressure products. *, J. Geophys. Res.*, in press, 2008.

I. Sokolik and O. B. Toon. Incorporation of mineralogical composition into models of the radiative properties of mineral aerosol from UV to IR wavelengths. *J. Geophys. Res.*, 104, D8, 1999.

P. Stammes. Spectral radiance modelling in the UV-visible range, in: Proceedings of the International Radiation Symposium 2000: Currents problem in Atmospheric Radiation. *Hampton*, eds. W.L. Smith and Y. M. Timofeyev, A. Deepak Publ., 2000.

I. M. Tegen, Werner, S. P. Harrison, and K. E. Kohfeld. Relative importance of cli and land use in determining preseent and future soil dust emission. *Geophys. Res. Lett.*, 31, 2004.

G.E. Thomas, C.A. Poulsen, R. L. Curier, G. de Leeuw, S. H. Marsh, E. Carboni, R. G. Grainger, and R. Siddans. Comparison of AATSR and SEVIRI aerosol retrievals over the northern adriatic. *Quart. J. Roy. Meteor. Soc.*, 2007.

O. Torres, P. K. Bhartia, J. R. Herman, Z. Ahmad, and J. Gleason. Derivation of aerosol properties from satellite measurements of backscattered ultraviolet

radiation: Theoretical basis. *Journal of Geophysical Research*, 103(D14), 1998.

O. Torres, P. K. Bhartia, J. R. Herman, A. Sinyuk, P. Ginoux, and B. Holben. A long-term record of aerosol optical depth from TOMS observations and comparison to AERONET measurements. *Journal of Atmos. Sci.*, 59(3):398–413, 2002a.

O. Torres, R. Decae, J.P. Veefkind, and G. de Leeuw. OMI Aerosol Retrieval Algorithm In: P. Stammes and R. Noordhoek OMI Algorithm Theoritical Basis Document Volume III: Clouds, Aerosols and Surface UV irradiance. *ATBD-OMI-03*, pages 46–71, 2002b.

S. A. Twomey. The influence of pollution on the shortwave albedo of clouds. *Journal of Atmos. Sci.*, 34:1149–1152, 1977.

B. H. J. van den Oord, P. Veefkind, P. Levelt, T. Jhonson, K. Stefanidis, A. Fleig, and R. Noordhoek. OMI small pixels data. TN-OMIE-KNMI-397, 2002.

M. Vaughan, S. Young, D. Winker, K. Powell, A. Omar, Z. Liu, Y. Hu, and C. Hostetler. Fully automated analysis of spacebased lidar data: An overview of the calipso retrieval algorithms and data products. *Proc. SPIE*, 5575:16 – 30, 2004.

J. P. Veefkind and G. de Leeuw. A new algorithm to determine the spectral aerosol optical depth from satellite radiometer measurements. *J. Aerosol Science*, 29:1237–1248, 1998.

J. P. Veefkind, G. de Leeuw, and P. A. Durkee. Retrieval of aerosol optical depth over land using two angle view satellite radiometry during tarfox. *Geophys. Res. Letters*, 23:3135–3138, 1998.

J. P. Veefkind, G. de Leeuw, P. Stammes, and B. A. Koelemeijer. Regional distributions of aerosols over lands derived from ATSR-2 and GOME. *Remote Sens. Environ.*, 74:377–386, 2000.

J.P. Veefkind. *Aerosol Satellite remote sensing.* PhD thesis, University of Utrecht, Utrecht, The Netherlands, 1999.

B. Veihelmann, P. F. Levelt, P. Stammes, and J. P. Veefkind. Simulation study of the aerosol information content in OMI spectral reflectance measurements. *Atmos. Chem. Phys. Discuss.*, 2007.

E. F. Vermote and A. Vermeulen. Atmospheric correction algorithm : Special reflectances (MOD09), ATBD version 4.0. *available at http://modis-land.gfsc.nasa.gov/mod09/*, 1999.

et al. Vermote, E. Second simulation of the satellite signal in the solar spectrum, 6s: an overview. *IEEE Transactions Geosciences Remote Sensing*, 35:675–686, 1997.

H. Volten, O. Muñoz, E. Rol, J. F. de Haan, W. Vassen, J. W. Hovenier, K. Muinonen, and T. Nousiainen. Scattering matrices of mineral particles at 441.6 nm and 632.8 nm. *J. Geophys. Res.*, 106:17375 – 17401, 2001.

W. von Hoyningen-Huene, M. Freitag, and J. B. Burrows. Retrieval of aerosol optical thickness over land surfaces from top-of-atmosphere radiance. *J. Geophys. Res.*, 108, 2003.

M. Wang and H. R. Gordon. Radiance reflected from ocean-atmosphere system: synthesis from individual components of the aerosol size distribution. *Applied Optics*, 33:7088–7095, 1994.

W. Wanner, A. H. Strahler, B. Hu, P. Lewis, J.-P. Muller, X. Li, C. L. B. Schaaf, and M. J. Barnsley. Global retrieval of bidirectional reflectance and albedo over land from EOS MODIS and MISR data: Theory and algorithm. *Journal of Geophysical Research*, 102:17143–17162, 1997.

G. Wen, A. Marshak, R. F. Cahalan, L. A. Remer, and R. G. Kleidman. 3-d aerosol-cloud radiative interaction observed in collocated modis and aster images of cumulus cloud fields. *J. Geophys. Res.*, 112, D13204, 2007.

D. M Winker, M. McGill, and W. H. Hunt. Initial performance assessment of caliop. *Geophys. Res. Lett.*, 34 L19803, 2007.

H. Yu, Y. J. Kaufman, M. Chin, G. Feingold, L. A. Remer, T. L. Anderson, Y. Balkanski, N. Bellouin, O. Boucher, S. Christopher, P. DeCola, R. Kahn, D. Koch, N. Loeb, M. S. Reddyand M. Schulz, T. Takemura, and M. Zhou. A review of measurement-based assessment of aerosol direct radiative effect and forcing. *Atmos. Chem. Phys.*, 6:613 – 666, 2006.

Notes


IF WE DON'T SPEND IT, WE MIGHT LOSE IT OR GET LESS MONEY NEXT TIME.


SO, IF THERE IS ANYTHING YOU NEED TO BUY, NO MATTER HOW TRIVIAL, NON-URGENT OR UNNECESSARY, NOW IS THE TIME TO GET IT.


CAN I GET A RAISE?
I SAID SPEND THE MONEY, NOT WASTE IT.

AEROSOL RETRIEVAL AND VALIDATION

Aerosols affect the radiation budget and cloud processes. Aerosol properties can be measured at ground level with good accuracy only at local scale. Satellites allow for monitoring the highly variable aerosol fields at a reasonable spatial and temporal resolution. Two instruments and their aerosol retrieval algorithms are used. These algorithms allow for the retrieval of aerosol optical depth over both ocean and land: one was applied to the AATSR data to retrieve aerosol optical depth in the visible domain while the other was designed to retrieve aerosol optical properties from OMI in the UV range. These algorithms have been developed and tested over North Western Europe and the Amazon Basin. The case studies presented a collocation between high aerosol optical depth values and heavily industrialized areas and downwind from the local sources large spatial gradients of the aerosol concentration. Results compare well with both ground based measurements and other spaceborne instruments.

RESTITUTION DES PROPRIETES DES AEROSOLS ET VALIDATION

Les aérosols influencent le bilan radiatif global et les processus nuageux. Leurs propriétés optiques et physico-chimiques sont mesurées au sol avec une grande précision à échelle locale. Les satellites permettent un suivi des aérosols à des résolutions spatio-temporelles raisonnables. Deux instruments et leurs algorithmes sont utilisés pour restituer les épaisseurs optiques des aérosols au-dessus des océans et des terres: un a été appliqué aux données AATSR afin de restituer l’épaisseur optique dans le visible alors que l’autre permet de restituer les propriétés optiques dans l’UV à partir de OMI. Ces algorithmes ont été développés et testés sur le Nord-Ouest de l’Europe et sur le bassin amazonien. Les cas étudiés se situaient dans des zones industrialisées avec des couches d’aérosols de forte épaisseur optique sous le vent de sources locales avec de forts gradients de concentration. Les résultats montrent une bonne restitution des concentrations en aérosols.